EFFECTS OF ORIENTATION ON ELECTRO-MECHANICAL COUPLING BEHAVIOR OF FERROELECTRICS AND THEIR COMPOSITES

by

PING ZHAO

A dissertation submitted to the Graduate Faculty in Engineering in partial fulfillment of the requirements for the degree of Doctor of Philosophy, The City University of New York

2009

This manuscript has been read and accepted for the
Graduate Faculty in Engineering in satisfaction of the
dissertation requirement for the degree of Doctor of Philosophy.

	Dr. Jackie Li
Date	Chair of Examining Committee
	Dr. Mumtaz K. Kassir
Date	Executive Officer

Dr. Benjamin Liaw

Dr. Ali M. Sadegh

Dr. Honghui Yu

Dr. Yook-Kong Yong
Supervision Committee

THE CITY UNIVERSITY OF NEW YORK

Abstract

EFFECTS OF ORIENTATION ON ELECTRO-MECHANICAL COUPLING BEHAVIOR OF FERROELECTRICS AND THEIR COMPOSITES

by

Ping Zhao

Adviser: Professor Jackie Li

The aim of this dissertation is to systematically study the nonlinear electro-mechanical coupling behavior of ferroelectrics and their composites under multi-axial loadings. Both experimental investigation and theoretical modeling are carried out.

For experiments, piezoelectric ceramics and 1-3 piezoelectric composites are tested under mechanical compressive loading and electric field, respectively. When a mechanical or electric loading is applied to piezoelectrics or piezoelectric composites at an angle θ to the original poling direction, its nonlinear electromechanical response is dependent on such an angle. As the loading direction changes from 0° to 90° to the initial poling direction, the experimental results exhibit strong angle dependence and nonlinear behavior under compression and electric field.

For theoretical modeling, a micromechanics approach developed by Li & Weng [1, 2] is adopted and extended to study the orientation effects on the electromechanical coupling behavior of ferroelectrics. A two-level theory developed by Lu and Weng [3], which originally targeted to shape memory alloy systems, is modified to study the nonlinear

coupling behavior of piezoelectric composites. The results from both experimental data and modeling are compared and discussed.

Acknowledgements

I would like express my appreciation to my advisor Dr. Jackie Li not only for this advice on research, but also for her overall support and guidance.

I would like to thank my committee members, Dr. Benjamin Liaw, Dr. Ali M. Sadegh, Dr. Honghui Yu and Dr. Yook-Kong Yong, for their interest in this research and for their valuable time in reviewing this dissertation.

I wish to express my heartful appreciation to my family, whose patience, understanding and encouragement helped me during the course of this research.

I am grateful for the financial support provided by the Graduate Center of City University of New York in the form of Science Fellowship, Teaching Assistant from the Department of Mechanical Engineering, Research Assistant from the Research Foundation and financial support from National Science Foundation.

Contents

Abstract…. ...……iv

Acknowledgements…….vii

1. Introduction ……...1

2. Literature Review……...3

2.1 Ferroelectric Ceramics …..……...3

2.2 Piezoelectric Composites……12

2.3 Applications of Ferroelectrics and their composites……..…….....15

3. Basic Concepts……...……..23

3.1 Piezoelectricity……23

3.2 Ferroelectricity & Domain Switch……..……26

3.2.1 Domain Switch…….....27

3.2.2 Hysteresis of Ferroelectrics……..29

3.3 Crystal Structure of PZT...…….….35

3.4 Classification of PZTs…….38

3.5 Piezoelectric Composites…….....38

3.5.1 Sum and Product Properties…….....39

3.5.2 Combination Properties…….....41

3.5.3 Connectivity…….…….....43

3.5.4 Stress Concentration…….…….....45

4. Experimental Investigation of Ferroelectrics under Multiaxial Mechanical

Loading…….47

4.1 Materials Preparation...……...47

4.2 Experiment Setup……50

4.3 Experimental Procedures…….……...51

4.4 Experimental Results…….....52

4.4.1 Stress vs Strain Curve under Applied Compressive Loading……...52

4.4.2 Stress vs Electrical Displacement Curve under Applied Compressive Loading...…….…….....54

5. Micromechanical Modeling of Ferroelectrics...……...56

5.1 Domain Switch..…….....57

5.2 Constitutive Equations……60

5.3 Gibb's Free Energy and Kinetic Equation of Domain Switching…….....62

5.4 Nonlinear Stress vs Strain and Stress vs Electric Displacement Relation under Compressive Loading….…….....67

5.5 Discussion and Conclusions……...72

6. Experimental Investigation of Piezoelectric Composite ……74

6.1 Materials Preparation...……...74

6.2 Experimental Setup....…..……...77

6.2.1 Compressive Loading……...77

6.2.2 Electric Field Loading...……...79

6.3 Experimental Procedures…….……...82

6.3.1 Procedures under Compression……82

6.3.2 Procedures under Electric Field……...82

6.4 Experimental Results…….....83

6.4.1 Under Compressive Loading……83

6.4.2 Under Electric Field Loading...……...…….85

6.5 Discussion and Conclusions……...94

7. Micromechanical Modeling of Piezoelectric Composites……95

7.1 Micromechanics Modeling on PZT inclusions…….....95

7.2 Constitutive Modeling on the Composite……...……96

7.3 Nonlinear Stress vs Strain and Stress vs Electric Displacement Relation under Compressive Loading…..……..99

7.4 Discussion and Conclusions…….101

8. Conclusions and Future Works ……...……...102

8.1 Conclusions……...102

8.2 Future Works…….103

References……..105

List of Tables

Table 3.1 Examples of product properties. [93]……...……40

Table 4.1 Physical and piezoelectric properties of PZT840 & PZT850. [89]……..48

Table 6.1 Physical and piezoelectric properties of PZT5A1. [103]…….75

List of Figures

Fig 2.1 Experimental arrangement: (a) cutting out of a block of poled material at angle θ, (b) applying electric field to the block and measuring surface charge. [4]…….7
Fig 2.2 Measured dielectric responses of specimens loaded with electric field at angl θ in the range 0-180° from the poling direction. [4]……...8
Fig 2.3 Measured response of the 180° specimen and fitted simulations using the three models. [4]……..…….....9
Fig 2.4 Comparison between calculated responses using three models and the experimental results: (a) self-consistent crystal plasticity model, (b) simplified viscoplastic crystal model, (c) phenomenological model. [4]……10
Fig 2.5 Schematic of a typical multilayer ceramic (MLC) capacitor. [67]……..16
Fig 2.6 A piezoelectric spark generator. [67]……...20
Fig 2.7 Cantilever bimorphs with (a) a series connection and (b) parallel connection of beams. [67]…..……...21
Fig 2.8 Schematic of a bimorph showing (a) two free halves of the bimorph, (b) the free halves in an electric field, (c) the two free halves shown in (a) are joined to form a bimorph. [67]…….…….22
Fig 3.1 Structure of the unit cell $BaTiO_3$ (a) Paraelectric state, (b) Ferroelectric state. [86]……..……..27
Fig 3.2 Polarizing (poling) process for a piezoelectric ceramic crystal……...28
Fig 3.3 Ferroelectric hysteresis loop (schematic). [12]……31
Fig 3.4 Strain (ε) and electric field (E) relation curve. [89]……..32
Fig 3.5 (a) Reference state with polarization vectors in all directions and zero net polarization and strain, (b)Saturated state with polarization P and axial remnant $2e$, (c) Saturated state with zero polarization and axial remnant strain $2e$, (d)Saturated state with zero polarization and $-e$ axial remnant strain. [4]……..…….34
Fig 3.6 (a) Spontaneous Polarization of a PZT crystal from its unpoled state, (b) Reorientation of the domain under a compressive stress or a perpendicular electric field. [2]……..37
Fig 3.7 Dielectric constant plotted as a function of composition for series and parallel mixing. [93]……..……..40
Fig 3.8 Speed of stress waves in composite materials made from steel filaments in epoxy. Waves traveling parallel to the filaments travel faster than transverse waves; the transverse waves are slower than waves in the pure epoxy matrix. [94]……..……...42
Fig 3.9 Ten connectivity patterns. [32]…….44
Fig 4.1 Experimental arrangement: cutting a parent poled PZT material into small pieces at angle θ=0°, 30°, 45°, 60°, 90° ...……..……...49
Fig 4.2 The parent-specimen of PZT 850…….……49
Fig 4.3 Five small samples with different angles to the poling direction…….49

Fig 4.4 Experimental setup of PZT specimen under compressive load……...50
Fig 4.5 Experimental stress-strain relationship of PZT840 applied under compressive loading at an angle θ in the range 0-90° from the poling direction……....53
Fig 4.6 Experimental stress-strain relationship of PZT850 applied under compressive loading at an angle θ in the range 0-90° from the poling direction……....53
Fig 4.7 Experimental stress-electrical displacement relationship of PZT840 under compressive loading at an angle θ in the range 0-90° from the poling direction……..54
Fig 4.8 Experimental stress-electrical displacement relationship of PZT850 under compressive loading at an angle θ in the range 0-90° from the poling direction……..55
Fig 5.1 Applying compressive loading at an angle θ to the poling direction……57
Fig 5.2 Comparison between Eq.(5-3) and the experimental data of PZT 840 for the maximum depolarization in terms of the angle θ of applied compressive load to the initial poling direction…….…….59
Fig 5.3 Comparison between Eq.(5-3) and the experimental data of PZT 850 for the maximum depolarization in terms of the angle θ of applied compressive load to the initial poling direction…….…….60
Fig 5.4 Comparison for stress-electrical displacement relation (PZT840) between (a) calculation of micromechanics model and (b) the experimental data……...…68
Fig 5.5 Comparison for stress-strain relation (PZT840) between (a) calculation of micromechanics model and (b) the experimental data……..…….69
Fig 5.6 Comparison for stress-electrical displacement relation (PZT850) between (a) calculations of micromechanics model and (b) the experimental data……..……70
Fig 5.7 Comparison for stress-strain relation (PZT850) between (a) calculations of micromechanics model and (b) the experimental data……..…….71
Fig 6.1 Experimental arrangement: cutting a parent poled PZT5A1 composite into small pieces at angle θ= 30°, 45°, 60°……..……...76
Fig 6.2 PZT5A1/epoxy composites samples. (a) Original fully poled PZT5A1 composite bar, (b) Testing specimens with different angles to the poling fiber direction at θ=0°, 30°, 45°, 60°……...…….76
Fig 6.3 Experimental setup of PZT5A1 piezoelectric composite specimen under compressive load……..……..……78
Fig 6.4 Experimental setup of PZT5A1 piezoelectric composite specimen under electric loading……..…….80
Fig 6.5 Model 30/20 high-voltage power amplifier…….80
Fig 6.6 VIBRAPLANE Model 9100/9200 Vibration Isolation Table……..81
Fig 6.7 Experimental stress-strain relationship of PZT5A1 composite applied under compressive load at angle θ in the range 0-60° from the poling direction…....84
Fig 6.8 Experimental stress-electrical displacement relation of PZT5A1 composite under compressive load at angle θ in the range 0-60° from the poling direction……..85
Fig 6.9 Electric displacement vs electric field hysteresis loop at θ= 0°…….86
Fig 6.10 Electric displacement vs electric field hysteresis loop at θ= 30°…….87

Fig 6.11 Electric displacement vs electric field hysteresis loop at θ= 45°…….87
Fig 6.12 Electric displacement vs electric field hysteresis loop at θ= 60°…….88
Fig 6.13 Comparison of the hysteresis loops of electric displacement and electric field at θ=0°, 30°, 45°, 60°……..…….89
Fig 6.14 Change of the remenant polarization in term of angle θ……...89
Fig 6.15 Electric field vs strain hysteresis loop at θ= 0°……90
Fig 6.16 Electric field vs strain hysteresis loop at θ= 30°……..91
Fig 6.17 Electric field vs strain hysteresis loop at θ= 45°……..91
Fig 6.18 Electric field vs strain hysteresis loop at θ= 60°……..92
Fig 6.19 Comparison of the relation of electric field and strain at θ= 0°, 30°, 45°, 60°……..93
Fig 6.20 Change of the remenant strain in term of angle θ…….….93
Fig 7.1 (a) The composite model and (b) the comparison material…….……96
Fig 7.2 Comparison for stress-electrical displacement relation between theory and the experimental data……..……...……100
Fig 7.3 Comparison for stress-strain relation between (a) theory and (b) the experimental data……..……...101

1. Introduction

In recent years, researchers have been studying the nonlinear electro-mechanical behavior of ferroelectric ceramics both experimentally & theoretically due to their applications as transducers, sensors, actuators, micro-electro-mechanical systems and other smart structures and devices.

In general, the studies on electromechanical coupling behavior of ferroelectrics focus on uniaxial loading condition. Since a fully poled ferroelectric material is transversely isotropic, the response is directional dependent. There also have been extensive studies on the coupling behavior of piezoelectric composites. However, there is very little experimental data available for more complicated loading situation such as multiaxial loading. To the author's knowledge, only Huber and Bleck [4] and Shieh *et al* [5] have conducted the limited experimental testing on multiaxial electric field and/or mechanical loading of a ferroelectric ceramic. Along their experiments, they also introduced three different models to verify their experimental data. To be able to fully understand the entire range of the electromechanical coupling behavior of ferroelectrics and their composites, we have carried out a comprehensive study by both experimental testing and theoretical modeling.

Therefore, this dissertation is composed in the following orders: The literature review related to this study is briefly given in chapter 2. Basic concepts related to ferroelectrics and their composites are presented in chapter 3. Then chapter 4 and 5 are experimental testing and micromechanics modeling of piezoelectric ceramics

under a compressive loading at an angle θ in the range 0-90° from the poling direction. Chapter 6 is the experimental testing of 1-3 piezoelectric composites under compressive loading and electric field at an angle θ in the range 0-60° from the poling direction. Finally, in chapter 7, a two-level micromechanical modeling of 1-3 piezoelectric composites under compressive loading at an angle θ in the range 0-60° from the poling direction is developed and the results are compared the experimental data. Finally, the conclusions and suggestions for future works are presented at the last chapter.

2. Literature Review

2.1 Ferroelectrics Ceramics

Ferroelectric/piezoelectric materials have become increasingly important in the microelectronics industry and Micro-Electro-Mechanical Systems (MEMS) [6], such as actuators for active control of helicopter rotor blades and underwater vehicle control surfaces, ultrasonic rotary inchworm motor with high power and torque densities and rapid prototyping and stereolithography techniques [7]. A lot of crystalline materials show piezoelectricity effects. These include barium titanate, lead titanate zirconate (PZT), Rochelle salt, and PLZT ceramics [8], among the others.

There are mainly two approaches to study the electromechanical coupling behavior of ferroelectrics which include the classic phenomenological approach such as Landau-Ginsburg-Devonshire theories and micromechanics approach by considering the microstructure of the system. Since our focus is on anisotropic behavior of ferroelectrics, the classic phenomenological approach will not be used and discussed. Interested readers may refer to Fatuzzo and Merz [9], Jaffe et al [10], Lines and Glass [11], Jona and Shirane [12], Ikeda [13], and Strukov and Levanyuk [14].

On the other hand, micromechanics studies on ferroelectrics have evolved in the past decades. Originally, the micromechanics theory was developed to study the mechanical behavior of heterogeneous materials such as composites and polycrystals. Based on Eshelby's inclusion theory [15], Dunn and Taya [16], Dunn [17], and Dunn

and Wienecke [18], among the others, extended the micromechanics theory to study the electromechanical moduli of piezoelectric and their composites.

For the nonlinear coupling behavior of ferroelectrics, Hwang *et al* [19] developed micromechanics model to simulate electromechanical coupling behavior in each grain of the PLZT (Lead lanthanum zirconate titane). Then work energy criterion was applied to catch the critical loading at which the domain switching occurs in the grain. The electric displacement and strain were calculated by averaging over all grains during the mechanical modeling. The results were compared with experiments of PLZT 8/65/35.

Later, the same group (Hwang *et al* [20]) proposed a modified model of polarization switching to simulate the response of strain and electric displacement under electromechanical loading in polycrystalline tetragonal ferroelectric ceramics. A few additional parameters of the material were added to the energy equation to get a better agreement with the experimental results.

McMeeking *et al* [21] applied the potential energy of an infinite homogeneous piezoelectrics to construct criteria for the first crystallite to switch in an unpolarized polycrystalline ferroelectric.

Michelitsch *et al* [22] modified the model developed by Hwang *et al* [19]. For simplicity intergranular interactions are neglected. The model leads to the conclusion that the hysteresis of the macroscopic strain vs electric field requires both microscopic ferroelectric polarization switching and piezoelectric coupling on the scale of the grains. Despite the simplicity of the model all characteristic phenomena of

ferroelectricity are represented.

A microscopic constitutive model was presented by Chen *et al* [23]. They added an internal variable in the theoretical constitutive equations and domain volume fractions to simulate the nonlinear behavior of polycrystalline ferroelectrics.

Fan *et al* [24] also developed a micromechanics constitutive model to describe the nonlinear behavior of polarization switching. The irreversible strain was simulated by a mechanical model, consisting of several parallel-arranged Maxwell chains with each chain taking a main role in a different, successive stage of the switching process. This spreads the overall polarization switching over a range of stress and electric field levels.

Seemann *et al* [25] presented a micromechanical modeling of ferroelectric materials by using probability functions in the energy equations for domain switching.

A new domain-switching criterion in terms of internal-energy density was proposed for combined mechanical and electrical loads by Sun *et al* [26]. Based on consideration of the atomic structure of ferroelectric materials, it is recognized that 180° and 90° domain switching result from different mechanisms and, thus, require different critical internal-energy densities for switching. This model was found to yield very good predictions for both 180° and 90° domain switching.

As we mentioned above, those micromechanical approaches have used an energy criterion to simulate the domain switching of ferroelectric materials. In those models, the homogenization or averaging process is adopted to describe the overall response of a ferroelectric polycrystal. However, in the study of nonlinear behavior of a

ferroelectric material, the irreversible thermodynamics and physics of domain switch are also important. Li and Weng [1, 2] developed a micromechanics model combined with the irreversible thermodynamics and physics involved in domain switch. This method is different from those mentioned above because the irreversible thermodynamics has been applied to develop the ferroelectric behavior instead of an energy criterion.

Those results of micromechanical models have been approved to have good agreements with existing experimental data [19, 23, 24, 27, 28, 29] only under uniaxial loading although their approaches are different.

However, there is very little experimental data for more complicated situation such as multiaxial loading. Huber and Bleck [4] conducted a few experiments on multi-axial electric switching of a ferroelectric material. As shown in Fig 2.1a, a poled plate of PZT-5H was cut using a diamond saw into cuboidal blocks, with the faces of the blocks cut at differing angles θ to the polarization direction. On each specimen, pairs of faces were electroded by sputtering gold and painting with silver electrode paint. The faces on which electrodes were made were chosen such that an electric field could be applied at angle θ=0-180° to the polarization direction. Each specimen was suspended in the oil bath and subjected to electric field E increasing from 0 to 1.5 MVm^{-1}, then decreasing back to zero. The loading loop took 30 seconds. The surface charge on each specimen was measured by the voltage across a 3 μF capacitor (Fig 2.1b). Therefore the electric field E and electric displacement D were obtained by using $E = V / d$ and $D = CV_c / A$ where d is the distance between electrodes, C

is the capacitance of the metering capacitor and A is the area of the electroded surface (Fig 2.1b).

According to the experimental results, Fig 2.2 shows the relation of the change in electric displacement and applied electric field for a selection of specimens at θ=0, 45, 90, 135 and 180°. In the case of the 0° specimen, there is only slight non-linearity in the dielectric response because of no domain switching. By contrast, in the 180° specimen the change of remnant polarization occurs, of magnitude 0.48 Cm^{-2}. In the other cases, the curves show nonlinear responses under the electric field.

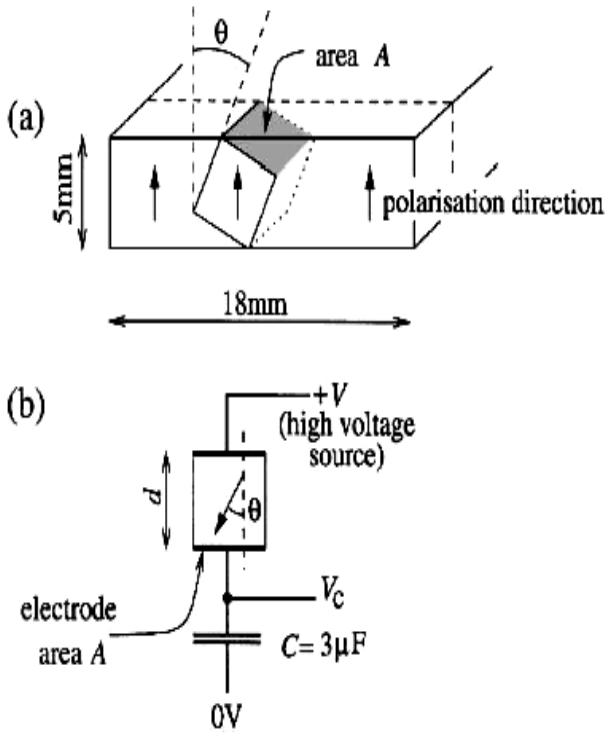

Fig 2.1 Experimental arrangement: (a) cutting out of a block of poled material at angle θ; (b) applying electric field to the block and measuring surface charge [4].

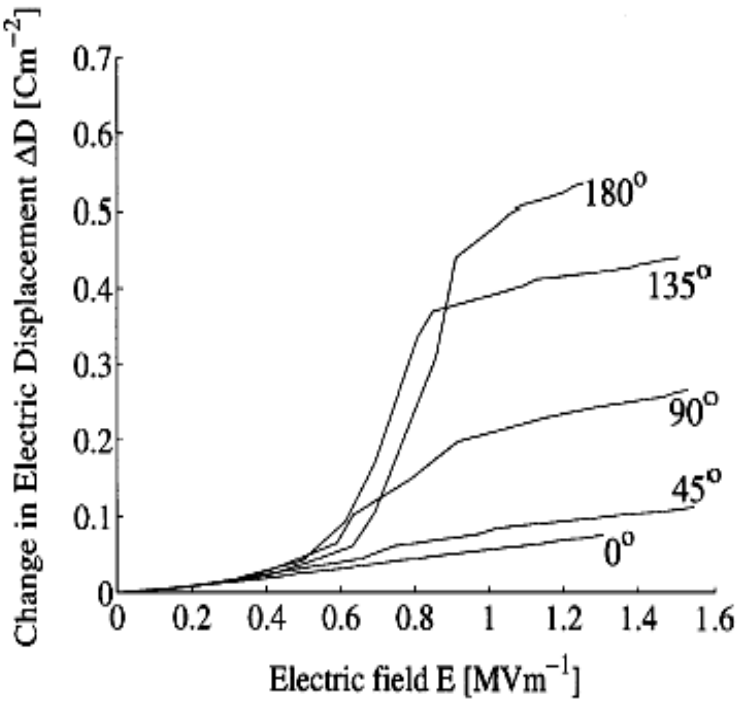

Fig 2.2 Measured dielectric responses of specimens loaded with electric field at angle θ in the range 0-180° from the poling direction [4].

Huber and Fleck [4] also introduced three constitutive models to capture the multi-axial response of the ferroelectric material: a rate-independent self-consistent plasticity model, a simplified viscoplastic crystal plasticity model with a reduced set of transformation systems, and a rate-independent phenomenological model. In each case the model was calibrated by using measurement of material response to fix the model parameters. The resulting simulations of the response of the 180° specimen are shown in Fig 2.3. It is clear that all the three models have sufficient flexibility to reproduce the response of the 180° specimen with good accuracy.

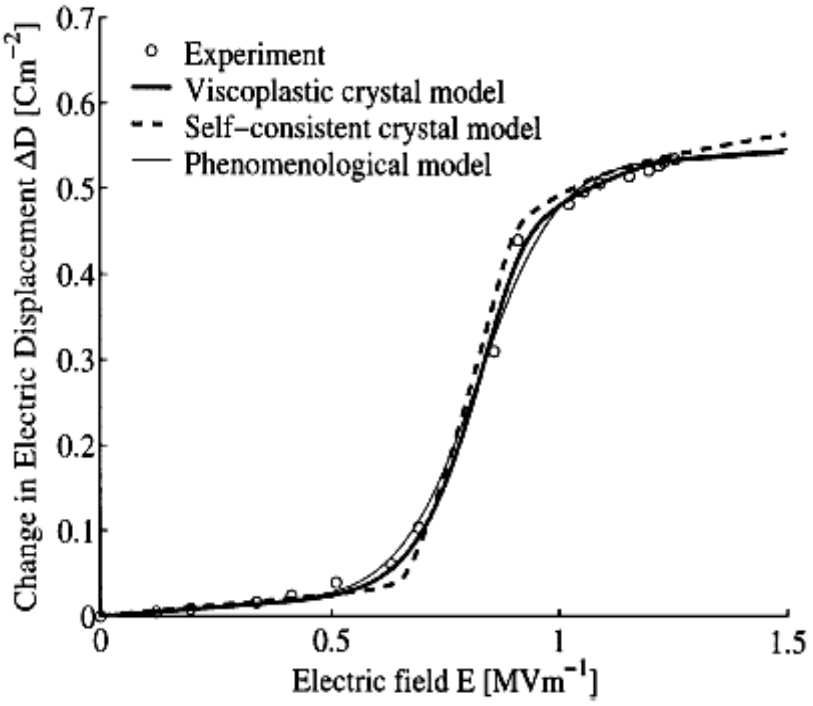

Fig 2.3 Measured response of the 180° specimen and fitted simulations using the three models [4].

Fig 2.4 shows the comparison of the three models with experiment results. As a conclusion, the self-consistent polycrystal model is computationally cumbersome for practical engineering modeling. The simplified viscoplastic crystal model neglects local interaction fields and then gives an improvement between speed and accuracy for practical engineering modeling. The phenomenological model is suitable for uniaxial loading and unable to reproduce the full range of multi-axial behavior in its present form.

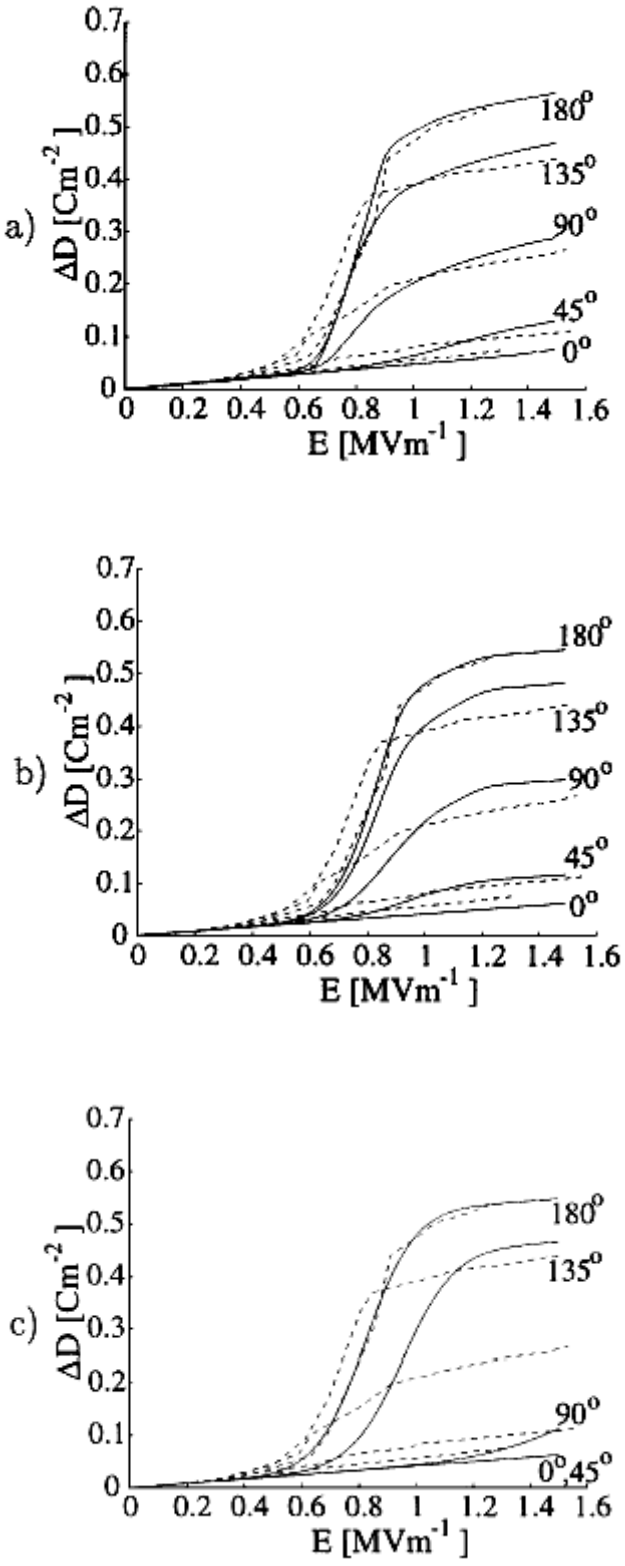

Fig 2.4 Comparison between calculated responses using three models and experimental results: (a) self-consistent crystal plasticity model, (b) simplified viscoplastic crystal model, (c) phenomenological model. [4]

Shieh *et al* [5] conducted experimental investigation to study the switching behavior of ferroelectrics under compression with proportional electric field loading. The multi-axial responses of barium titanate ($BaTiO_3$) and hard lead zirconate titanate (PZT-4D) are measured for stress and electric field loadings, and are compared to the response of soft lead zirconate titanate (PZT-5H) [4]. First, poled ferroelectric specimens are subjected to an electric field at an angle to the original poling direction. Second, unpoled ferroelectric specimens are loaded by a uniaxial compressive stress and a parallel, proportional electric field. The switching surfaces of $BaTiO_3$ and PZT-4D are constructed from the experimental measurements, and compared with existing data for PZT-5H. The measured responses are then used to evaluate the accuracy of existing micromechanical and phenomenological models of ferroelectric switching.

Li [30] extended the micromechanics models [1, 2] to study the multi-axial response of ferroelectrics. An equivalent system was introduced to capture the key nonlinear response of ferroelectric polycrystals subjected to the multixaial electrical loading. The overall effective polarization due to the multiaxial electrical switch is identical to the one of the real polycrystal system. Therefore, the problem became a uniaxial response which is simpler when the angle θ of applied electric field to poling direction is 0° or 180°. These theoretical results were in good agreement with the experimental data [4].

A computational micromechanical model was also developed by Chen *et al* [31], which is capable of simulating the response of ferroelectric materials under multiaxial

loading. This model was based on consideration of the constitutive behavior of single crystals to simulate the tetragonal and the rhombohedral crystal structures. Saturation of the linear piezoelectric effect and interaction between different grains in the polycrystalline ceramic were considered.

2.2 Piezoelectric Composites

For many applications, it is also necessary to use composite materials in which one or more of the constituents have piezoelectric properties. Lots of researches have been conducted to study the electromechanical properties of piezoelectric composite systems. Simple methods have been used to predict the behavior of a limited class of composite geometries [32-35]. Upper and lower bounds for the electromechanical moduli have been determined [36-39]. Also finite element methods were adopted to study the electromechanical properties [40, 41].

For effective linear electromechanical properties of piezoelectric composites, micromechanics approach has been considered to be one of the most powerful analytical tools. Several researchers have extended Eshelby's [15] classical solution of an infinite medium containing a single ellipsoidal inclusion to include piezoelectric constituents [42-44]. This approach ignores the interactions of the inclusions that occur at finite inclusion volume fractions, referred to as the dilute solution.

For finite volume concentration of inclusion, researchers [45-48] have also been able to extend the classical Mori-Tanaka [49, 50], Self-consistent [51, 52] and

Differential approaches [53, 54] to study the electromechanical coupling behavior of piezoelectric composites. More analytical solutions using micromechanics approaches with piezoelectric constituents have been obtained the literature [55-59].

Separately, an analytical model [60] and a numerical model [61] were developed by R. Kar-Gupta *et al* to describe the effects of fiber distribution in 1-3 piezoelectric composites with the active matrix under primarily static fields and elastic stress conditions.

For nonlinear coupling behavior of ferroelectric composites, Fang *et al* [62, 63] carried out experiments for 0-3 (particle-reinforced) and 1-3 (fiber-reinforced) types of ferroelectric composites with different viscoelastic and dielectric relaxation polymer-matrixes to study their nonlinear electro-mechanical behavior. As a result, the effects of viscoelasticity and dielectric relaxation of the matrices on the coupling response of the ferroelectric composites are significant. The nonlinear behavior of the ferroelectric composites also depends on the frequency of the applied loads.

Odegard [64] conducted a constitutive modeling to predict the bulk electromechanical properties of piezoelectric polymer composite by extending Mori-Tanaka Method and self- consistent approach.

Based on the multi-linear constitutive model of ferroelectric and ferroelastic piezoceramics, Zhang *et al* [65] performed a nonlinear finite element analysis with the representative volume element to model the poling behavior of 3-3 piezoelectric composites, in which appropriate periodic boundary conditions were prescribed for the displacements and the electric field of the composites.

Zeng *et al* [66] calculated the Eshelby tensor for the piezoelectric inclusion in a composite. The two-dimensional piezoelectric Eshelby tensor relates constrains and electric displacement in an elliptic inclusion to specified uniform eigenstrains and eigendisplacement. The Eshelby tensor was obtained by using the extended Lekhnitskii's formalism. The symmetric property of the Eshelby tensor was also established.

Mikata [58] determined a representation of the components of the piezoelectric Eshelby tensor in terms of certain integrals for a general ellipsoid in a transversely isotropic piezoelectric material. It was obtained that the explicit results for the piezoelectric Eshelby tensor for cylindrical inclusions aligned along the axes either parallel or perpendicular to the axis of the anisotropy in a transversely isotropic piezoelectric material. Mikata [59] also determined piezoelectric Eshelby tensors for a spheroidal inclusion.

It is evident that plenty of micromechanical approaches have been used to capture the electromechanical behavior of ferroelectric materials and their composites. Their calculations are able to compare to the existing experimental data under uniaxial loading. However, only few experimental testing under multiaxial loading have been conducted so the applicability of the models under multiaxial loading is not able to be verified. In order to study the electro-mechanical nonlinear coupling behavior of ferroelectric materials and their composites under multiaxial loading, both experimental investigation and theoretical modeling will be carried out in this dissertation.

2.3 Applications of Ferroelectrics and Their Composites

a) Capacitors

A capacitor consists of a dielectric material sandwiched between two electrodes. The total capacitance for this device is given by

$$C = \varepsilon_0 \varepsilon_r A / d \tag{3-12}$$

where C stands for the capacitance, ε_0 stands for the permittivity of free space, ε_r stands for the relative dielectric permittivity, d stands for the distance between the electrodes, and A stands for the area of the electrodes.

To get a high volumetric efficiency (capacitance per unit volume) the dielectric material between the electrodes should have a large dielectric constant, a large area and a small thickness. $BaTiO_3$ based ceramics having a perovskite type structure show dielectric constant values as high as 15,000 as compared to 5 or 10 for common ceramic and polymer materials. The high dielectric constant $BaTiO_3$ ceramic based disk capacitors are simple to make and have captured more than 50% of the ceramic capacitor market.

The volumetric efficiency can be further enhanced by using multilayer ceramic (MLC) capacitors. As shown in Fig 2.5, the MLC capacitor structure consists of alternate layers of dielectric and electrode material. Each individual dielectric layer

contributes capacitance to the MLC capacitor as the electrodes terminate in a parallel configuration. Hence the effective equation for capacitance becomes

$$C = n\varepsilon_0\varepsilon_r A/d \tag{3-13}$$

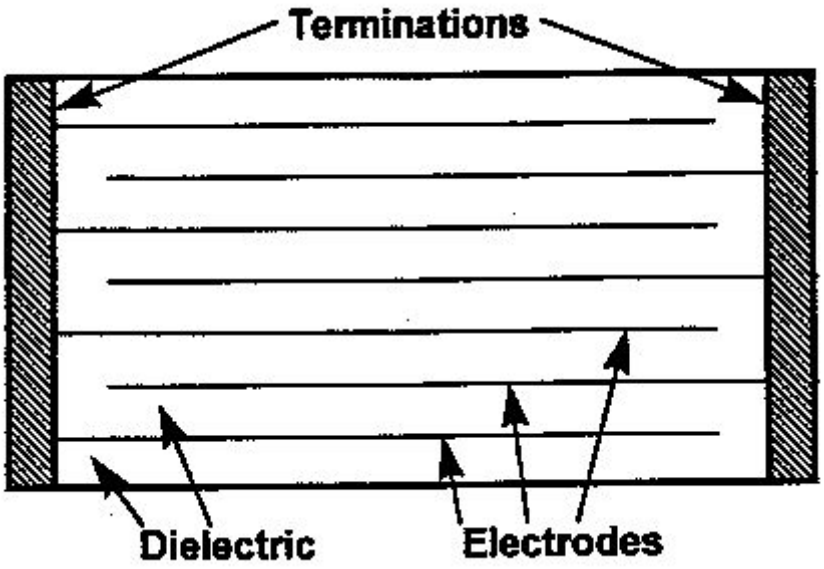

Fig 2.5 Schematic of a typical multilayer ceramic (MLC) capacitor [67]

where n = number of dielectric layers. The advances in tape casting technology have made it possible to make dielectric layers < 20 m thick. This, combined with the use of a high dielectric constant ceramic like $BaTiO_3$, allows large capacitance values to be achieved in relatively small volume capacitor devices [68-71].

b) Ferroelectrics Memories

Semiconductor memories such as dynamic random access memories (DRAM's) and static random access memories (SRAM's) currently dominate the market. However, the disadvantage of these memories is that they are volatile, i.e. the stored information is lost when the power fails. The non-volatile memories available at this time include complementary metal oxide semiconductors (CMOS) with battery backup and electrically erasable read only memories (EEPROM's). These non-volatile memories are very expensive. The main advantages offered by ferroelectric random access memories (FRAM's) include non-volatile and radiation hardened compatibility with CMOS and GaAs circuitry, high speed (30ns cycle time for read/erase/rewrite) and high density (4 μm^2 cell size).

Since ferroelectric materials spontaneously polarize on cooling below the Curie temperature, the magnitude and direction of polarization can be reversed by the application of an external electric field. The FRAM's made from ferroelectric thin films make use of this phenomena to store data. Data is stored by localized polarization switching in the microscopic regions of ferroelectric thin films. The FRAM's are non-volatile because the polarization remains in the same state after the voltage is removed as ferroelectrics have a non-linear hysteresis curve. The radiation hardness of FRAM's allow for the use of devices containing these memories in harsh environments such as outer space [72-75].

c) Ferroelectric Thin Film Waveguides

An optical waveguide controls the propagation of light in a transparent material (ferroelectric thin film) along a certain path. For the waveguide to work properly, the refractive index of the film should be higher that that of the substrate. For light to propagate in the waveguide, the thin film should be optically transparent. This can be achieved by fabricating the film under clean conditions and aiming for a fine grain size with ultra-phase purity and high density. A great deal of work has been done on making ferroelectric thin film waveguides from $LiNbO_3$ and $Li(Nb,Ta)O_3$ using LPE, EGM, and MBE methods. PZT and PLZT thin films are even better candidates for optical waveguide applications because of their large electro-optic coefficients [76-78].

d) Medical Ultrasound Applications

Piezoelectric materials can be used for both active and passive transducer applications. In the passive mode the transducer acts as a sound receiver i.e. there is conversion of sound energy into an electrical signal. The converse piezoelectric effect permits a transducer to act as an active sound transmitter. In the pulse echo mode, the transducer is used to perform both the active and passive functions at the same time. A sound wave is propagated into the medium and a faint echo is received back after a small time gap due to the acoustic impedance mismatch between the interface

materials. This principle is used in transducers for ultrasonic medical imaging applications. A lot of progress has been made in the last twenty years in the area of ultrasonic diagnostic equipment. This is mainly because of the developments in the area of piezoelectric materials used as the vibrator material and instrument electronics [79-81].

e) Gas Ignitors

A typical design for a voltage generator for gas ignitors is shown in Fig 2.6. It consists of two oppositely poled ceramic cylinders attached end to end in order to double the charge available for the spark.

The compressive force has to be applied quickly to avoid the leakage of charge across the surfaces of the piezoelectric ceramic. The generation of the spark takes place in two stages. The application of a compressive force F on the poled ceramic (under open circuit conditions) leads to a decrease in the length by dL^D. The potential energy developed across the ends must be higher than the breakdown voltage of the gap, for sparking to occur. When the spark gap breakdown occurs the second stage of energy generation starts. The electric discharge across the gap results in a change from open circuit conditions to closed circuit conditions with the voltage dropping to a lower level. The compliance of the material increases and allows further

compression of the ceramic by $dL^E - dL^D$ where dL^E is the displacement that would have occurred if the force 'F' had been applied under short circuit conditions. The combination of the strains from the open and short circuit conditions produce more energy that can be dissipated in the spark. Usually PZT ceramic disks are used for this application [82].

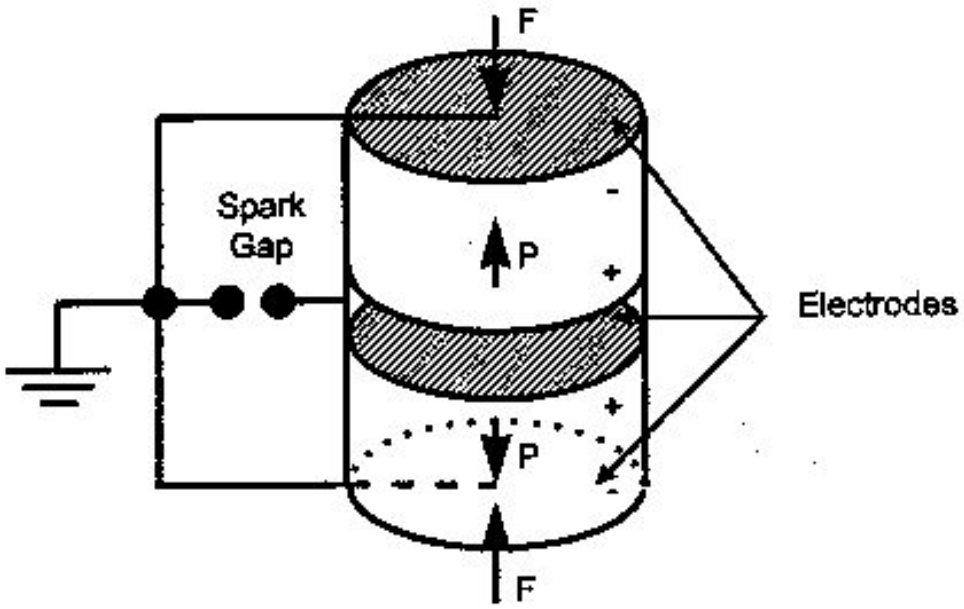

Fig 2.6 A piezoelectric spark generator [67]

f) Displacement Transducers

When force is applied to a long piezoelectric cantilever beam, one side is in tension while the other side will be in compression. No electrical output can be

obtained from this homogenous body by bending. Bimorphs made with two halves of separate beams with an electrode in between as well as on the top and bottom surfaces is shown in Fig 2.7. If the beams are poled in the opposite direction then on the application of a force 'F' the voltage generated on the outer electrodes will be additive (Fig 2.7 (a)). If the beams are poled in the same direction, the additive output can be obtained by connecting the outer electrodes and the center electrode as shown in Fig 2.7 (b).

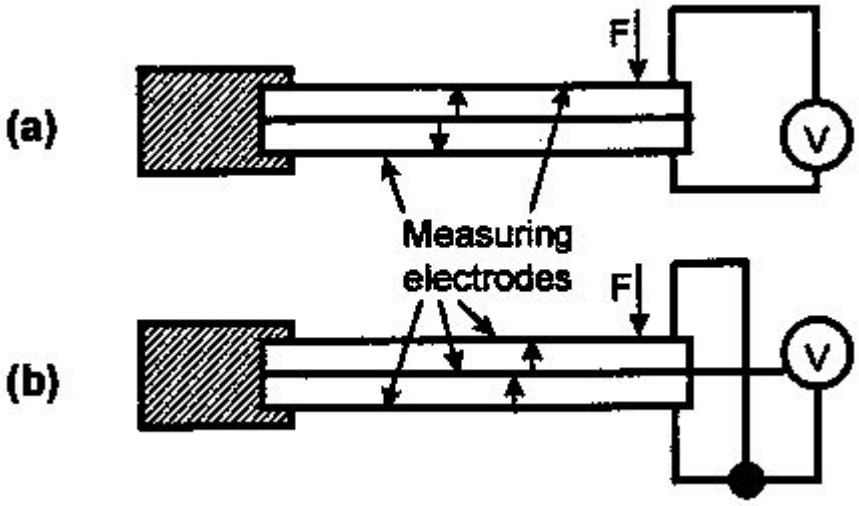

Fig 2.7 Cantilever bimorphs with (a) a series connection and (b) parallel connection of beams [67].

Conversely the application of a voltage to the bimorph causes it to bend. As shown in Fig 2.8. The application of an electric field causes one half of the cantilever beam to expand and the other half to contract. If they are joined in the form of a bimorph it leads to a net displacement on the application of an electric field [82].

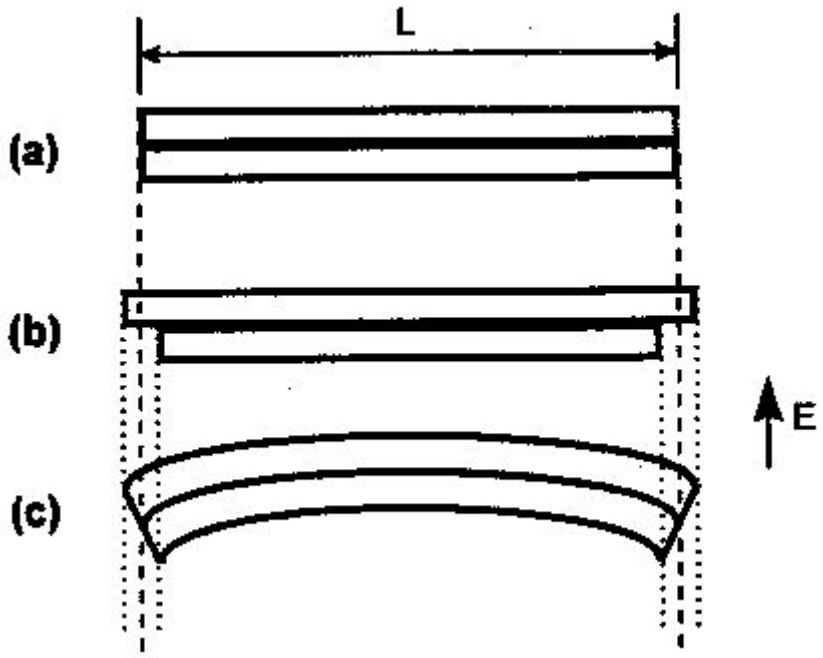

Fig 2.8 Schematic of a bimorph showing (a) two free halves of the bimorph; (b) the free halves in an electric field; (c) the two free halves shown in (a) are joined to form a bimorph [67].

3. Basic Concepts

3.1 Piezoelectricity

The piezoelectricity was discovered in 1880 by Pierre and Jacques Curie during the experiments on quartz and the word derived from the Greek *piezein* which means squeeze or press. Piezoelectricity is a fundamental process of electromechanical interaction and is a linear interaction between electrical and mechanical systems. In other words, when piezoelectric material is squeezed, an electric charge collects on its surface. Conversely, a piezoelectric material is subjected to an externally applied voltage, it deforms mechanically.

On the nanoscopic scale, piezoelectricity results from the nonuniform charge distribution with a crystal unit cell. When such a crystal is mechanically deformed, the positive and negative charge centers displace by different amount. So while the overall crystal appears electrically neutral, the difference between the charge center displacements causes an electric polarization within the crystal. Therefore, that electric polarization which produced by mechanical stress is called the direct piezoelectric effect. For example, if a uniaxial tensile stress σ is applied along one of the diad axes of a piezoelectric crystal, the magnitude of the electric moment per unit volume, or the polarization charge per unit area P, is given by

$$P = d\sigma, \tag{3-1}$$

where d is a constant, called a piezoelectric modulus. As implied by this equation, a

change from a tensile stress to an equal compressive stress reverses the direction of the polarization.

On the other hand, a crystal becomes strained when an electrical field is applied, which is called the converse piezoelectric effect [83]. Its existence is a thermodynamic consequence of the direct effect. It is found that there is a linear relation between the electric field E within the crystal and the strain components ε along the same direction of E. Moreover, the coefficients connecting the field and the strain in the converse effect are the same as those connecting the stress and the polarization in the direct effect. Therefore, the converse effect is written as

$$\varepsilon = dE . \tag{3-2}$$

Both of direct and converse piezoelectric effects are manifestations of the same fundamental property of crystal. Linear piezoelectric constitutive relations can be written in a general form as follows

$$\begin{aligned} \sigma_{ij} &= c_{ijkl}\varepsilon_{kl} - e_{nij}E_n , \\ D_m &= e_{mkl}\varepsilon_{kl} + k_{mn}^{(\varepsilon)}E_n , \end{aligned} \tag{3-3}$$

where $\sigma_{ij}, \varepsilon_{kl}$ are the stress and strain tensors respectively; D_m, E_n are the electric displacement and electric field vector respectively; c_{ijkl} and k_{mn} are the elastic moduli and dielectric constant tensors, respectively, and e_{ijk} is the piezoelectric constant tensor. The superscript (ε) stands for that the dielectric constants are measured at constant strain.

In the absence of a body force and a free charge density, the stress σ_{ij} and electrical displacement D_i satisfy the divergence condition, therefore Newton's and Maxwell's laws give

$$\sigma_{ij,j} = 0, \quad D_{i,i} = 0 \tag{3-4}$$

Under the small strain assumption, the strain and electric field can be derived from the displacement u_i and electrical potential Φ as

$$\varepsilon_{ij} = \frac{1}{2}[\frac{\partial u_i}{\partial x_j} + \frac{\partial u_j}{\partial x_i}], \quad E_i = -\frac{\partial \Phi}{\partial x_i} \tag{3-5}$$

Apparently, such a pairing has the advantage that stress σ_{ij} and electrical displacement D_i are both related to the divergence of the field, whereas strain ε_{ij} and electrical field E_i are related to the potential. As a result, each pair of quantities also shares the same kind of continuity conditions at the interface. This type of pairing is most useful to solve the boundary-value problems in piezoelectricity.

There are four possible ways to write the electromechanical constitutive equations depending on the boundary conditions. In order to concern the evolution of the new domains under an application of stress or electric field, the constitutive equations can be written as

$$\varepsilon_{ij} = s_{ijkl}\sigma_{kl} + d_{nij}E_n, \quad D_m = d_{mkl}\sigma_{kl} + k_{mn}^{(\sigma)}E_n, \tag{3-6}$$

where s_{ijkl} and d_{nij} are the elastic compliance and piezoelectric compliance tensors, respectively, and the superscript (σ) stands for that dielectric constants are measured at constant stress. d_{nij} is a third-order tensor and also called " the piezoelectric moduli tensor" which represents the direct piezoelectric effect of a crystal under the mechanical stress. This tensor also characterizes the converse effect for the strain ε_{ij} generated by an electric field E. The relationship between d and e is $d_{nij} = e_{nkl}s_{klij}$.

3.2 Ferroelectricity and Domain Switch

While piezoelectricity is used to describe a linear behavior of a crystal between electric & mechanical coupling, ferroelectricity describes the nonlinear coupling behavior of the crystal. The key physical phenomenon governing the nonlinear response of ferroelectrics happens below the Curie temperature. Above the Curie temperature the ferroelectrics has central symmetric structure which is said to be in paraelectric phase (Fig 3.1a), and below the Curie temperature the structure has changed to asymmetric structure which is said to be in ferroelectric phase (Fig3.1b). By lowering the temperature from the Curie temperature to below Curie temperature, the paraelectric to ferroelectric phase transition occurs. This phase transition is generally a very sharp transition [84]. It is accompanied by the development of spontaneous polarization in the unit cells, which is a characteristic of ferroelectric materials. For ferroelectric materials with the perovskite crystal structure, spontaneous polarization changes the crystal system from cubic to tetragonal [85]. The ferroelectric materials exhibit a linear piezoelectric behavior under small loading and nonlinear electrical-mechanical coupling behavior under large loading.

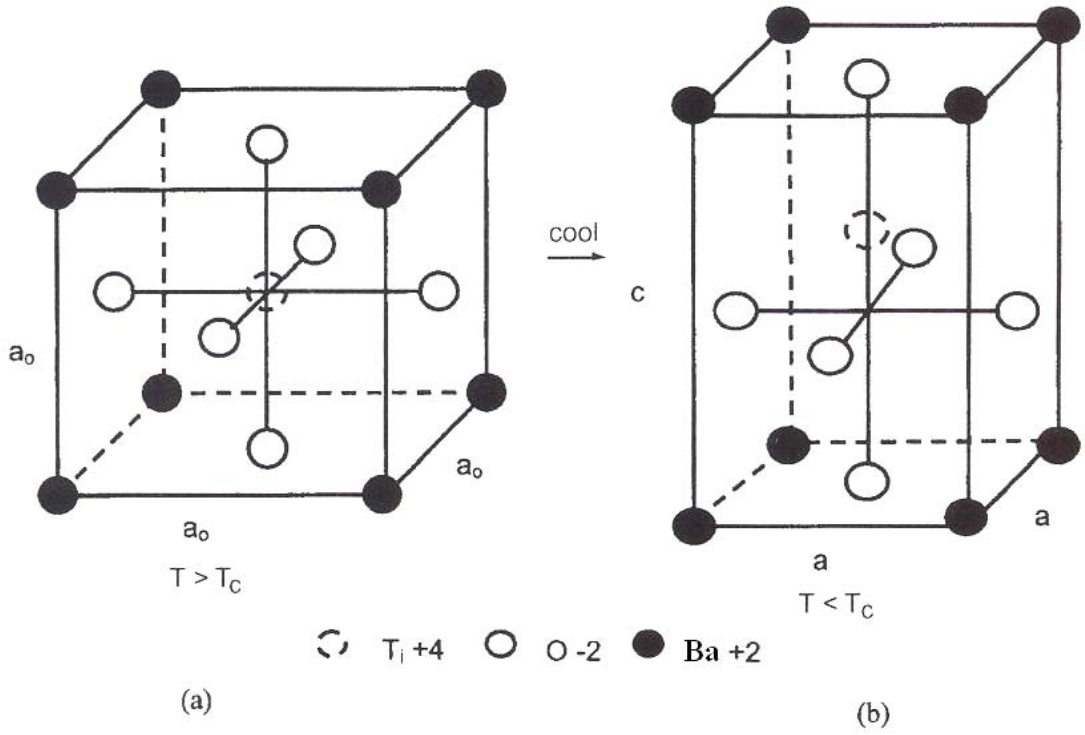

Fig 3.1 Structure of the unit cell $BaTiO_3$ (a) Paraelectric state (b) Ferroelectric state [86]

3.2.1 Domain Switch

During the phase transition from paraelectric state to ferroelectric state, unit cells in a crystal arrange in such a way that many unit cells in the neighborhood will have the same orientation for the spontaneous polarization and form a domain. The orientation of the spontaneous polarization of a single unit cell in a crystal can be either parallel or perpendicular to the crystallographic axis of the crystal. Therefore there are six possible orientations for a domain in a unit cell though an infinite number of domains are possible in a single crystal material. A polycrystal ferroelectric

material consists of many crystals with random crystallographic orientations, and hence the domains can have numerous random orientations. However, since both the single crystal and polycrystal piezoelectric materials have numerous domains with different orientations, the net polarization of an unpoled piezoelectric material is practically zero (Fig 3.2 a) [86].

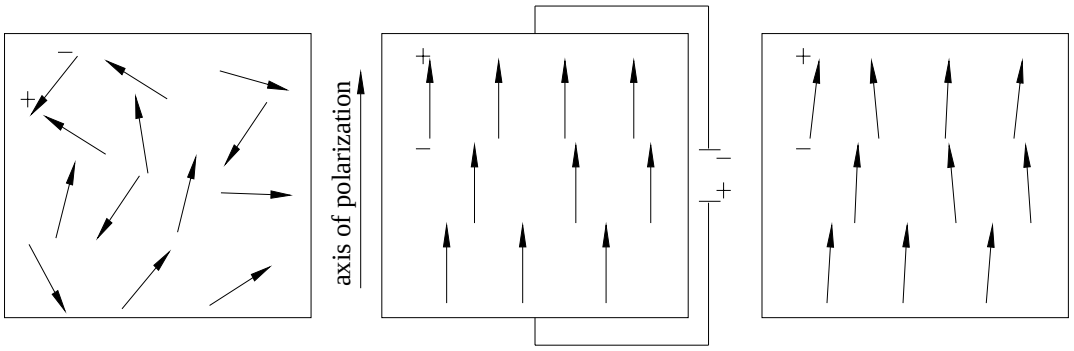

Fig 3.2 Polarizing (poling) process for a piezoelectric ceramic crystal

The domains in a ceramic crystal are aligned by exposing the crystal to a strong, direct current electric field, usually at a temperature slightly below the Curie point (Fig 3.2b). The unit cells in the ceramic reorient themselves to give a net polarization along the poling direction during the poling process. The unit cell changes its direction of spontaneous polarization by switching 90° or 180° to a direction closer to

the poling direction. In fact, domain switch is a gradual process and crystalline cells in a domain do not all switch simultaneously [87]. The process of domain switch starts with nucleation at different point on the existing domain, followed by switching of unit cells on the boundary of the nucleus, thus causing spreading of the newly formed domain. The movement of the newly formed domain boundary is called domain wall movement, and it sweeps fully through the existing domain to complete the domain switching process [86]. So through this poling process, domains most nearly aligned with the electric field expand at the expense of domains that are not aligned with the field, and the ceramic crystal lengthens in the direction of the field [87]. After the electric field is removed, the crystal has a permanent polarization, the remnant polarization, and is permanently elongated (Fig 3.2c).

3.2.2 Hysteresis of Ferroelectrics

Ferroelectric materials have electromechanical coupling effect in their constitutive relations and their ability to undergo domain switch in the poled state. Domain switch involves reorientation of the polarization and such a reorientation is also accompanied by the creation of polarization strain (or eigenstrain) [1]. Indeed reorientation of polarization (or domain switch) is the origin of nonlinearity in the polarization (P) (or electric displacement D) versus electric field (E) curve, whereas the accompanied eigenstrain is the source of nonlinearity in the stress (σ) and strain (ε) relation.

Upon electrical or mechanical loads, domain switch can be initiated depending on

the magnitude and the direction of the load. Electrical field can induce both 180° and 90° domain switch depending on the direction of the electrical field, while mechanical stress can induce only 90° domain switch [88]. Under electrical or mechanical loads, the poled materials will respond linearly in the initial stage (piezoelectricity), and begin to undergo domain switch at a critical load. In the plot of Polarization (P) vs Electric field (E), shown schematically in Fig 3.3, we obtain the portion OA of the curve. After commencement of domain switch, there are at least two domains in the materials and the material as a whole can be treated as a composite. As the electric field or mechanical stress continues to increase, the reorientation process will also continue and the polarization will increase rapidly (portion AB), until all the domains have totally switched into a single domain. After that, continuous loading will lead to a linear relation (portion BC) again as characterized by the dielectric constants and/ or the elastic moduli of the new domain: this is the state of saturation. While unloading, the polarization will follow the path CD, not go back to zero. Once the electric field is decreased to zero, some of the domain will remain, which the crystal will exhibit a remenant polarization P_r (OD). The value of spontaneous polarization P_s (OE) is the extrapolation of the linear curve BC back to the polarization axis. Continue to apply an electric field in the opposite direction, then the value of the field required to reduce P to zero (OF) is called the coercive field E_c. Further increase of the field in the negative direction will cause complete domain switch in this direction (FG). And also will attain a negative maximum polarization and negative maximum remanent polarization. The cycle can be completed by reversing the field direction once again

(GHC) [12].

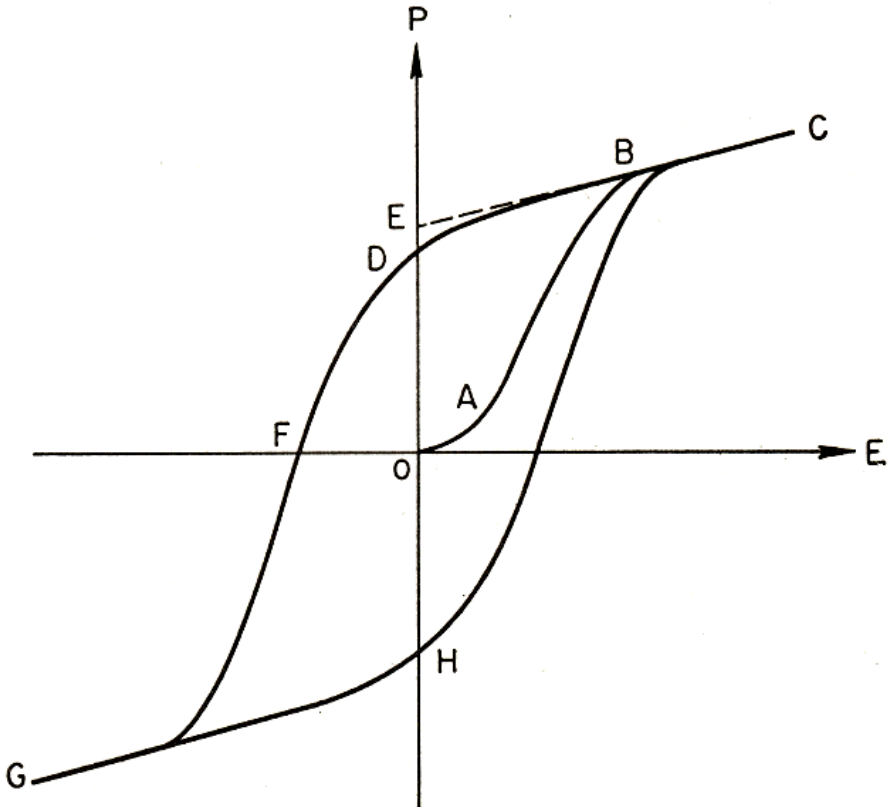

Fig 3.3 Ferroelectric hysteresis loop (schematic) [12]

Fig 3.4 shows the relative change of strain in the ferroelectric single crystal along the direction of polarization corresponding to the change in the electric field. The relative increase or/and decrease of strain parallel to the direction of the electric field is accompanied by a corresponding relative decrease or/and increase of strain

perpendicular to the electric field.

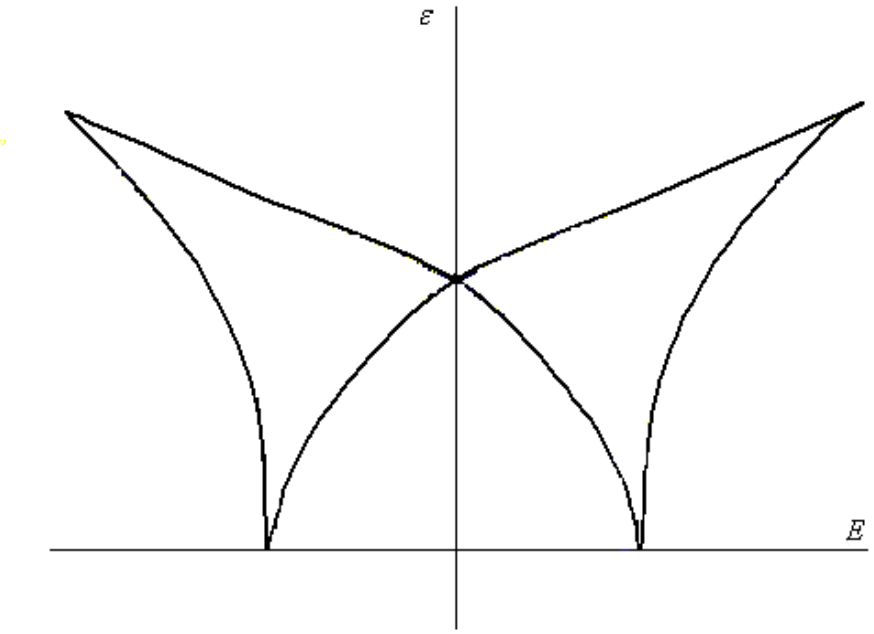

Fig 3.4 Strain (ε) and electric field (E) relation curve [89]

Switching is the source of remnant strain and polarization in ferroelectrics. When the applied loads or electric field can produce no further switch, the ferroelectric reaches a saturated state. Before poling, the orientations of the crystal variants in a random polycrystal are uniformly distributed over all spatial directions. This reference configuration has zero remnant strain and zero polarization (zero net polarization) (Fig3.5a). Subsequent switch may produce polarization and remnant strain, but note that the switch process conserves volume.

In order to explain potential states of overall saturation, consider three cases of loading subjected to a random polycrystal in the reference configuration. First, consider a monotonically increasing electric field; it causes alignment of polarization vectors along (or close to) the direction of the applied electric field. When saturation has been reached, an axissymmetric remnant strain and polarization are present. In the limiting case where all crystal variants become fully aligned with the applied field, the polarization gets a magnitude P and the axial strain reaches $2e$, at the same time the radial strain is $-e$ (Fig 3.5b). Second, consider uniaxial tension applied to the polycrystal in the reference configuration. Switch causes an axissymmetric state of remnant strain, but by symmetry the polarization remains zero. The saturated state of remnant strain is the same as that reached under electric filed; the limiting case of full alignment is shown is (Fig 3.5c).Third, consider uniaxial compression in the reference configuration. By symmetry, the average polarization remains zero. Switch causes each crystal variant to orientate its long axis close to the transverse plane. In the limiting case where all variants have their long axis in the transverse plane, the remnant strain is $-e$ axially and $e/2$ radially (Fig3.5d). Note that the saturation states shown in Fig 3.5 b-d share the common feature that the most negative principal strain has a value of $-e$.

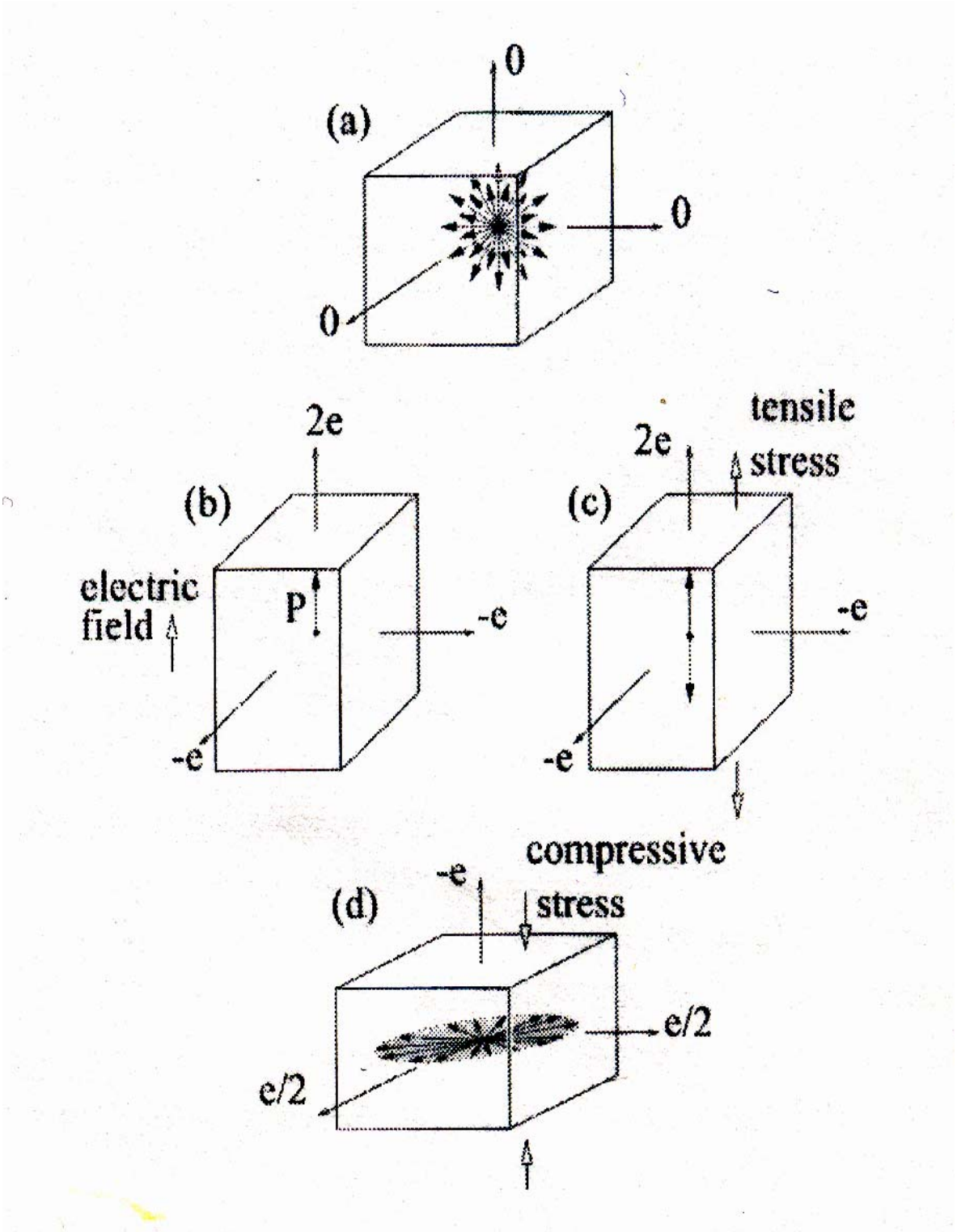

Fig 3.5 (a) Reference state with polarization vectors in all directions and zero net polarization and strain. (b) Saturated state with polarization P and axial remnant $2e$. (c) Saturated state with zero polarization and axial remnant strain $2e$. (d) Saturated state with zero polarization and $-e$ axial remnant strain [4]

3.3 Crystal Structure of PZT

Lead zirconate titanate PZT ($Pb(ZrTi)O_3$), with large piezoelectric coefficient, large dielectric coefficient and quick time response, was found to be an excellent piezoelectric ceramic based on ferroelectric crystals in 1954 [90]. Due to their intrinsic electromechanical coupling properties, PZT has become one of the most widely used ferroelectric ceramics. PZT is a perovskite alloy of lead zirconate (PZ) and lead Titanate (PT). PT is a ferroelectric material with a simple tetragonal structure, while PZ has a complex antiferroelectric ground state. Neither PT nor PZ are good piezoelectric materials separately, mixing them in a disordered solid solution gives rise to excellent piezoelectric response [91]. There are six macroscopic phases of PZT according to the zirconium/titanium ratio and temperature: A low temperature antiferroelectric phase, two rhombohedral phases in different temperatures (FE), a tetragonal phase (FE), a paraelectric high–temperature cubic phase and the low–temperature monoclinic phase (FE).

In tetragonal phase, PZT has a typical perovskite structure (ABO_3), consisting of a small tetravalent metal ion (titanium or zirconium) in the center, in the lattice of larger divalent lead ion and oxygen ions. However, there is extensive disorder in the magnitude and direction of tetravalent metal cations within their oxygen octahedral. There is also disorder in the magnitude of direction of the movements of both the lead and oxygen ions away from their original perovskite position. This disorder within the orderly perovskite lattice gives PZT very interesting properties.

The PZT crystal structures in unpoled state are cubic. Under an electric field or cooling, spontaneous polarization will cause the cubic structure to change to a tetragonal structure. In this process, one of the cube edges is elongated to become the tetragonal c axis, the two other cube edges are compressed to become the tetragonal a axes (Fig 3.6a). The positively charged titanate or zirconite ion moves from its original central position to a position aligned along the poling axis, and together with the negatively charged oxygen ions, forms a dipole moment. The total dipole moments in the materials with a unit volume is the spontaneous polarization P for PZT. Such a poled crystal can undergo a 180° domain switch under a reversed electric field or a 90° domain switch under a compressive load or under an electric field perpendicular to its original poled direction (Fig 3.6b). There are four possible directions of domain switch or four new domains in the unit cell. But in general, the evolution of the new domain under an increasing stress or electric field must be incorporated in order to determine the nonlinear constitutive relation of the system.

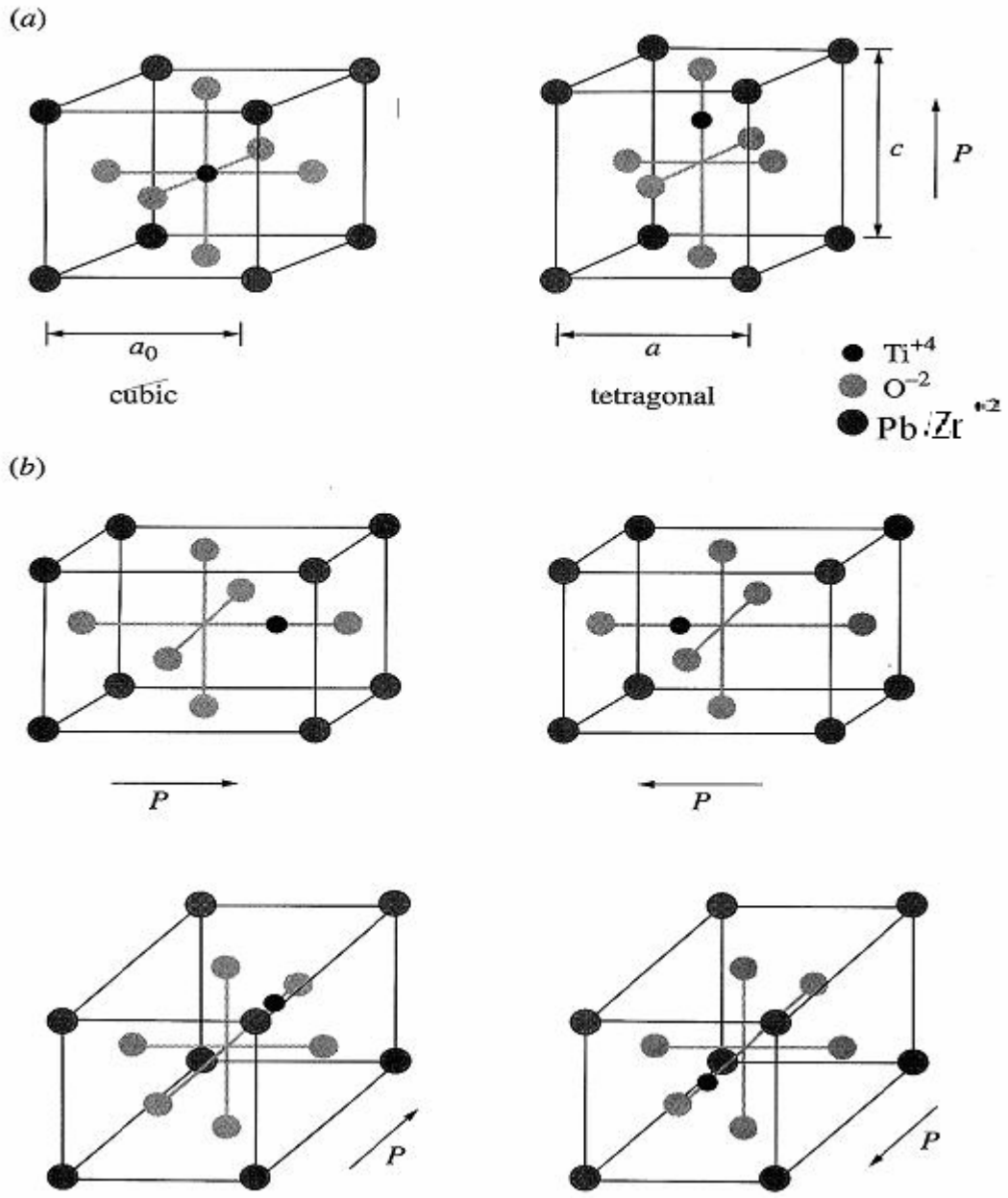

Fig 3.6 (a) Spontaneous Polarization of a PZT crystal from its unpoled state. (b) Reorientation of the domain under a compressive stress or a perpendicular electric field. [2]

3.4 Classification of PZTs

The PZT ceramics can be classified into two groups: hard PZT and soft PZT, refer to the ferroelectric properties, i.e. the mobility of the dipoles or domains and hence also to the polarization / depolarization behavior. The materials are doped with small amounts of substitutional materials to harden them (acceptor, usually iron) or soften them (donor, usually niobium) [7]. The hard PZT are characterized by a low domain mobility and resulting “ferroelectrically hard” behavior such as relatively hard polarization. Therefore, it typically can withstand high electric field and mechanical load. However, they offer lower piezoelectric coefficients and lower dielectric loss. On the other hand, soft piezoelectrics have lower coercive fields, higher piezoelectric coefficients and higher dielectric loss. The soft PZT is easily depolarized by mechanical loads or by an electrical field. The piezoelectric coefficient of soft PZT may be larger, but the piezoelectric effect saturates at higher field levels.

3.5 Piezoelectric Composites

Piezoelectric composites have found a numbers of applications in industries, but only a limited study has been done to explore their nonlinear electro-mechanical coupling behavior.

In this part we will review some of the basic concepts of piezoelectric composites: sum and product properties, combination properties, connectivity patterns and stress

concentration.

3.5.1 Sum and Product Properties

Van Suchtelen [92] introduced the basic ideas of sum and product properties of composites. For a sum property, the composite property coefficient depends on the corresponding coefficients of its constituent phases. Thus the stiffness of a composite is governed by the elastic stiffness of its component phases. Product properties are more complex and more interesting involving different properties in its constituent phases with the interactions between the phases often causing unexpected results. Some popular sum and product properties are listed as following:

Dielectric constant is a simple and useful sum property. Series and parallel mixing rules for dielectric constants are shown in fig 3.7. The dielectric constants K_A and K_B of the two phases and their volume concentration V_A and V_B are involved in the mixing rules. When plotted as a function of composition, the dielectric constant of the composite K, decreases smoothly from K_A to its minimum value at K_B.

A product property utilizes different properties in the two phases of a composite to produce yet a third property through the interaction of the two phases. By combining different properties of two or more constituents, surprisingly large product properties are sometimes obtained with a composite. Indeed, in a few cases, product properties are found in composites which are entirely absent in the phases making up the composites. A few of hundreds of possible product properties are listed in Table 3.1.

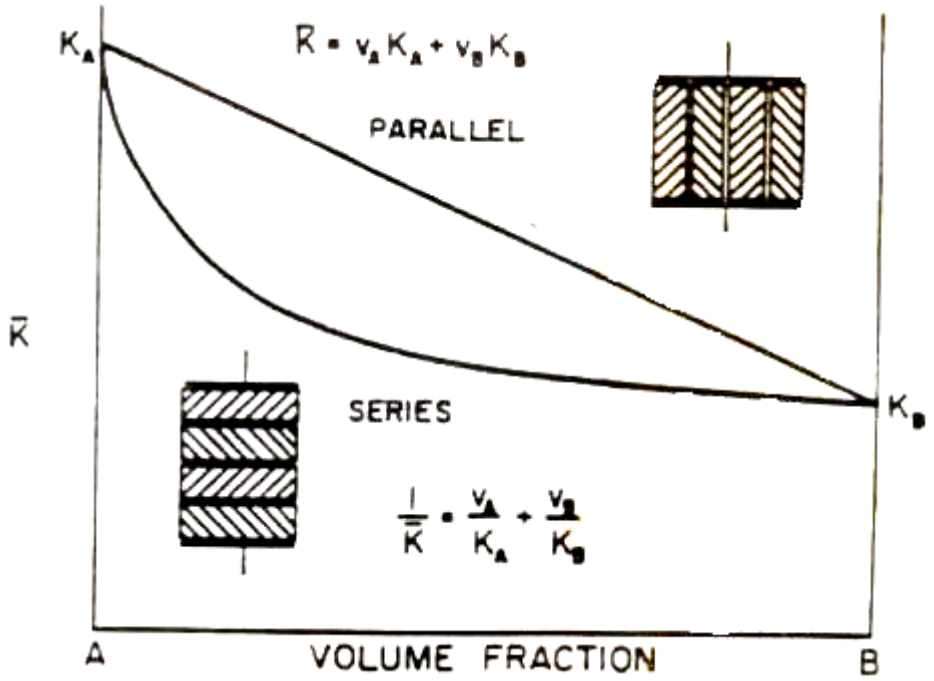

Fig 3.7 Dielectric constant plotted as a function of composition for series and parallel mixing [93]

Property of phase I	Property of phase II	Composite product property
Thermal expansion	Electrical Conductivity	Thermistor
Magnetostriction	Piezoelectricity	Magnetoelectricity
Hall effect	Electrical conductivity	Magnetoresistance
Photoconductivity	Electrostriction	Photostriction
Superconductivity	Adiabatic demagnetization	Electrothermal effect
Piezoelectricity	Thermal Expansion	Pyroelectricity

Table 3.1 Examples of product properties [93]

3.5.2 Combination Properties

Generally, the properties of the composites lie between those of its constituent phases due to the simple mixing rules. However, this is not true for combination properties which involve two or more coefficients. For example, Poisson's ratio is a combination property since it is identical to the ratio of two compliance coefficients. As we known, the value of Poisson' ratio for some composite are extremely smaller than those of the materials used to make the composite.

In electronic applications, the acoustic wave velocity determines the resonant frequency of piezoelectric devices. Fiber-reinforced composites often have very anisotropic wave velocities. In a long and thin rod, the velocity of waves propagating along the length of the rod is $v = (E/\rho)^{1/2}$, where E is Young's modulus and ρ is the density. The long and thin rods embedded from the composite have different properties when the fibers are oriented parallel or perpendicular to the length of the rod. The wave velocities for longitudinal orientation of the fibers are much faster than that for transverse orientation (Fig 3.8).

The wave velocity for the longitudinal fibers v_L is

$$v_L = \sqrt{\frac{(E_f - E_m)v_f + E_m}{(\rho_f - \rho_m)v_f + \rho_m}} \tag{3-7}$$

and the wave velocity for the transverse fibers v_T is

$$v_T = \sqrt{\frac{E_m(1 + 2nv_f)}{\rho_m + (\rho_f - \rho_m)(1 - nv_f)}} \tag{3-8}$$

where E_f and E_m are the Young's modulus of the fibers and matrix respectively,

ρ_f and ρ_m are the densities, v_f is the fiber volume concentration and where n stands for

$$n = \frac{(E_f / E_m) - 1}{(E_f / E_m) + 2} \tag{3-9}$$

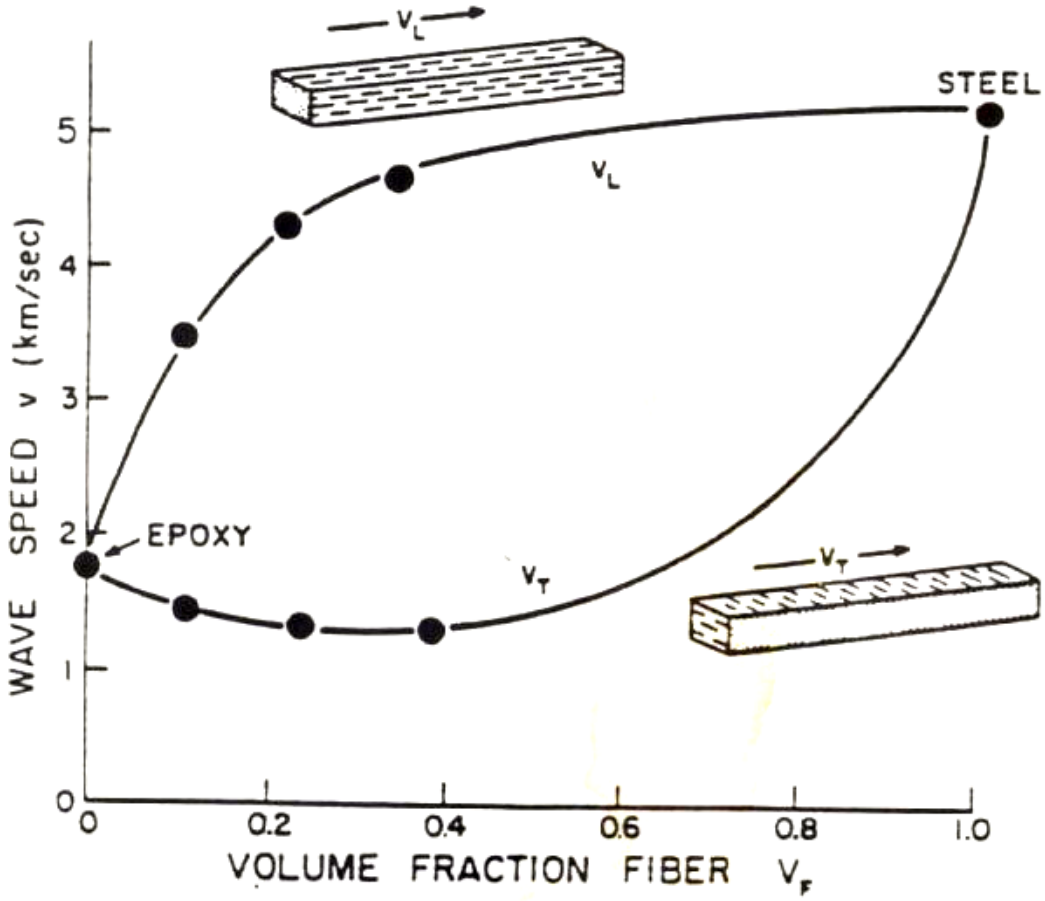

Fig 3.8 Speed of stress waves in composite materials made from steel filaments in epoxy. Waves traveling parallel to the filaments travel faster than transverse waves; the transverse waves are slower than waves in the pure epoxy matrix. [94]

3.5.3 Connectivity

Connectivity [32] is a key feature in property development in multiphase solids since physical properties can change by many orders of magnitude depending on the manner in which connections are made.

Each phase in a composite may be self-connected in zero, one, two or three dimensions. It is natural to confine attention to three perpendicular axes because all property sensors are referred to such systems. If we limit the discussion to diphasic composites, there are ten connectivities: 0-0, 0-1, 0-2, 0-3, 1-1, 1-2, 1-3, 2-2, 2-3, and 3-3. The ten different connectivities are illustrated in Fig 3.9, using a cube as the basic building block. A 1-2 connectivity pattern, for example, has one phase self- connected in two-dimensional chains or fibers. The connectivity patterns are not generally unique. In the case of a 1-2 pattern, the fibers of the second phase might be perpendicular to the layers of the first phase, as in Fig 3.9, or they might be parallel to the layers.

During the past few years, several developing processing techniques have been developed for making piezoelectric composites with different connectivities [95]. The methods include extrusion, tape-casting and replamine.

The 1-3 connectivity pattern in Fig 3.9 is ideally suited by extrusion processing. A ceramic slip is extruded through a die giving a three-dimensionally connected pattern with one-dimensional holes, which can later be filled with a second phase. The1-3 connectivity pattern has the same structure as the aligned fiber-reinforced composite.

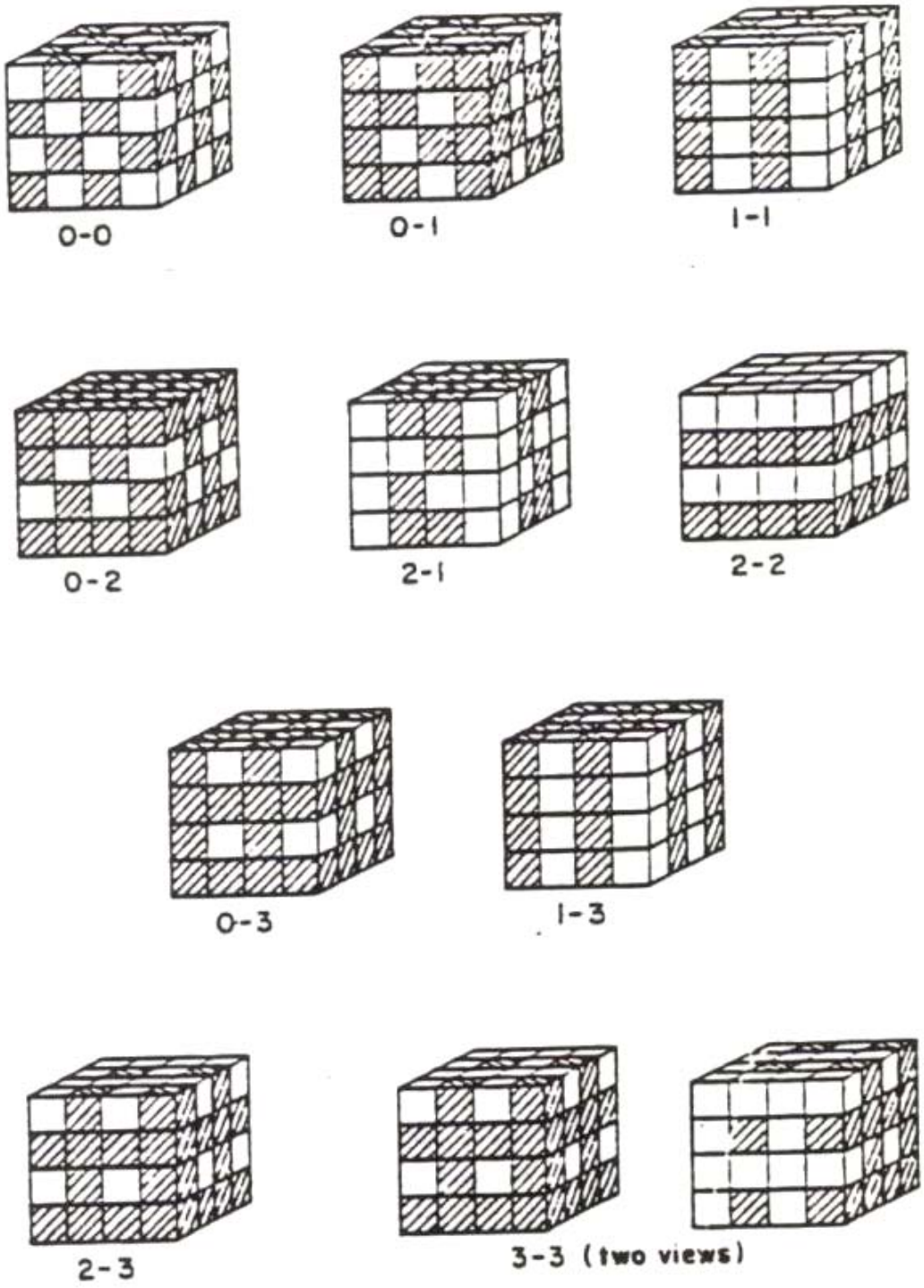

Fig 3.9 Ten connectivity patterns [32]

The tape-casting of multilayer capacitors with alternating layers of metal and ceramic is a way of producing 2-2 connectivity. In this arrangement both phases are self-connected in the lateral X and Y directions but not connected perpendicular to the layer along Z. The lamellar composite is a typical 2-2 pattern.

A 0-3 connectivity pattern has one phase which is three-dimensionally connected. The particle-reinforced composite is 0-3 connectivity pattern.

In 2-3 connectivity, one phase is three-dimensionally connected, the other is two. This pattern can be considered as a modified multilayer pattern with 2-2 connectivity. If the holes are left in the layers of one phase, layers of the second phase can connect through the holes giving three-dimensional connectivity.

The most complicated and in many ways the most interesting pattern is 3-3 connectivity in which the two phases form interpenetrating three-deimensional networks. Patterns of this type often occur in living systems such as coral where organic tissue and an inorganic skeleton interpenetrate one another. These structures can be replicated in other materials using the lost-wax method. The replamine process, as it is called, can also be used to duplicate the connectivity patterns found in foam, wood and other porous materials [96].

3.5.4 Stress Concentration

Stress Concentration is a key feature of many of the piezoelectric composites made from polymers and ferroelectric ceramics [95]. By focusing the stress on the

piezoelectric phase, some of the piezoelectric coefficients can be enhanced and others reduced.

The piezoelectric voltage coefficient $\bar{g}_{33}$ is related electric field to applied stress. Both the tensile stress σ_3 and the resulting electric field E_3 are parallel to the poling direction. If the two phases of the composite are arranged in parallel, the stress acting on the more compliant phase will be transferred to the stiffer phase. Under these conditions, the voltage coefficient $\bar{g}_{33}$ is

$$\bar{g}_{33} = \frac{E_3}{\sigma_3} = \frac{\bar{d}_{33}}{\varepsilon_3} = \frac{V^1 d_{33}^1 s_{33}^2 + V^2 d_{33}^2 s_{33}^1}{(V^1 s_{33}^2 + V^2 s_{33}^1)(V^1 \varepsilon_{33}^1 + V^2 \varepsilon_{33}^2)} \tag{3-10}$$

where $V^1, d_{33}^1, \varepsilon_{33}^1$ and s_{33}^1 represent the volume concentration of phase 1 and its piezoelectric charge coefficient, electric permittivity and elastic compliance. The corresponding properties of the phase 2 are $V^2, d_{33}^2, \varepsilon_{33}^2$ and s_{33}^2.

In a composite, if the ferroelectric ceramic (phase 1) is parallel to the compliant polymer (phase 2), then $d_{33}^1 >> d_{33}^2, s_{33}^1 << s_{33}^2, \varepsilon_{33}^1 << \varepsilon_{33}^2$, and

$$\bar{g}_{33} = \frac{d_{33}^1}{V^1 \varepsilon_{33}^1} = \frac{g_{33}^1}{V^1} \tag{3-11}$$

In this dissertation, we studied the nonlinear electromechanical coupling behavior of 1-3 type of ferroelectric composites due to its wide applications.

4. Experimental Investigation of Ferroelectrics under Multi-axial Mechanical Loading

In this chapter, orientational dependence of electromechaincal coupling behavior of PZT under compressive loading at angle θ in the range 0-90° from the poling direction will be studied experimentally. The experimental investigation for the hard PZT (PZT840) and the soft PZT (PZT850) from APC International, Ltd. will be conducted. The experimental data will be compared to the micromechanical model's results in chapter 5.

4.1 Materials Preparation

Two types of PZT which one is hard (PZT 840), another is soft (PZT 850) were supplied by APC International. Ltd. The manufacturer's properties of the materials are list in Table 4.1.

The full poled parent-specimens of size 100mm x 10mm x 10mm were cut using diamond saw into cuboidal blocks, with the faces of the blocks cut at different angles θ to the polarization direction, as shown in Fig 4.1. 20 specimens were cut for each of θ=0, 30, 45, 60, 90°, making total 100 blocks for all types of PZT. The specimens were polished for smooth surfaces. On each specimen, pairs of faces were electroded with silver paint. The faces on which electrodes were made are chosen in such a way

so that a compressive load could be applied at angles of 0 - 90° to the polarization direction.

Property constants of Materials		PZT 840	PZT850
Relative Dielectric Constant	K^t	1250	1750
Curie Point(°C)	T_c	325	360
Piezoelectric Charge Constant (10^{-12} C/N or 10^{-12} m/V)	d33	290	400
	-d31	125	175
	d15	480	590
Young's Modulus (10^{10}N/m^2)	Y^E_{33}	6.8	5.4
Poisson's ratio	ν	0.31	0.3
Spontaneous polarization (C/ m^2)	Ps	0.2	0.19
Remnant strain	ε_r	0.016	0.003

Table 4.1 Physical and piezoelectric properties of PZT840 & PZT850 [89]

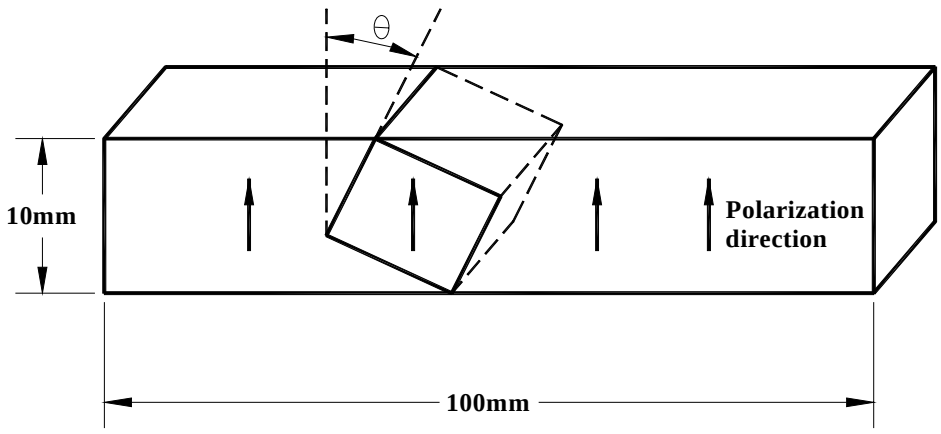

Fig 4.1 Experimental arrangement: cutting a parent poled PZT material into small pieces at angle θ=0°, 30°, 45°, 60°, 90°

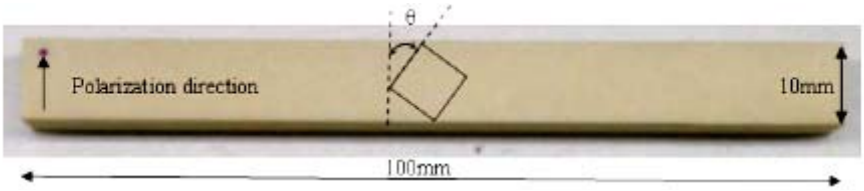

Fig 4.2 The parent-specimen of PZT 850

Fig 4.3 Five small samples with different angles to the poling direction

Fig 4.2 shows the parent-specimen of PZT 850 and Fig 4.3 shows the five small pieces at the angle θ=0, 30, 45, 60, 90° to the polarization direction. Each sample has been polished and electroded with silver paint.

4.2 Experimental Setup

Compressive testing was carried out using INSTRON universal mechanical testing machine Model 5882 with loading capacity of 100KN (Fig 4.4).

As shown in Fig 4.4, the PZT specimen was placed between the two load cells of the Instron 5882. High purity alumina spacers were placed between the specimen and the compression load anvils to ensure the isolation of the electric circuit from the testing machine. A Keithley 6514 electrometer was connected with the same polarity to a 10 μF capacitor to measure the voltage of the specimen. A thin copper strip was placed between the bottom electrode of the specimen and the alumina space. The capacitor was connected to the thin copper and the ground.

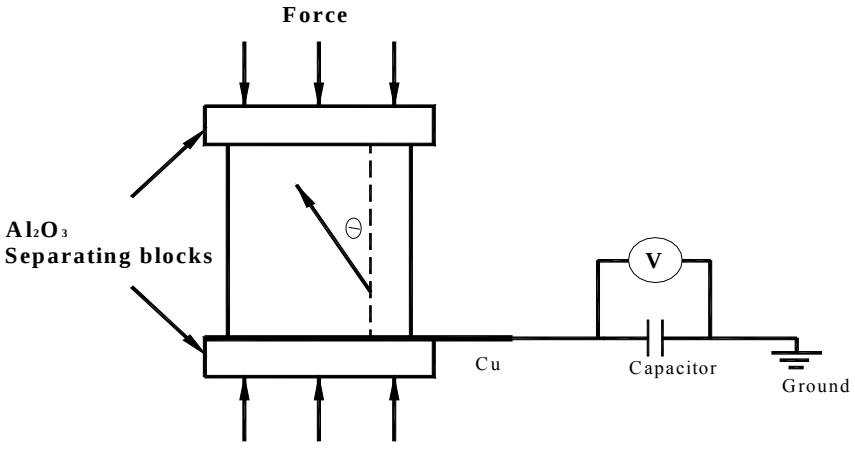

Fig4.4 Experimental setup of PZT specimen under compressive load

The relations of stress vs. strain as well as stress vs. electrical displacement were measured by the setup. The load and the displacement (LVDT) outputs were recorded through the Instron software to the computer. Then the stress is determined from the force divided by the cross sectional area of the specimen. The strain is determined from the value of displacement divided by the length of the specimen. The electrical displacement is equal to the charge per unit area on the electrode. The charge on the electrode is measured by monitoring the voltage of the capacitor. The voltage of the capacitor is monitored by the electrometer and recorded by the Instron software on the computer. The electrical displacement is determined from the capacitivity times voltage divided by the cross sectional area of the specimen.

4.3 Experimental Procedures

Each sample was subjected to a compressive load. The loading path consists of increasing the load from zero to the value at which domain switching finishes and then decreasing back to zero. During the loading procedure data of Load F, displacement Δd and Voltage V were recorded. These data can be converted into stress σ, strain ε and electric displacement D by using the formula follow as

$$\sigma = \frac{F}{A}; \tag{4-1}$$

$$\varepsilon = \frac{\Delta d}{d}; \tag{4-2}$$

$$D = \frac{CV}{A}; \tag{4-3}$$

where A stands for the area of the electroded surface, d stands for the distance

between electrodes and C stands for the capacitance of the capacitor ($C = 10\mu F$ in the test).

4.4 Experimental Results

4.4.1 Stress vs Strain Curve under Applied Compressive Loading

Fig 4.5 and Fig4.6 show the experimental stress- strain relationship of two types of PZT under compressive loading at angle θ (0-90°) from the poling direction. Since there is no or just little domain switch when the applied load is vertical the poling direction (θ=90°), the curve shows the linear piezoelectric response. When the applied load is along the poling direction (θ=0°), the polarization strain due to domain switch reaches the maximum. Between 0° and 90°, the remnant strain decreases with the angle θ increases. In all cases except θ=90° cases, the stress vs strain curves show the nonlinear behavior with the increasing applied load.

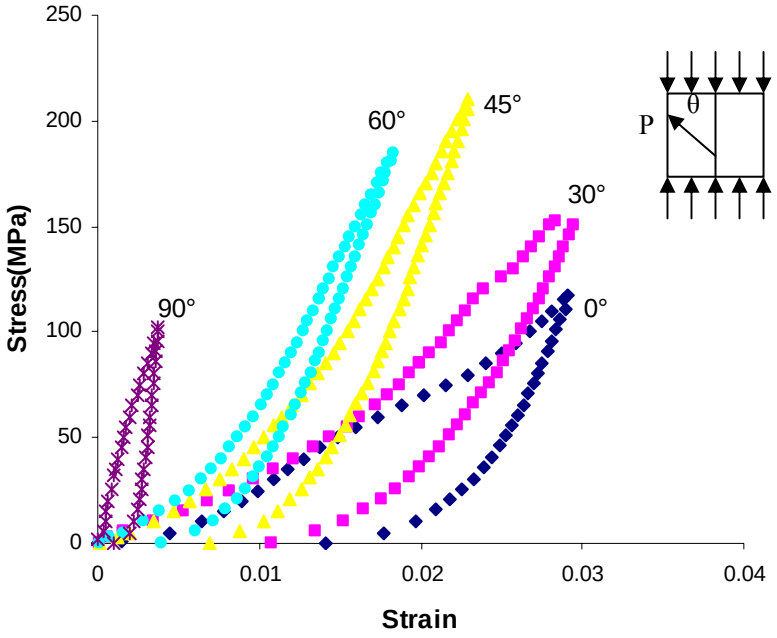

Fig 4.5 Experimental stress-strain relationship of PZT840 applied under compressive loading at an angle θ in the range 0-90° from the poling direction.

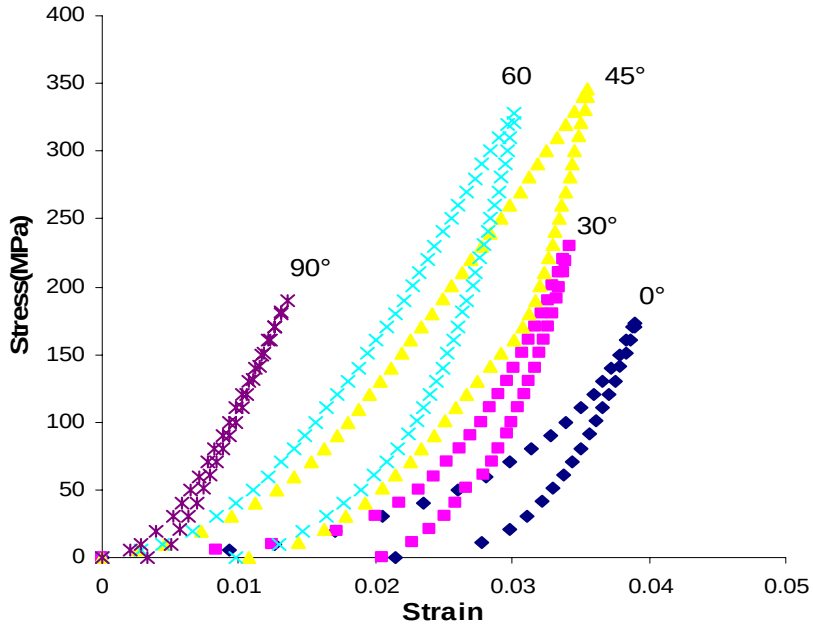

Fig 4.6 Experimental stress-strain relationship of PZT850 applied under compressive loading at an angle θ in the range 0-90° from the poling direction.

4.4.2 Stress vs Electrical Displacement Curve under Applied Compressive Loading

Fig 4.7 and Fig 4.8 show the experimental stress-electrical displacement relationship of the PZTs under compressive loading at an angle θ (0-90°) from the poling direction. Since there is no or just little domain switch when the applied load is vertical the poling direction (θ=90°), the response also shows the linear piezoelectric response. When the applied load is along the poling direction (θ=0°), the maximum change of electric displacement or remnant polarization has been reached. Between 0° and 90°, the remnant polarization increases with the angle θ increases. In all cases except θ=90° cases, the stress vs electrical displacement responses show the nonlinear behavior with increasing the applied load.

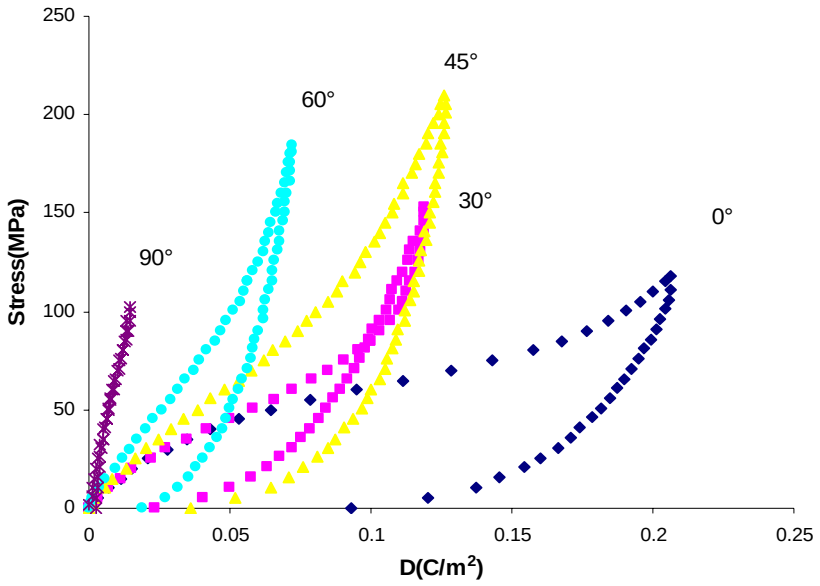

Fig 4.7 Experimental stress-electrical displacement relationship of PZT840 under compressive loading at an angle θ in the range 0-90° from the poling direction.

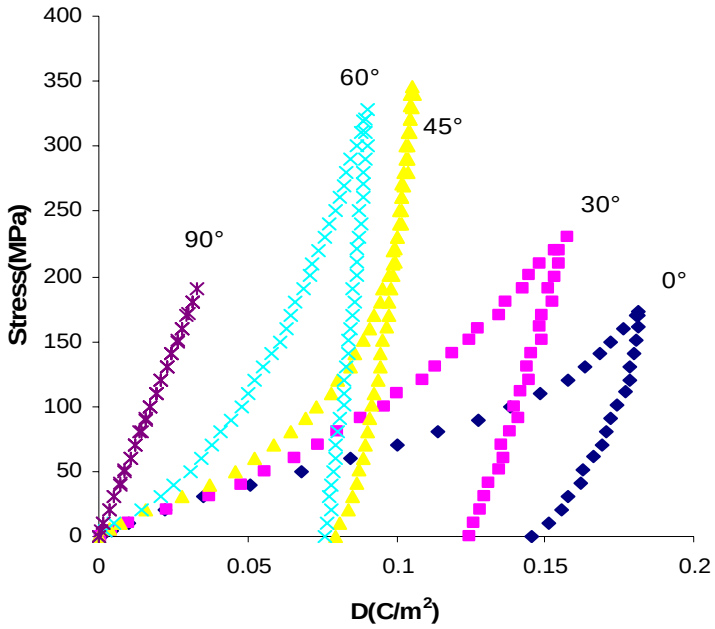

Fig 4.8 Experimental stress-electrical displacement relationship of PZT850 under compressive loading at an angle θ in the range 0-90° from the poling direction.

5. Micromechanical Modeling of Ferroelectrics

Here we extend the micromechanics theory with irreversible thermodynamics principle developed by Li and Weng [1, 2] and Li [30] to study the orientation effects on electromechanical behavior of the PZTs under compression. In this micromechanics model, an equivalent dual-phase system was introduced to define the "effective" domain under different loading conditions. Li [28] has used the model to study the orientation effects on the electrical response of PZT under multiaxial electrical switch. Recently, Su and Weng [97] have also developed a polycrystal model based upon this original micromechanics model to capture more detail information from each individual grain. Due to the simplicity and accuracy of the original model of Li and Weng, we start out from this model to study the orientation effects on electromechanical behavior of ferroelectrics under compressions and compare with our experimental results. In this micromechanics model, the equivalent system can be represented by a two phase composite consisting of the transversely isotropic parent phase and the switched phase. The local and global coordinates in the equivalent system are shown in Fig 5.1, where the original poling direction is along the 3'-axis of the local coordinates and the applied compressive load is along the 3-axis of the global coordinates. The angle between the local 3'-axis and the global 3-axis also coincides with the cutting angle θ to the poling direction. When the

angle θ of applied load to the poling direction is 0° or 90°, the problem reduces to the common uniaxial response of ferroelectrics; in which it has been studied intensively in the literature. Otherwise, it corresponds to orientation dependent response. In the equivalent system, we adopt the lamellar domain structure due to the morphology of the domain switch, in which the piezoelectric Eshelby's S-tensor has been obtained by Li [98]. Before we lay out the entire theory, the eigenfield due to the domain switch in the equivalent system will be discussed.

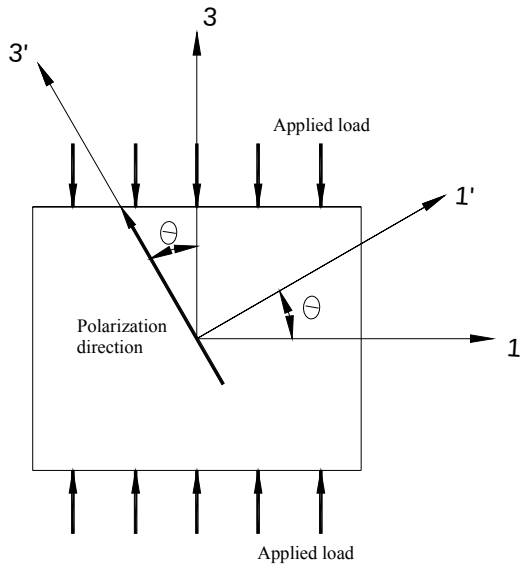

Fig 5.1 Applying compressive loading at an angle θ to the poling direction

5.1 Domain Switch

To be able to use the micromechanics based theory, the eigenfield due to heterogeneous nature of the system needs to be identified and obtained. It has been widely known that the domain switch is the main source of the nonlinear response of

ferroelectrics. For a tetragonal single crystal (i.e. BaTiO3), there are totally six possible domain switch configuration, which include one 180°, four 90° switches, and the original 0° domain. For a polycrystal, the problem becomes more complicated. The different domain switches may happen in any grain with any one of six domain switch configurations depending on the loading conditions. In order to simplify the problem and still capture the key factor of the electromechanical coupling behavior of a ferroelectric polycrystal, an equivalent two-phase system has been introduced by Li [30]. In this equivalent system, the overall effective polarization of the parent phase is treated as an original phase 0, and the new switched domain as phase 1. Then the two-phase composite micromechanics model can be readily applied. In such a system, the effective electric polarization due to the domain switch in the global coordinates can be written as

$$D_{ds} = \begin{bmatrix} -(1-\sin\theta) \\ 0 \\ -\cos\theta \end{bmatrix} P_s \tag{5-1}$$

where P_s is the spontaneous polarization. The corresponding polarization strain (or eigenstrain) is

$$\varepsilon_{ds} = \begin{bmatrix} (1+\upsilon_t)\varepsilon_{33}^s \cos^2\theta & 0 & (1+\upsilon_t)\varepsilon_{33}^s \cos\theta\sin\theta \\ 0 & 0 & 0 \\ (1+\upsilon_t)\varepsilon_{33}^s \cos\theta\sin\theta & 0 & -(1+\upsilon_t)\varepsilon_{33}^s \cos^2\theta \end{bmatrix} \tag{5-2}$$

where ε_{33}^s is the polarization strain due to the spontaneous polarization in the local coordinates.

ν_t is the "transformation" Poisson's ratio during the poling process.

When a fully poled specimen is subjected to compressive loading with an angle of

θ to the poling direction, the change of remnant polarization or the maximum depolarization ΔP in loading direction (axis 3) can be directly obtained as

$$\Delta P = -P_s \cos\theta \tag{5-3}$$

where the spontaneous polarization P_s is set to be the same as the saturation polarization P_{sat}.

Compare the Eq (5-3) with the experiment data of PZT840 and PZT850, the results are shown in Fig 5.2 and Fig 5.3. It is clear that the ΔP in Eq (5-3) is similar to the experimental data, which $P_s = 2.0(C/m^2)$ in PZT 840; $P_s = 1.8(C/m^2)$ in PZT 850.

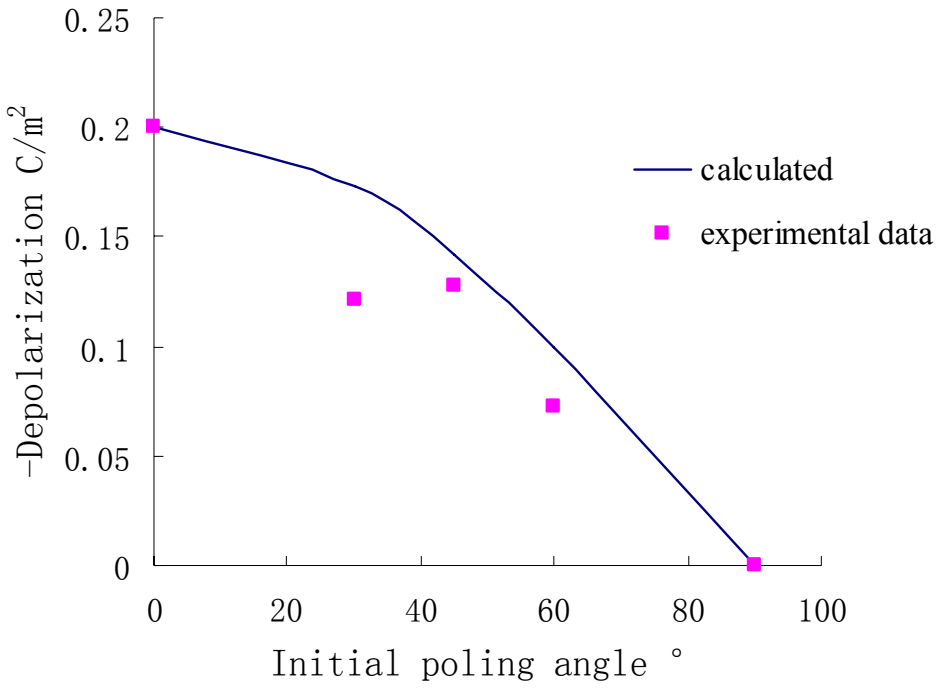

Fig 5.2 Comparison between Eq.(5-3) and the experimental data of PZT 840 for the maximum depolarization in terms of the angle θ of applied compressive load to the initial poling direction

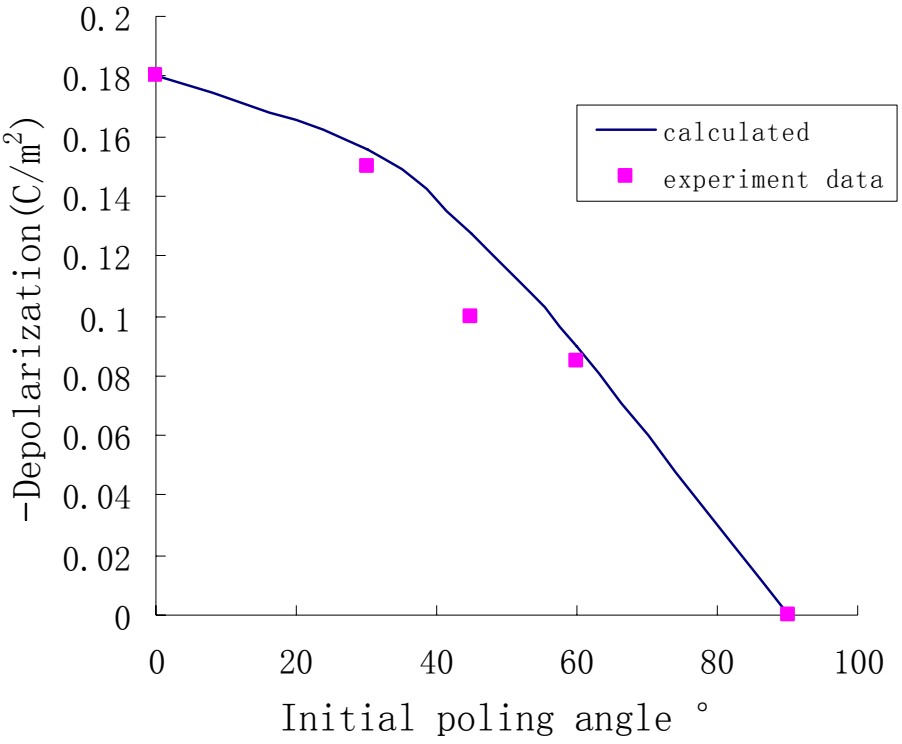

Fig 5.3 Comparison between Eq.(5-3) and the experimental data of PZT 850 for the maximum depolarization in terms of the angle θ of applied compressive load to the initial poling direction

As described in Eq. (5-1) and Eq. (5-2), the eigenpolarization and eigenstrain are represented by the change of the dipole moment and polarization strain of a unit cell in PZT ceramic between the original and the final positions.

5.2 Constitutive Equations

Most ferroelectric ceramics exhibit a linear piezoelectric effect at a small loading range. In the absence of body force and free charge density,

$$\nabla \cdot \sigma = 0, \nabla \cdot D = 0 \tag{5-4}$$

where σ is the stress and D is the electric displacement. Under the small strain assumption,

$$\varepsilon = \frac{1}{2}[\nabla u + (\nabla u)^T], E = -\nabla \Phi \tag{5-5}$$

where ε, E represent strain and electric field respectively, u, Φ represent displacement and electric potential respectively.

The coupled linear constitutive equations of a ferroelectric material can be written as

$$\begin{bmatrix} \varepsilon \\ D \end{bmatrix} = \begin{bmatrix} s & d \\ d & k \end{bmatrix} \begin{bmatrix} \sigma \\ E \end{bmatrix} \tag{5-6}$$

where s, d and k stand for the elastic compliances tensor (under a constant electric field), piezoelectric moduli tensor, and dielectric permittivity tensor (under a constant stress) respectively.

For convenience Eq. (5-6) can be rewritten in the unified form

$$Y = MX \quad \text{or} \quad Y_i = M_{ij} X_j, \text{ sum over } i, j = 1,...,9 \tag{5-7}$$

Where, in Nye's (1979) contracted notation,

$$\left.\begin{aligned} Y &= (\varepsilon_1, \varepsilon_2, \varepsilon_3, \varepsilon_4, \varepsilon_5, \varepsilon_6, D_1, D_2, D_3)^T \\ X &= (\sigma_1, \sigma_2, \sigma_3, \sigma_4, \sigma_5, \sigma_6, E_1, E_2, E_3)^T \end{aligned}\right\} \tag{5-8}$$

And M is the electromechanical compliances matrix. PZT has the class 6-mm-symmetry, so the overall properties for a fully poled PZT are transversely isotropic. The components of M can be written as

$$M_0 = \begin{bmatrix} s_{11} & s_{12} & s_{13} & 0 & 0 & 0 & 0 & 0 & d_{31} \\ s_{12} & s_{11} & s_{13} & 0 & 0 & 0 & 0 & 0 & d_{31} \\ s_{13} & s_{13} & s_{33} & 0 & 0 & 0 & 0 & 0 & d_{33} \\ 0 & 0 & 0 & s_{44} & 0 & 0 & 0 & d_{15} & 0 \\ 0 & 0 & 0 & 0 & s_{44} & 0 & d_{15} & 0 & 0 \\ 0 & 0 & 0 & 0 & 0 & s_{66} & 0 & 0 & 0 \\ 0 & 0 & 0 & 0 & d_{15} & 0 & k_{11} & 0 & 0 \\ 0 & 0 & 0 & d_{15} & 0 & 0 & 0 & k_{11} & 0 \\ d_{31} & d_{31} & d_{33} & 0 & 0 & 0 & 0 & 0 & k_{13} \end{bmatrix} \quad (5\text{-}9)$$

where $s_{66} = 2(s_{11} - s_{12})$ and 3 direction is taken to be the symmetric axis. Hence ten independent electromechanical constants exist in this matrix.

The subscript 0 in M_0 represents this set of components refer to the fully poled parent ceramic.

The inverse of the constitutive relation in Eq. (5-7) can be obtained as

$$X = LY \quad \text{or} \quad X_i = L_{ij} Y_j, \text{ sum over } \; i, j = 1,2,...,9 \quad (5\text{-}10)$$

where L carries the unified moduli tensor and $L = M^{-1}$. During the summation, the indices associated with the stress or strain run from 1 to 6, on the other hand those associated with the electric fields run from 1 to 3, corresponding to 7 to 9 in the unified expression in terms of X and Y.

5.3 Gibb's Free Energy and Kinetic Equation of Domain Switching

The nonlinear coupling behavior of ferroelectric materials is due to the domain switch. In the equivalent system, once the domain switch starts, the ceramic becomes a composite material which consists of the parent phase and the newly switched domain phase. The transversely isotropic parent phase with the original poling

direction is considered as phase 0 and the new domain as phase 1. The volume concentration of the new domain is denoted as c_1 ($c_1 + c_0 = 1$).

To establish the kinetic equation, recall the Gibbs' free energy [16]. Upon application of the external field $\overline{X} = (\overline{\sigma}, \overline{E})^T$, the Gibbs' free energy with a new domain (volume concentration is c1) due to domain switch $Y_{ds} = (\varepsilon_{ds}, D_{ds})^T$ is given by

$$G(\overline{X}, c_1) = \frac{1}{2}\int_V X^T (Y - Y_{ds}) dV - \overline{X}^T Y \tag{5-11}$$

where $\overline{Y} = (\overline{\varepsilon}, \overline{D})^T$ is the overall strain and electric displacement response of the equivalent system.

The Gibbs' free energy of parent domain without domain switching is give by

$$G_0(\overline{X}) = \frac{1}{2}\int_V X^T Y dV - \overline{X}^T \overline{Y_0} = -\frac{1}{2}\overline{X}^T \overline{Y_0} \tag{5-12}$$

where $\overline{Y_0} = (\overline{\varepsilon_0}, \overline{D_0})^T$ is the overall electromechanical response of this homogeneous solid, given by $\overline{Y_0} = M_0 \overline{X}$

It is the change that stands for the driving force for the nucleation and growth of the new domain in the irreversible thermodynamics. The difference in Gibbs' free energy would be

$$\Delta G = G - G_0 \tag{5-13}$$

Once the domain switch is considered and the Mori and Tanaka's micromechanics method [49] in the formulation of the inclusion type problem is used. The change of Gibbs' free energy in the matrix notation can be written by

$$\Delta G = -\frac{1}{2} c_1 (\widetilde{X} + \overline{X}^{pt}) Y_{ds} - \frac{1}{2} c_1 \overline{X}^T (2Y_{ds} + Y^*) \tag{5-14}$$

where

$$(\widetilde{X} + \overline{X}^{pt}) = [B_1(c_1B_1 + c_0I)^{-1} - I]\overline{X} + [B_1(c_1B_1 + c_0I)^{-1} - I]B_1L_0(I - S)Y_{ds},$$
$$Y^* = -[(L_1 - L_0)(c_1I + c_0S) + L_0]^{-1}(L_1 - L_0)[L_0^{-1}\overline{X} - c_0(I - S)Y_{ds}], \quad (5\text{-}15)$$
$$B_1 = [I + L_0(I - S)(L_0^{-1} - L_1^{-1})]^{-1}.$$

In these equations, $\widetilde{X}$ is the difference between the average X of the parent domain and the applied $\overline{X}$, and $\overline{X}^{pt}$ is the difference between the average X of the parent domain and that of the new domain. Tensor B_1 represents the electromechanical field concentration tensor of a single inclusion (with L_1) embedded in the infinite matrix (with L_0) under an applied $\overline{X}$. S is the Eshelby-type tensor in the electromechanical context. The component of the orientation-dependent S tensor is given by Li [98].

In irreversible thermodynamics, the microstructure is now represented by c_1. Under a constant applied field $\overline{X}$, the second law requires in an irreversible thermodynamic process that [99]

$$\left.\frac{\partial \Delta G(\overline{X}_{ij}, c_1)}{\partial c_1}\right|_{\overline{X}} dc_1 \le 0 \quad (5\text{-}16)$$

where the equality holds only for a reversible process ($dc_1 = 0$).

Then the thermodynamic driving force of domain switch is

$$f_{ds} = -\left.\frac{\partial \Delta G}{\partial c_1}\right|_{\overline{X}} \quad \text{or}$$

$$f_{ds} = \frac{1}{2}(\overline{X}^T A\overline{X} + \overline{X}BY_{ds} + Y_{ds}^T CY_{ds}) \quad (5\text{-}17)$$

where A, B, and C are 9 X 9 matrices. They are, respectively

$$A = A_1L_0^{-1}[c_1A_1(I - S) - I],$$

$$B = [B_1(c_1B_1 + c_0I)]^T - c_1[B_1(c_1B_1 + c_0I)^{-2}(B_1 - I)]^T + I + [(1-2c_1)I - c_1c_0A_1(I-S)]A(I-S),$$

$$C^T = c_1B_1(c_1B_1 + c_0I)^{-1}B_1L_0(I-S)[2I - c_1(c_1B_1 + c_0I)^{-1}(B_1 - I)] - B_1L_0(I-S), \quad (5\text{-}18)$$

with

$$A_1 = [\Delta L(c_1I + c_0S) + L_0]^{-1}\Delta L, \text{ and}$$

$$\Delta L = L_1 - L_0 \quad (5\text{-}19)$$

When piezoelectric moduli L_1 and L_0 do not differ from each other along the loading direction, the kinetic can be more explicit. In this case, $\Delta L = 0$ and as a result the equivalent eigenfield Y^* in Eq. (4-13) goes zero and $B_1 = I$ as well. Hence the Eq (4-15) reduces to

$$f_{ds} = \overline{X}^T Y_{ds} - \frac{1}{2}(1-2c_1)Y_{ds}^T[L_0(I-S)]^T Y_{ds} \quad (5\text{-}20)$$

Domain switch needs to overcome a resistance force which is from two sources: the surface energy of domain walls ΔG^s and the energy dissipation accompanied by the movement of domain wall ΔG^d. The surface energy is

$$\Delta G^s = \gamma_s A_1 = c_1\gamma_s(A_1/V_1) = 2c_1\gamma_s/t \quad (5\text{-}21)$$

where γ_s stands for the interface energy density, A_1 stands for the interface area, V_1 stands for the total volume of the new domain in a unit volume of the system and t stands for the average thickness of the new domain.

The dissipation energy is obtained as

$$\Delta G^d = m(e^{b_0c_1} + e^{-b_1c_1} - 2) \quad (5\text{-}22)$$

where m, b_0, and b_1 are constants. Both b_0 and b_1 represent the rate of domain switching and parameter m characterize the dissipation energy at the end of the

domain switch ($c_1 = 1$). These three parameters may be different under multiaxial compressive loads. Then the resistance force follows as

$$R_{ds} = \frac{\partial(\Delta G^s + \Delta G^d)}{\partial c_1} = \frac{2\gamma_s}{t} + m(b_0 e^{b_0 c_1} - b_1 e^{b_1 c_1}) \tag{5-23}$$

The driving force must overcome the resistance force, and then the kinetic equation of domain growth is cast into

$$f_{ds} = R_{ds} \tag{5-24}$$

Substituting Eq.(5-17) and (5-23) into Eq.(5-24), the explicit kinetic equation is recast into

$$\frac{1}{2}(\overline{X}^T A\overline{X} + \overline{X}BY_{ds} + Y_{ds}^T CY_{ds}) = \frac{2\gamma_s}{t} + m(b_0 e^{b_0 c_1} - b_1 e^{b_1 c_1}) \tag{5-25}$$

At the onset (or start) of domain switch (c_1=0), the corresponding applied field as $\overline{X}_s$ is denoted. Eq.(5-25) can be rewritten without surface energy term as

$$(\overline{X}^T - X_s^T)Y_{ds} + c_1 Y_{ds}^T (I - S)^T L_0{}^T Y_{ds} = m(b_0(e^{b_0 c_1} - 1) - b_1(e^{b_1 c_1} - 1)) \tag{5-26}$$

With the constants b_0 and b_1 in dissipation energy, this kinetic equation (5-26) provides the value of c_1 at a given load $\overline{X}$.

Once the volume concentration c_1 is known, the overall response of the equivalent system follows from

$$\overline{Y} = M_0 \overline{X} + c_1(Y_{ds} + Y^*) \tag{5-27}$$

When piezoelectric moduli L_1 and L_0 do not differ from each other along the loading direction, $\Delta L = 0$ and as a result the equivalent eigenfield Y^* in Eq. (5-27) goes zero.

$$\overline{Y} = M_0 \overline{X} + c_1 Y_{ds} \tag{5-28}$$

5.4 Nonlinear Stress vs Strain and Stress vs Electric Displacement Relation under Compressive Loading

The stress-strain and stress-electric displacement responses are calculated by the micromechanics model for the set of specimens poled at angles of 0-90°, then compared with the experimental data. Some materials properties have been changed since the materials were cut into small pieces. Therefore, the piezoelectric charge constant d_{33} and Young's modulus Y_{33}^{E} have been re-measured. For PZT 840, the measured piezoelectric charge constant $d_{33} = 145 \times 10^{-12}$ C/N and the measured Young's modulus $Y_{33}^{E} = 2.8 \times 10^{10}$ N/m. For PZT 850, $d_{33} = 174 \times 10^{-12}$ C/N, $Y_{33}^{E} = 1.4 \times 10^{10}$ N/m. The measured values were adopted in the calculation of micromechanical modeling.

The results for PZT 840 show in Fig 5.4 and Fig 5.5. The Comparison of stress and electrical displacement relationship between calculation of micromechanics model and the experimental data is shown in Fig 5.4. And then the comparison of stress and strain relationship is shown in Fig 5.5.

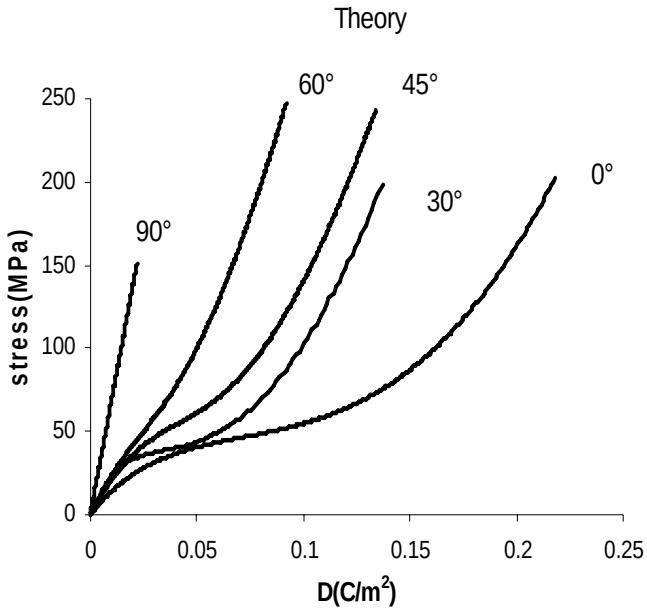

(a) Theory

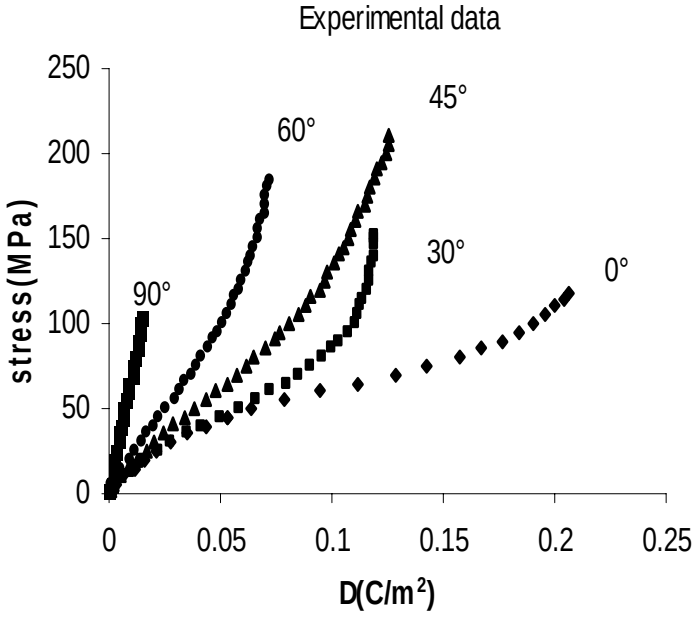

(b) Experimental data

Fig 5.4 Comparison for stress-electrical displacement relation (PZT840) between calculation of micromechanics model (a) and the experimental data (b)

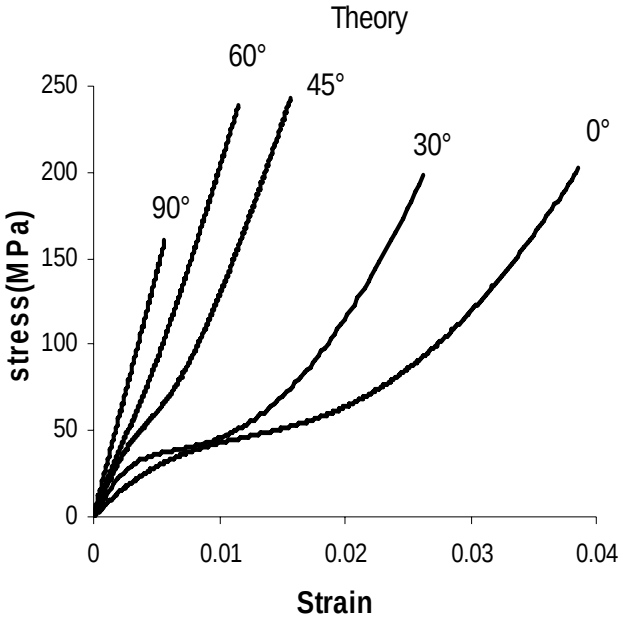

(a) Theory

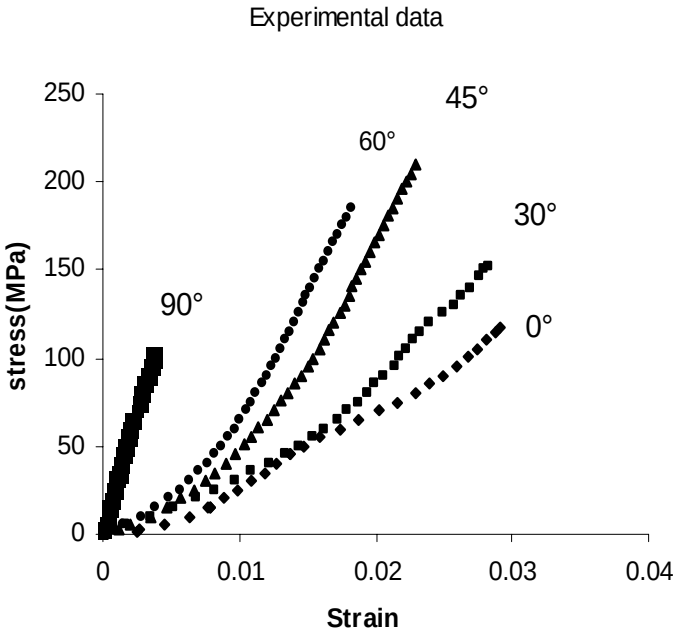

(b) Experimental data

Fig 5.5 Comparison for stress-strain relation (PZT840) between calculation of micromechanics model and the experimental data

The results for PZT 850 show in Fig 5.6 and Fig 5.7

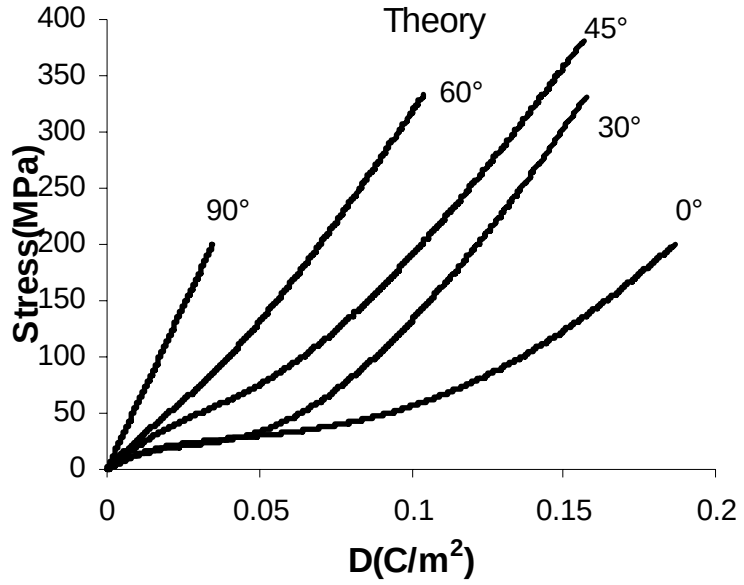

(a) Theory

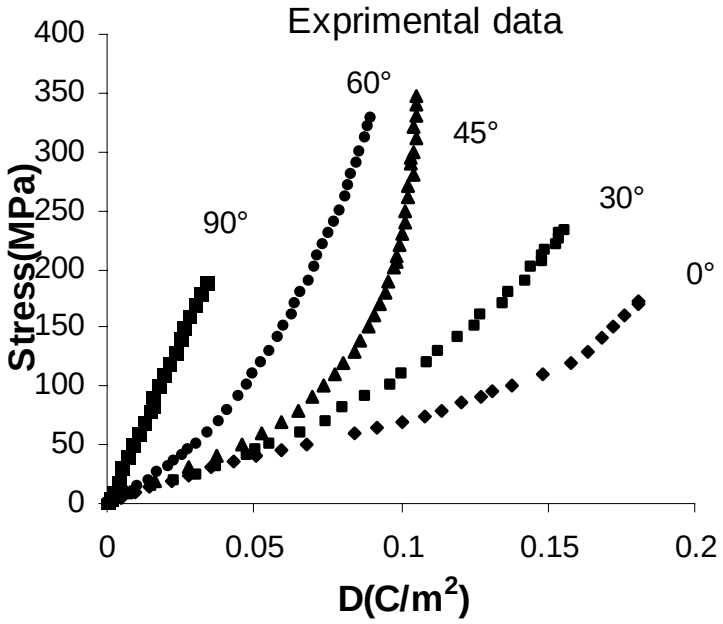

(b) Experimental data

Fig 5.6 Comparison for stress-electrical displacement relation (PZT850) between calculations of micromechanics model (a) and the experimental data (b)

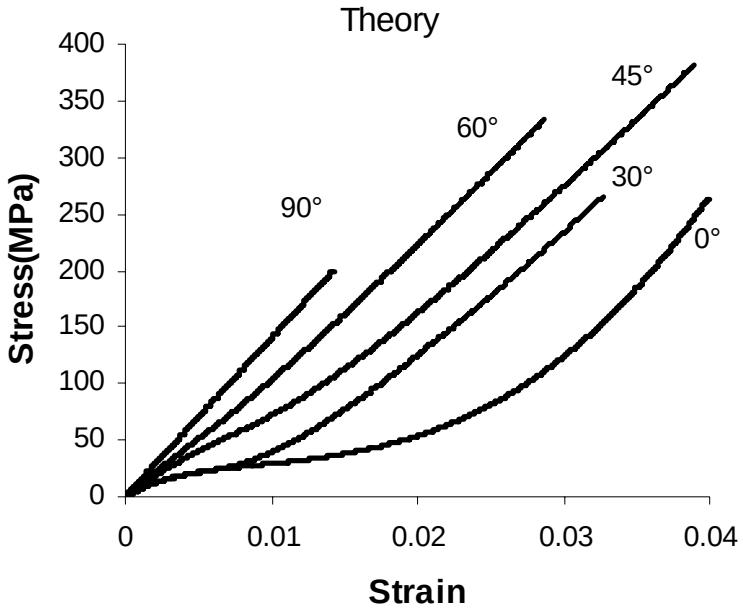

(a) Theory

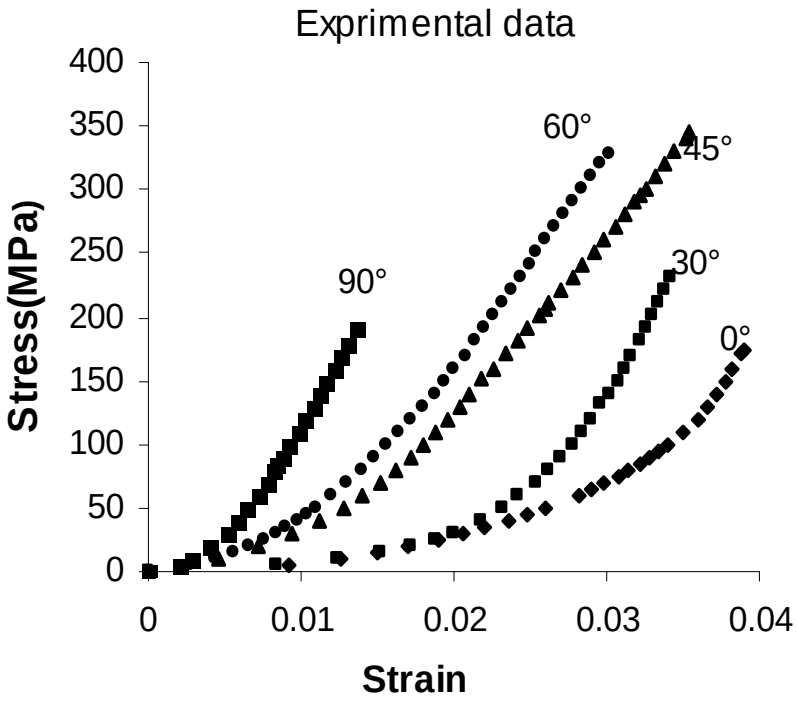

(b) Experimental data

Fig 5.7 Comparison for stress-strain relation (PZT850) between calculations of micromechanics model (a) and the experimental data (b)

5.5 Discussion and Conclusions

Now we compare the calculation of the micromechanical model and the experimental data. From Fig 5.4 to Fig 5.7, it is clear that both experimental data and calculation results for θ=90° show linear relationship since no or little domain switch happen in this case. When θ=0°, at which the applied load is along the poling direction, the maximum polarization reached the spontaneous polarization P_s. In the stress vs electric displacement response, it shows that the calculation and experimental data are pretty much consistent although there are some discrepancies.

In the stress vs strain response, it shows calculation and experimental data does not match very well. The possible reasons are

(a) The strain channel of the machine has trouble.

(b) LVDT is not very accurate for the case of very small deformation

(c) Alumina often breaks during the test

The modified micromechanical model which is based on the irreversible thermodynamics principle, physics of domain switch, and mechanics of homogenization introduces a dual-phase equivalent system. This equivalent system takes the orientation average over the entire system, instead of taking into account each individual domain switch in each grain of the polycrystal. In such a simplified approach, the key response of ferroelectric materials under the multiaxial loads can be captured. The results are found to be in satisfactory agreement with the experimental data of stress and electrical displacement although the stress-strain response does not

fit very well because of some reasons mentioned above.

6. Experimental Investigations of Piezoelectric Composites

In this chapter, the effect of orientation on electro-mechanical coupling behavior of piezoelectric composite under compressive loading and electric field at angle θ in the range 0-90° from the poling direction is studied experimentally. The piezoelectric composite system has 1-3 type of connectivity with 65% PZT5A1 fibers in an epoxy matrix.

6.1 Materials Preparation

PZT5A1 piezoelectric composites are supplied by Smart Material Corp, which the inclusion is PZT5A1 and the matrix is epoxy. The manufacturer's published properties of the piezocreramic are list in Table 6.1.

To be able to study the orientation effect on electromechanical coupling behavior of the composite system, the samples were cut into cuboidal specimens. The cutting angle with respect to the poling PZT fiber direction is ranged from 30°, 45° and 60°, respectively. The schematic sketch on cutting angle is shown in Fig. 6.1. For 0° specimens, we purchased the10mm x 10mm x 10mm blocks with gold sputtering electrodes on both top and bottom surfaces directly from the manufacture without cutting. The original 100mm x 10mm x 10mm 1-3 PZT composite bar and the 0° cubic blocks with other angle arrangements after cutting are shown in Fig. 6.2.

Piezoceramic	**Symbol**	**unit**	**5A1**
Electrical Properties			
Permittivity/1kHz	$\varepsilon_{33}^{T} / \varepsilon_{0}$		1850
Dielectric dissipation factor/1kHz	$\tan\delta$		0.012
Curie temperature	T_c	^{o}C	335
Electromechanical Properties			
Coupling factors	k_p		0.62
	k_{31}		0.33
	k_{33}		0.72
	k_{15}		0.74
Piezoelectric charge coefficients	d33	10^{-12}C/N	440
	-d31		185
	d15		560
Piezoelectric voltage coefficients	g33	10^{-3}Vm/N	25.5
Mechanical Properties			
Compliance	s^{E}_{11}	10^{-12} m^2/N	18.5
	s^{E}_{33}		20.7

Table 6.1 Physical and piezoelectric properties of PZT5A1 [103]

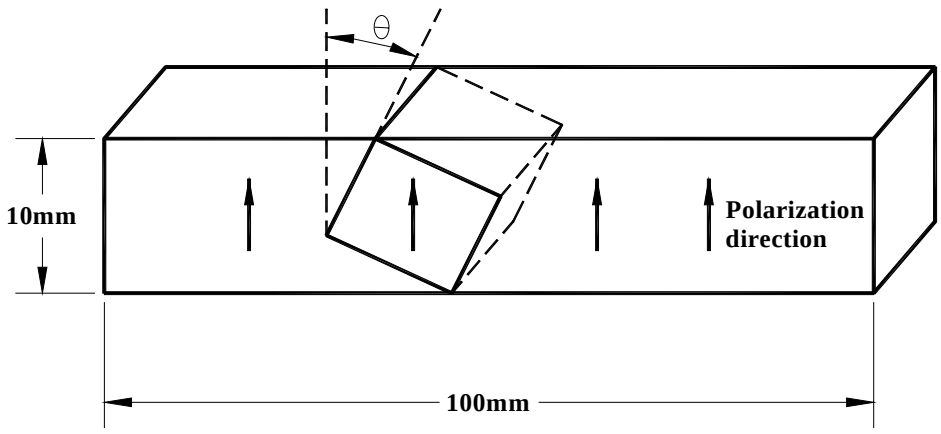

Fig 6.1 Experimental arrangement: cutting a parent poled PZT5A1 composite into small pieces at angle θ = 30°, 45°, 60°

(a) Original fully poled PZT5A1 composite bar

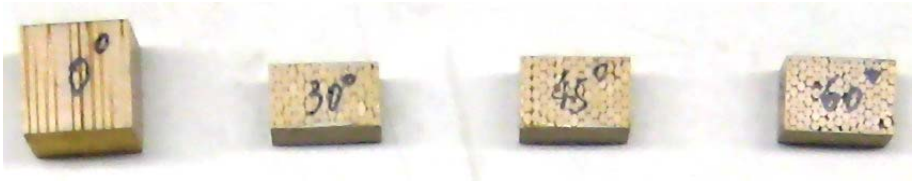

(b) Testing specimens with different angles to the poling fiber direction at θ=0°, 30°, 45°, 60°

Fig 6.2 PZT5A1/epoxy composites samples

The cut specimens were polished lightly for uniform surfaces. On each specimen, pairs of faces are electroded with silver paint. The faces on which electrodes were made are chosen in such a way that a compressive load could be applied at angles of 0 - 60° to the polarization direction.

6.2 Experimental Setup

6.2.1. Compressive Loading

Similar to the PZT ceramics tests, an INSTRON universal mechanical testing machine Model 5882 with loading capacity of 100KN was used for compressive tests. As shown in Fig 6.3, the PZT5A1 composite specimen is placed between the two load cells. Two high purity alumina spacers were placed between the specimen and the compression load cells to isolate the electric circuit from the testing machine. Keithley 6514 electrometer was connected with the same polarity to a 10 μF capacitor to measure the voltage of the specimen. A thin copper strip was placed between the bottom electrode of the specimen and the alumina spacing. The capacitor was connected to the thin copper and the ground.

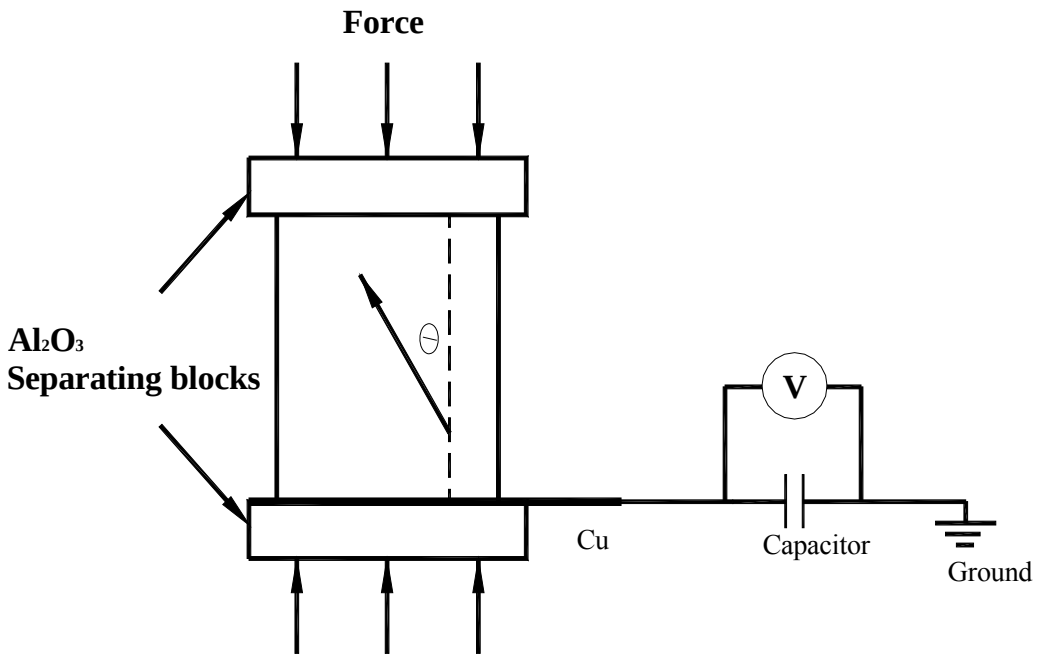

Fig 6.3 Experimental setup of PZT5A1 piezoelectric composite specimen under compressive load

The curves of stress vs. strain as well as stress vs. electrical displacement are determined under compression. Upon the compressive loading, the displacement is measured by Linear Variable Differential Transformer (LVDT), while the voltage of the capacitor is measured by Keithley 6514 electrometer. Both the applied load and the output from LVDT are recorded through the Instron software. The stress is determined from the force divided by the cross sectional area of the specimen. The strain is determined from the value of the displacement measured by LVDT divided by the length of the specimen. The electrical displacement is equal to the charge per unit area on the electrode. The electrical displacement is determined from the capacity times voltage divided by the cross sectional area of the specimen.

6.2.2 Electric Field Loading

For coupling behavior of piezoelectric composites, under electric field loading, a TREK high voltage amplifier model 30/20 (Fig 6.5) was used as electric field supply. A customized specimen holding apparatus was built. As shown in Fig 6.4, the PZT5A1 composite specimen is placed between two high purity alumina spacers. The specimen is immersed in a silicon oil bath to prevent the electric arcing. The thin copper strips are placed between the electrode of the specimen and the alumina spacing. The Model 30/20 high voltage power amplifier, which provides precise control of output voltages in the range of 0 to $\pm$ 30kV applies the electric field through the top thin copper. A 10 μF capacitor is connected to the bottom thin copper and the ground. Keithley 6514 electrometer is connected with the same polarity to the capacitor to measure the voltage of the capacitor. The longitudinal displacement is measured by the MTI-2000 Fotonic^{TM} sensor from MTI Instruments, Inc. All data are recorded. This electric loading system is settled on the VIBRAPLANE Model 9100/9200 Vibration Isolation Table from Kinetic System, INC (Fig 6.6), which will absorb the vibration in the tests to get more accurate data.

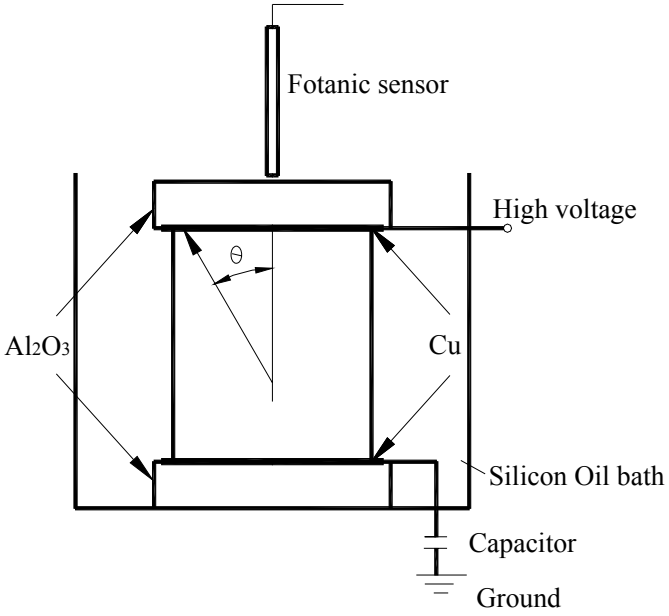

Fig 6.4 Experimental setup of PZT5A1 piezoelectric composite specimen under electric loading

Fig 6.5 Model 30/20 high-voltage power amplifier

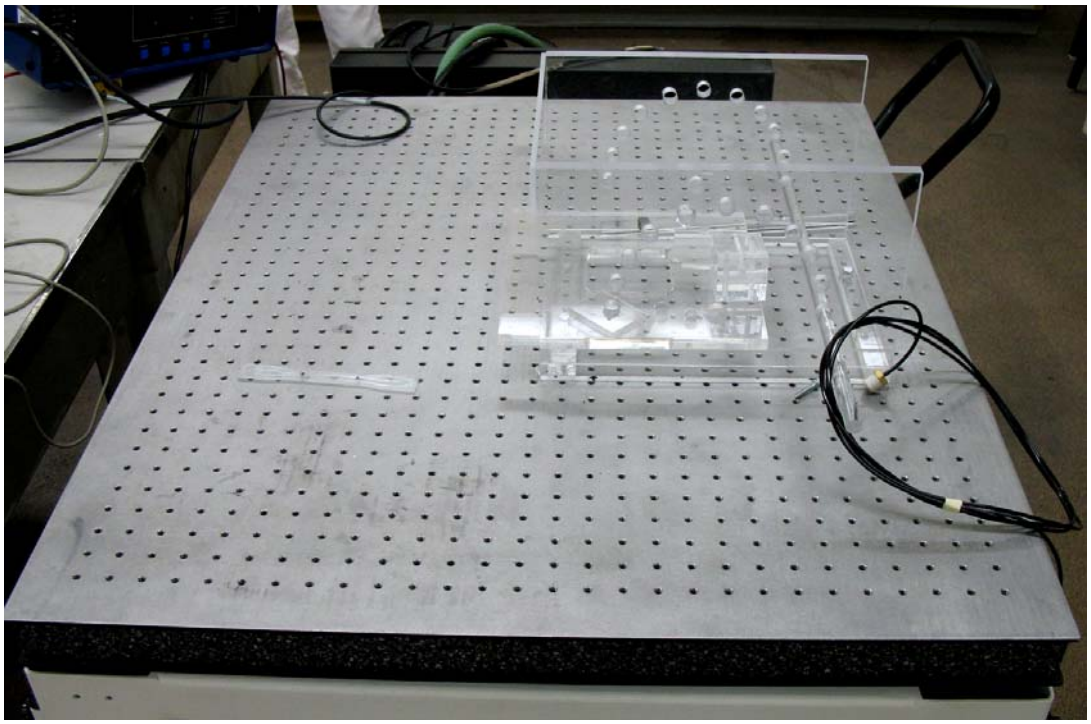

Fig 6.6 VIBRAPLANE Model 9100/9200 Vibration Isolation Table

The curves of electrical displacement vs. electric field as well as electrical displacement vs. strain are determined by the setup. Upon the electric field, the longitudinal displacement of the specimen is measured by the MTI-2000 Fotonic^{TM} sensor, where the voltage of the capacitor is measured by Keithley 6514 electrometer. Both the applied high voltage and the output from Fotonice senser are recorded through the Labview Program. The electrical displacement is equal to the charge per unit area on the electrode. The electrical displacement is determined from the capacity times voltage divided by the cross sectional area of the specimen. The electric field is determined from the high voltage divided by the cross sectional area of the specimen. The strain is determined from the value of longitudinal displacement divided by the length of the specimen.

6.3. Experimental Procedures

6.3.1 Procedures under Compression

Each specimen is subjected to a compressive load with 100 KN maximum load capacity. The loading path consists of increasing the load from zero to the value at which domain switching finishes and then decreasing back to zero. During the loading procedure data of Load F, displacement Δd and Voltage of capacitor V_c are recorded.

These data can be converted into stress σ, strain ε, electric displacement D by using the formula as follows

$$\sigma = \frac{F}{A}; \tag{6-1}$$

$$\varepsilon = \frac{\Delta d}{d}; \tag{6-2}$$

$$D = \frac{CV_c}{A}; \tag{6-3}$$

where A stands for the cross sectional area of the specimen, d stands for the distance between electrodes and C stands for the capacitance of the capacitor ($C = 10\mu F$ in the test).

6.3.2 Procedures under Electric Field

The generator created a triangular wave voltage with frequency is 1/30 Hz so that the voltage source can be received from the high-voltage power amplifier which can

amplify the original voltage 3000 times. By multiplying this voltage signal by 3000 times and divide it by the thickness of specimen, the applied electric field of 2MV/m and 1/30Hz is obtained. The voltage loading path is increasing the electric field strength from 0 to 2 MV/m, then decreasing back to zero and then reverse in the opposite direction. After several cycles, a stable hysteresis loop develops. The displacement of specimen under the electric loading is measured by Fotnic optic sensor. The voltage of capacitor is measured by Keithley electrometer.

During the loading procedure data of high voltage V, displacement Δd and Voltage of capacitor V_c are recorded using Labview.

These data can be converted into strain ε, electric displacement D by using Eq.(6-2) and Eq. (6-3). Then electric field E can be obtained by

$$E = \frac{V}{d} \tag{6-4}$$

6.4. Experimental Results

6.4.1 Under Compressive Loading

a) Stress-Strain Curve

Fig 6.7 shows the experimental stress-strain relationship of PZT5A1 composite under compressive load at angle θ (0-60°) from the poling direction. When the applied load is along the poling direction (θ=0°), the polarization strain due to

spontaneous polarization reaches the maximum. Between 0° and 90°, the remnant strain decreases with the angle θ increases. In all cases, the stress vs strain curves show the nonlinear behavior with the increasing applied load. At a 90°, only linear elastic behavior has revealed due to difficulty of domain switch along that direction.

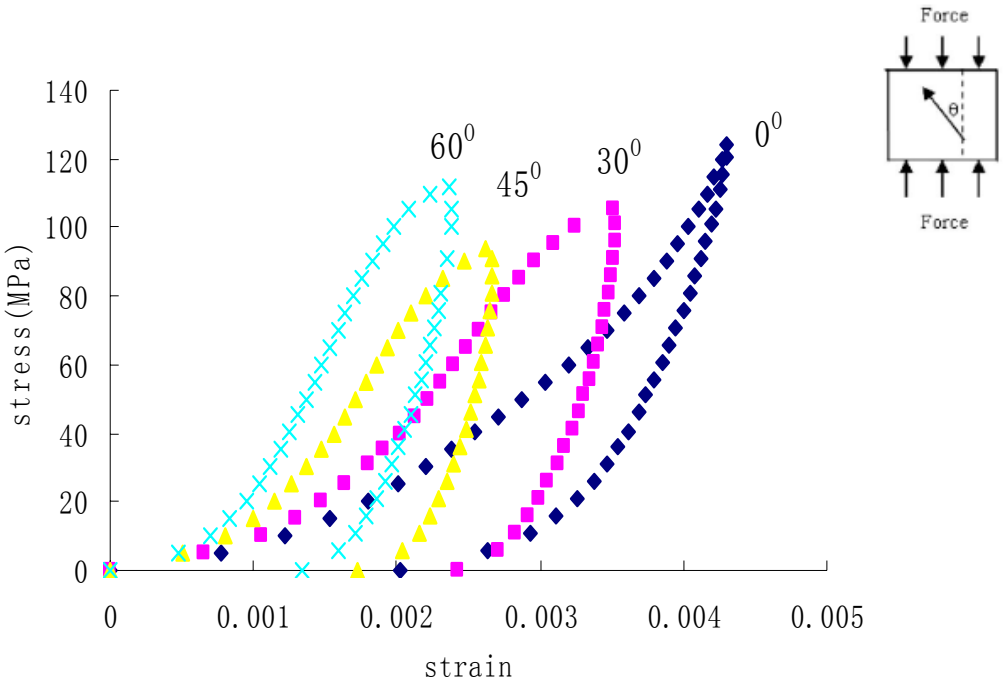

Fig 6.7 Experimental stress-strain relationship of PZT5A1 composite applied under compressive load at angle θ in the range 0-60° from the poling direction.

b) Stress- Electrical Displacement Curve

Fig 6.8 shows the experimental stress-electrical displacement relationship of PZT under compressive load at angle θ (0-60°) from the poling direction. When the applied load is along the poling direction (θ=0°), the maximum change of electric displacement or remnant polarization has been reached. Between 0° and 90°, the

remnant polarization decreases with the angle θ increases. In all cases, the stress vs electrical displacement responses show the nonlinear behavior with increasing the applied load. For a 90° angle, the electric displacement reduces to zero due to the lack of domain switch. The behavior of the system is dominated by elastic properties of the composite.

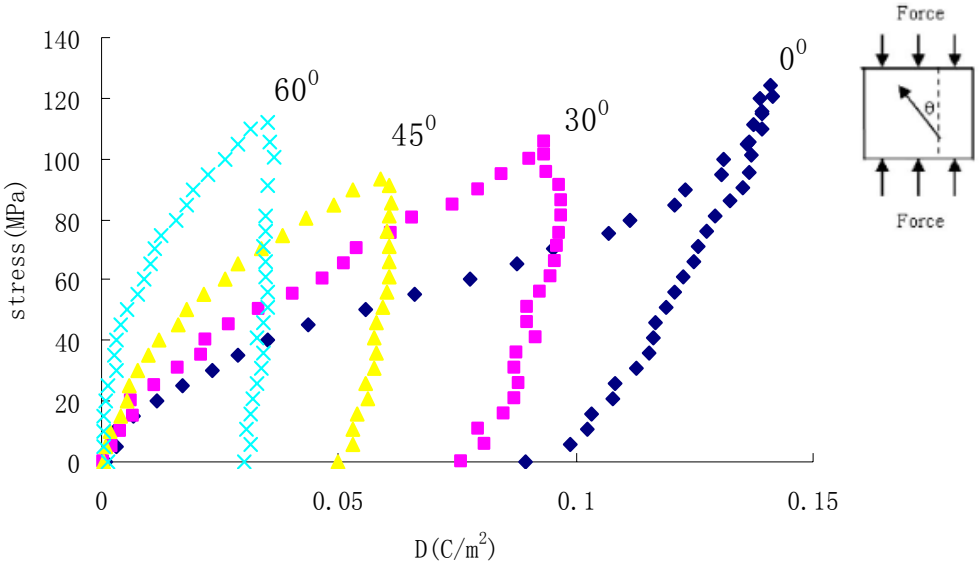

Fig 6.8 Experimental stress-electrical displacement relation of PZT5A1 composite under compressive load at angle θ in the range 0-60° from the poling direction.

6.4.2 Under Electric Field Loading

Under the electric field loading, all tests run about 10-30 cycles in the range of ±2 KV/m. After the initial cycle, the hysteresis loops of electric field vs electric displacement are stabilized and repeatable.

a) Electric Field- Electric Displacement Curves

Fig 6.9-6.12 show the hysteresis loops of electric field and electric displacement under electric field loading with the angles ranging from 0°, 30°，45° to 60° toward the fiber direction.

At 0° angle which represents the common uniaxial electric field loading, the electric hysteresis loop of the composite is similar to the ones of PZT ceramic. When the electric field reaches zero, the remnant polarization is around 0.9 C/m^2.

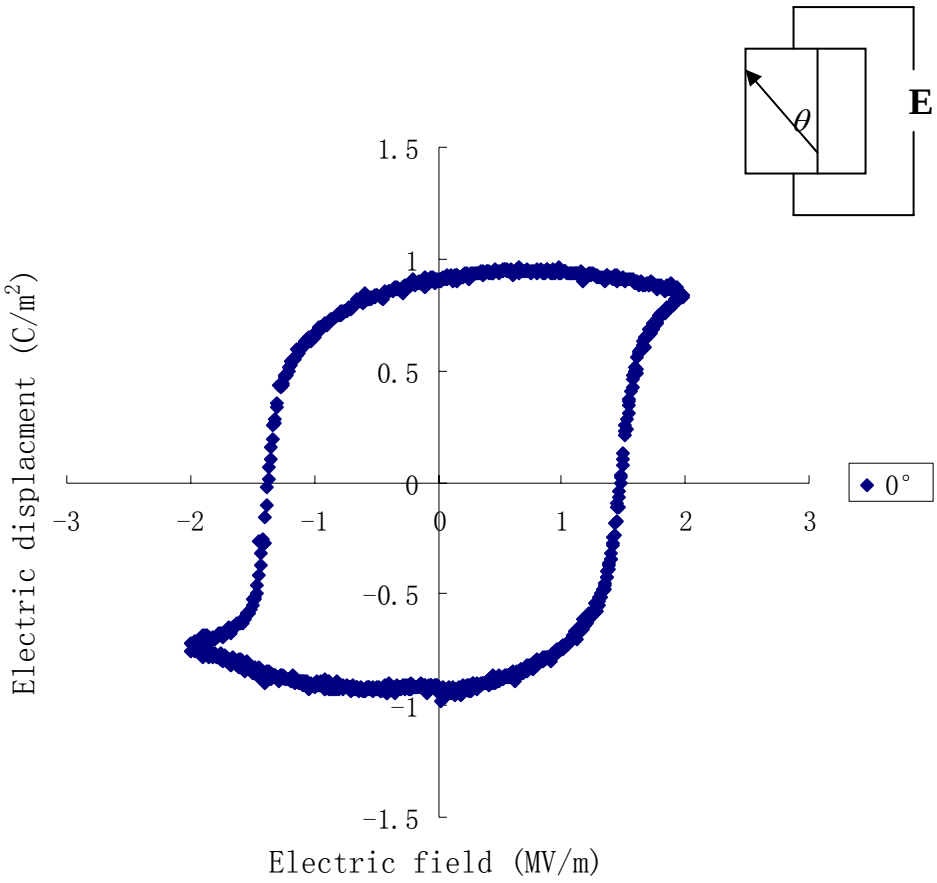

Fig 6.9 Electric displacement vs electric field hysteresis loop at $\theta = 0°$

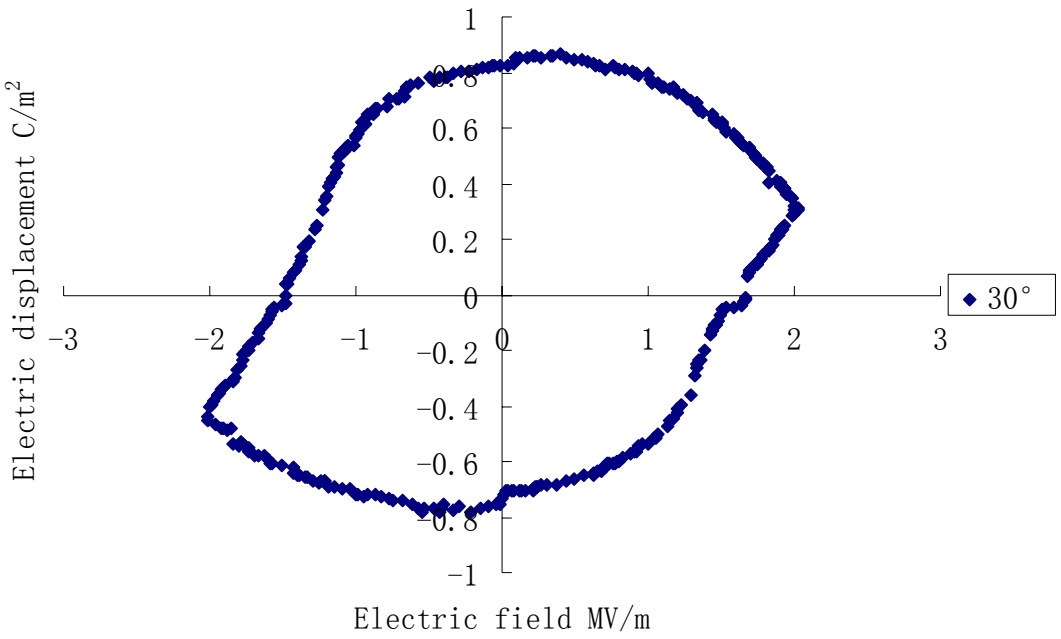

Fig 6.10 Electric displacement vs electric field hysteresis loop at $\theta = 30°$

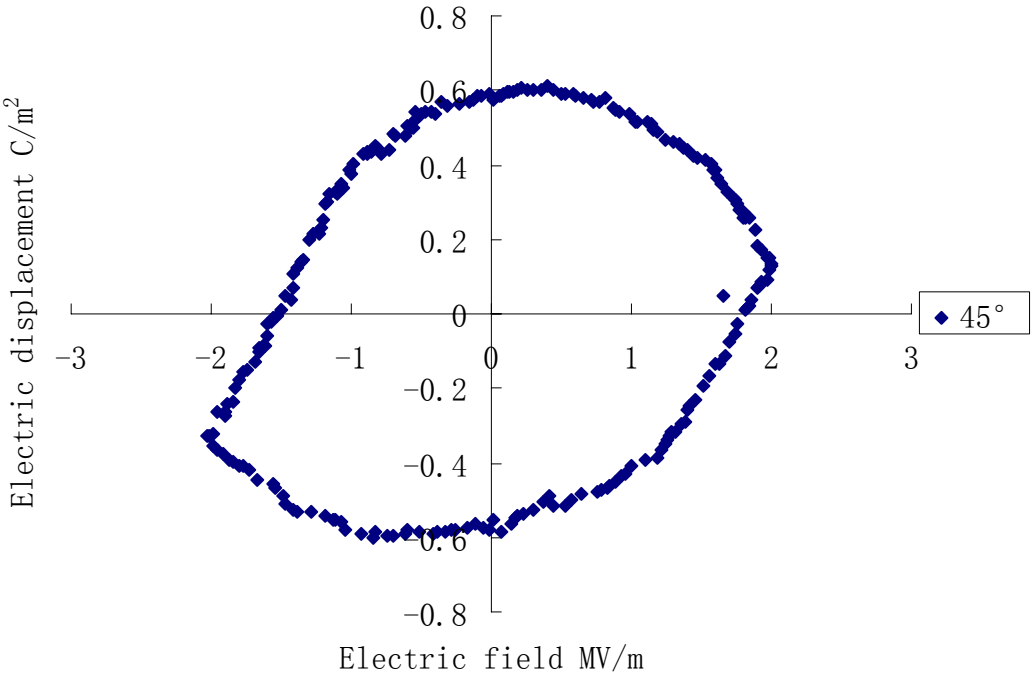

Fig 6.11 Electric displacement vs electric field hysteresis loop at $\theta = 45°$

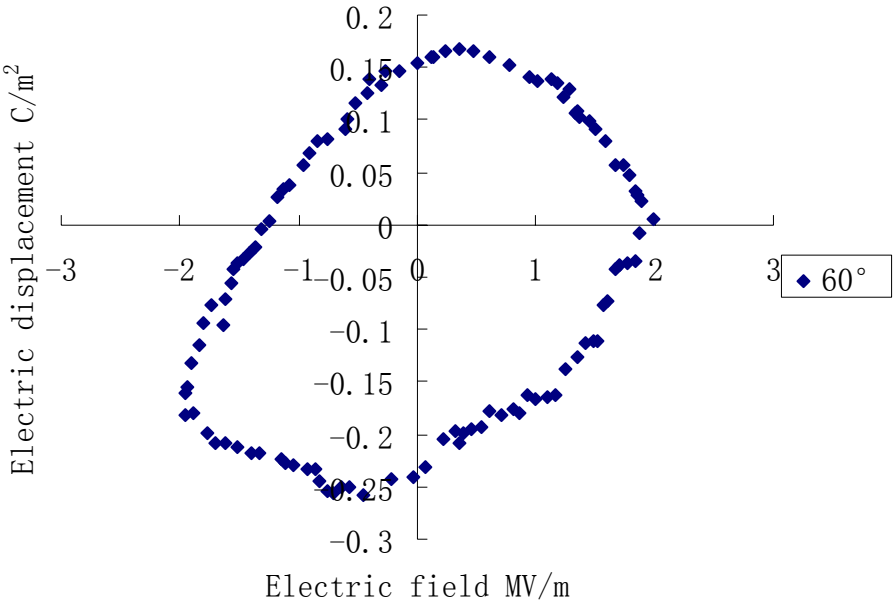

Fig 6.12 Electric displacement vs electric field hysteresis loop at $\theta = 60°$

When the angle between electric field loading direction to the poling fiber direction increases, the electric connectivity decreases and the remenant polarization reduces. The comparison among the different angles is shown in Fig 6.13. The tests at 90° were conducted, however it does not show any hysteresis since the epoxy matrix isolates the PZT fibers from the testing system. Fig 6.14 shows the change of the remenant polarization in term of angle θ=0°, 30°, 45°, 60° and 90°. At 0° angle, the remenant polarization reaches the maxium, and then it decreases while the angle increases till it reaches zero at 90°.

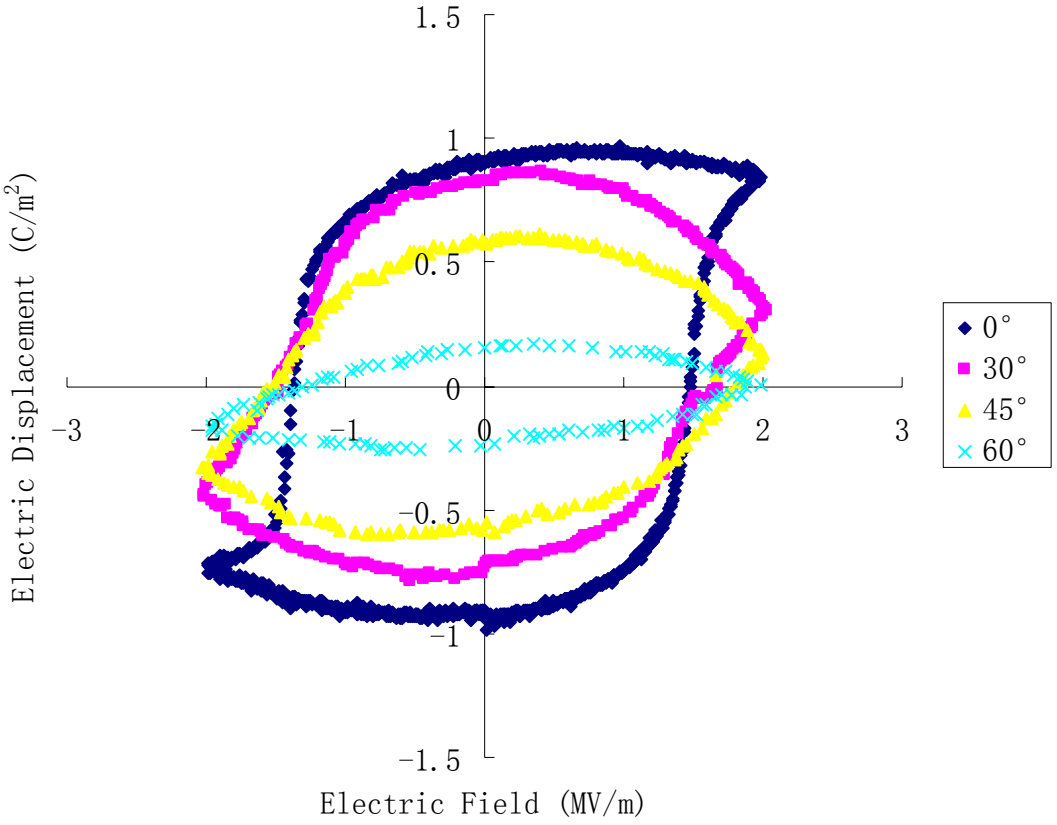

Fig 6.13 Comparison of the hysteresis loops of electric displacement and electric field at θ=0°, 30°, 45°, 60°

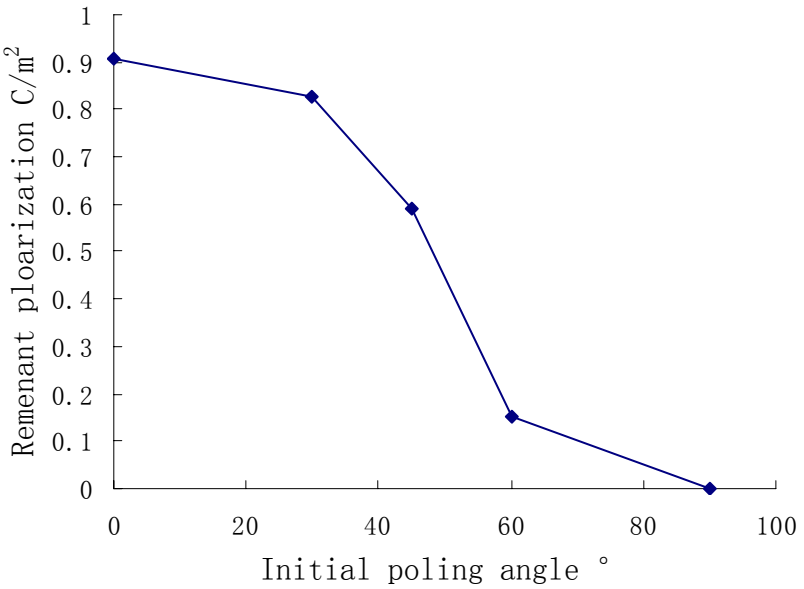

Fig 6.14 Change of the remenant polarization in term of angle θ

b) Electric Field -Strain Curve

Fig 6.15-6.18 shows the relation between electric field and strain under electric loading with the angles ranging 0°, 30°，45° and 60° toward the fiber direction which is also the poling direction. At 0° angle, the remnant strain is around 0.006 %.

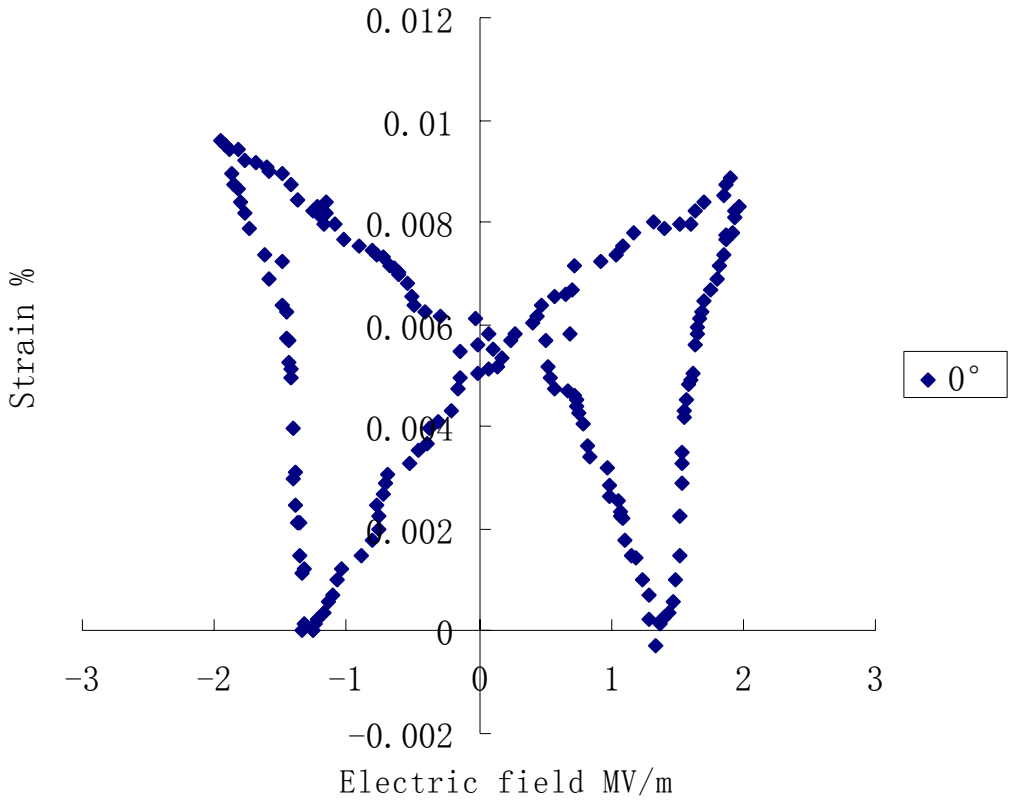

Fig 6.15 Electric field vs strain hysteresis loop at $\theta = 0°$

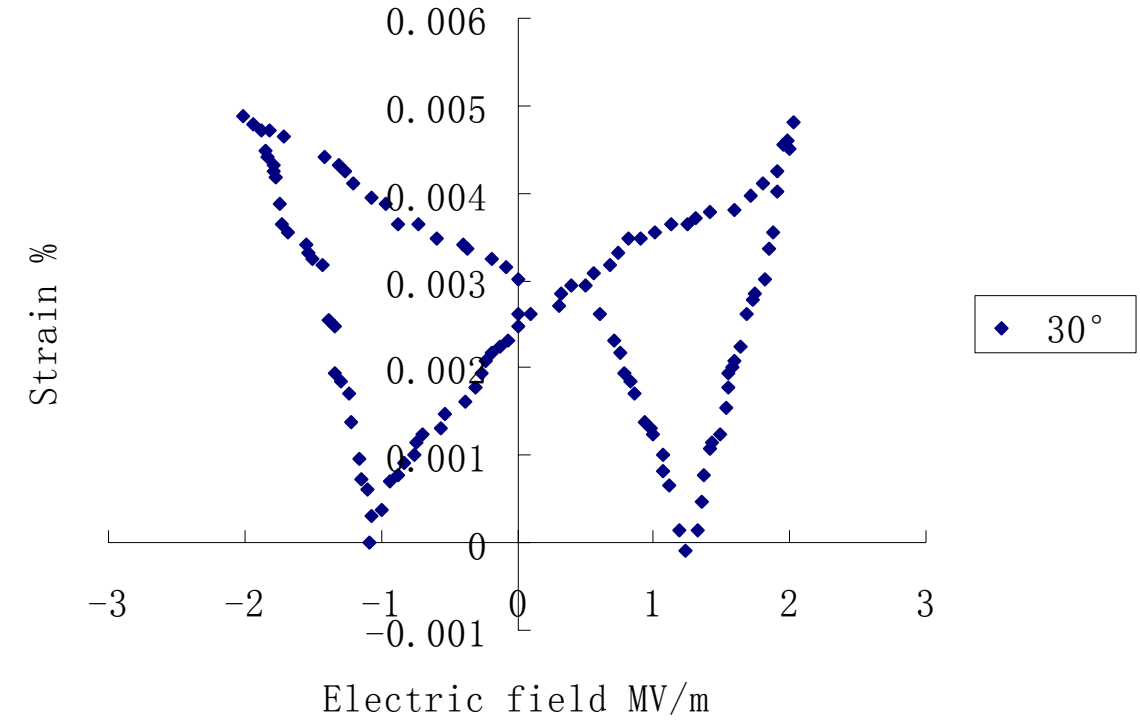

Fig 6.16 Electric field vs strain hysteresis loop at $\theta = 30°$

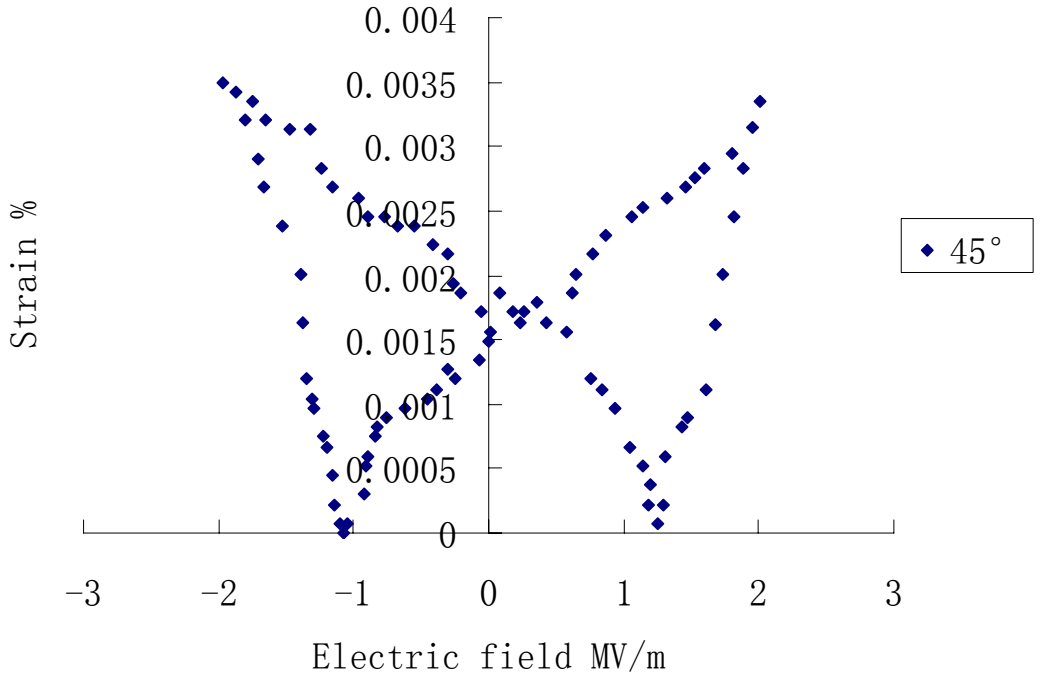

Fig 6.17 Electric field vs strain hysteresis loop at $\theta = 45°$

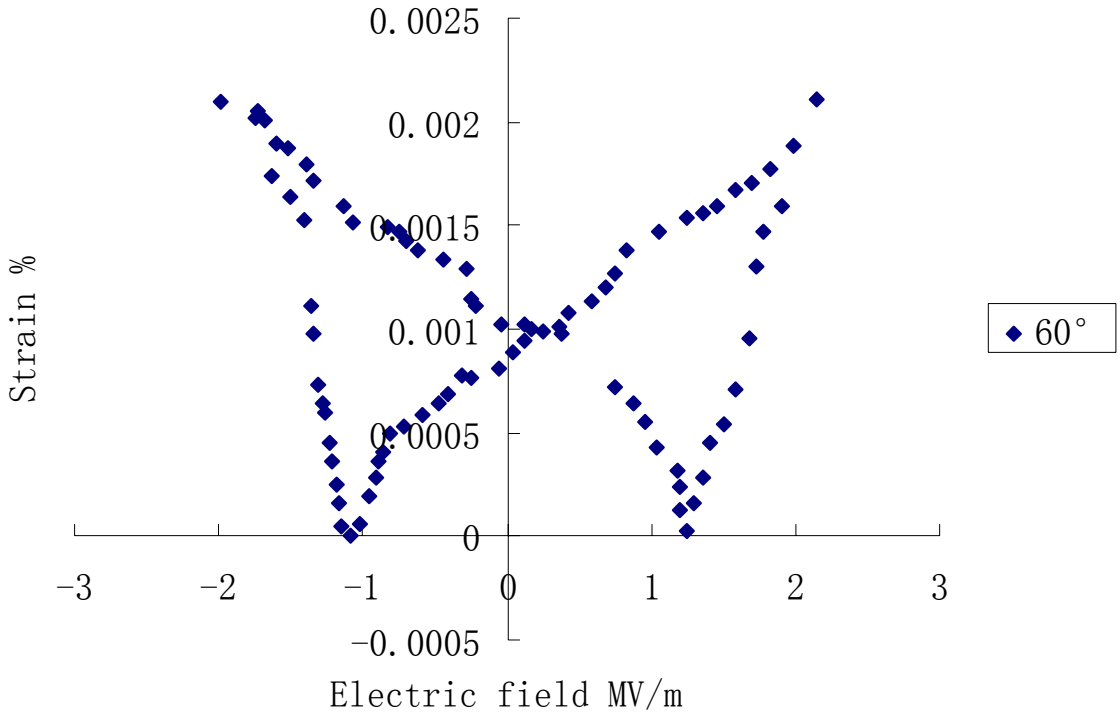

Fig 6.18 Electric field vs strain hysteresis loop at $\theta = 60°$

Fig 6.19 shows the comparison of electric field and strain relations at different angles. When the angle between electric field loading direction to the poling fiber direction increases, the butterfly curve shrinks and the remenant strain reduces. The change of remenant strain among the different angles from 0°, 30°, 45°, 60° to 90° is shown in Fig 6.20. At 0° angle, the remenant strain reaches the maxium.At 90° angle, there is no any hysteresis because of the epoxy matrix.

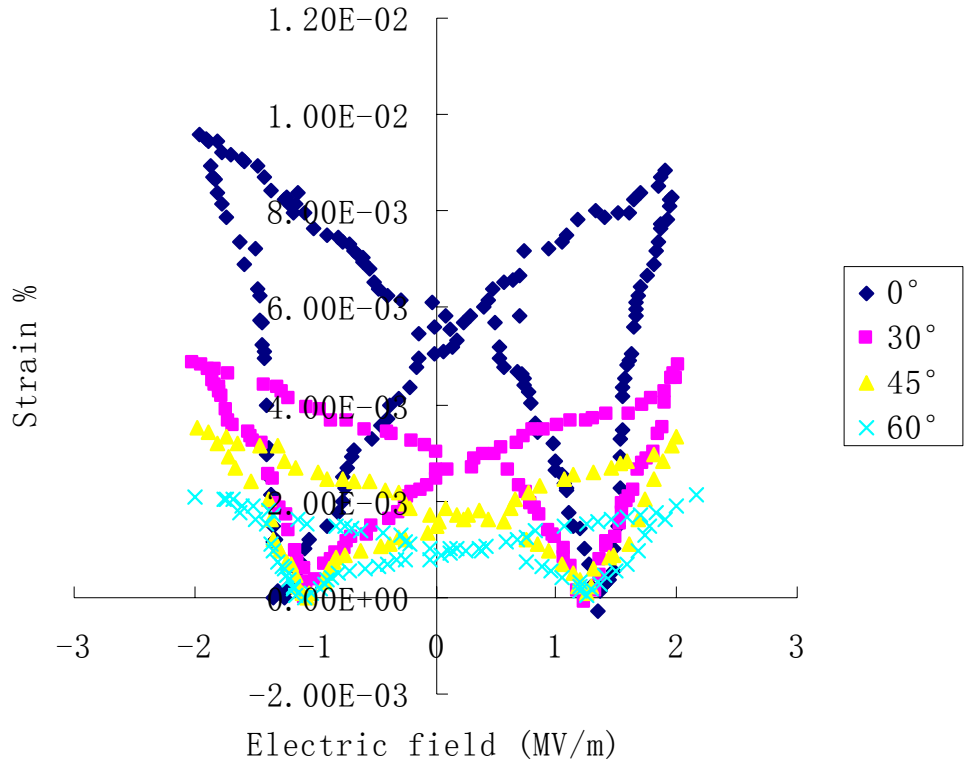

Fig 6.19 Comparison of the relation of electric field and strain at θ= 0°, 30°, 45°, 60°

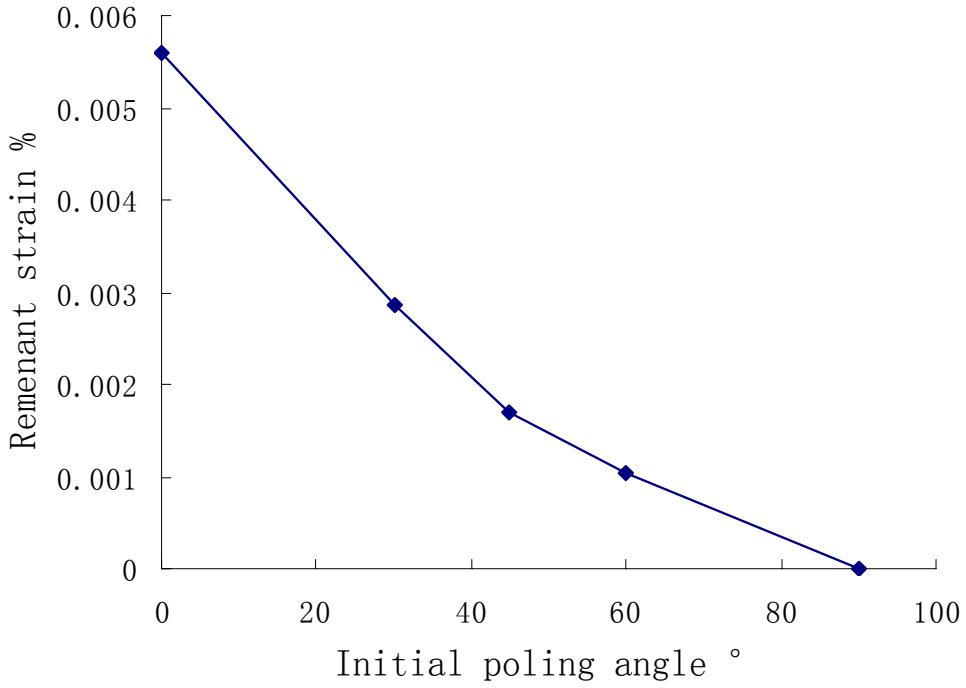

Fig 6.20 Change of the remenant strain in term of angle θ

6.5 Discussion and Conclusions

In this chapter, the experimental testing of 1-3 PZT5A1 composites under compression and electric field was carried out, respectively.

The results under compression, which include the relation of stress vs electric displacement and stress vs strain and the results under electric fields, which include the relation of electric field vs electric displacement and electric field vs strain show that the piezoelectric composites have nonlinear electromechanical coupling behavior under electrical loading. This nonlinear coupling response has very angle dependent effects. When the mechanical/electrical loading direction is parallel to the fiber direction (poling direction), the strain and electrical displacement reach the maximum. When the electrical loading direction is along the fiber direction with the angles at 30°，45° and 60°, the values of strain and electrical displacement decrease and the curves shrink till they vanish.

7. Micromechanical Modeling of Piezoelectric Composites

A two-level micromechanical theory is developed here to is adopted to study the nonlinear electro-mechanical coupling behavior for a piezoelectric composite. The idea comes from Lu and Weng's [3] original two-level micromechanics theory which was developed to study thermomechanical coupling behavior of shape memory alloys. The first level exists on the smaller PZT fiber level, or microscopic-level, in which, under the stress, an equivalent system [1,2,30,101] is represent by a two phase composite consisting of the transversely isotropic parent phase and the switched phase. The second level is on the composite, or macroscopic-level, consisting of the PZT inclusions and an inactive polymer matrix.

For clarity, we recall the equivalent system [1,2,30,101]. In this microscopic-level of PZT inclusion, the volume concentration of the switched phase with fibers is denoted by c_1 and transversely isotropic parent phase is denoted by c_0. So that, on this micro-scale, $c_1 + c_0 = 1$. On the macroscopic-level, we refer to inactive matrix as phase M and the active inclusions as phase f, with the volume concentration of matrix and inclusion are c_M and c_f respectively ($c_M + c_f = 1$).

7.1 Micromechanics Modeling on PZT Inclusions

Recall the micromechanics modeling of PZTs in chaper 4. Therefore, the overall response of the equivalent system can be obtained as

$$\overline{Y} = M_f \overline{X} + c_1 Y_{ds} \tag{7-1}$$

7.2 Constitutive Modeling on the Composite

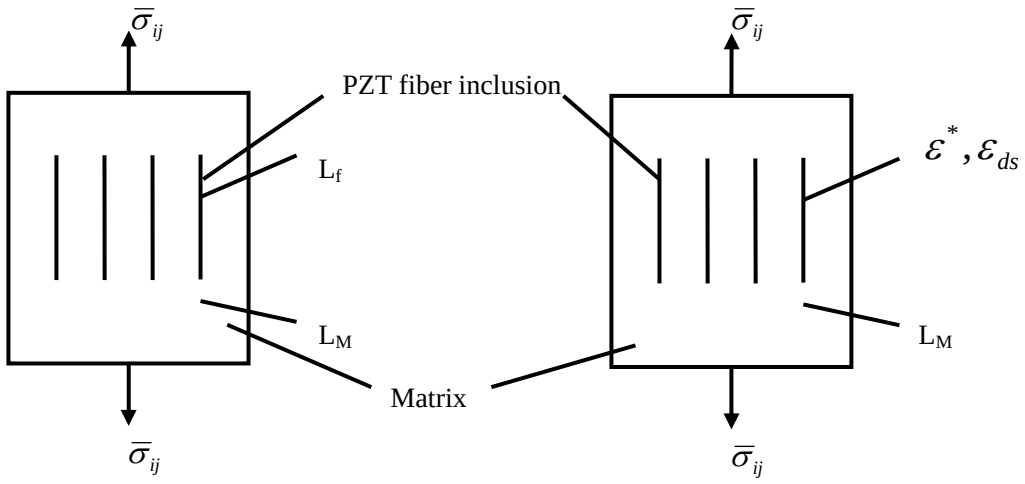

Fig 7.1 (a) The composite model and (b) the comparison material

Consider the analytical model described in Fig 7.1 (a) in which PZT fiber inclusions are uniformly dispersed aligned in the three-dimensional space. The inclusions and matrix are assumed to be linearly isotropic and perfectly bonded. To provide the basic structure for the subsequent analysis, the matrix is referred to as phase M, and the inclusion or PZT fiber as phase f with the volume fractions c_M and

c_f respectively. So that $c_M + c_f = 1$. A surface traction is prescribed on the boundary to give rise to a uniform stress $\bar{\sigma}$. We introduce an identical comparison material under same boundary condition in Fig 7.1 (b). The strain tenser in the homogeneous comparison material is then uniform, given by

$$\varepsilon^0 = L_M^{-1}\bar{\sigma} \tag{7-2}$$

where L_M is the elastic moduli tensor of the matrix and L_M^{-1} is its inverse or elastic compliance tensor.

During phase transformation in the inclusion, the overall PZT fiber concentration c_f keeps constant, the average stress $\sigma^{(M)}$ and strain $\varepsilon^{(M)}$ of matrix in real composite is different from $\bar{\sigma}$ and ε^0 due to the presence of inclusion, say by the amount $\tilde{\sigma}$ and $\tilde{\varepsilon}$, respectively. The average stress is given by

$$\sigma^{(M)} = \bar{\sigma} + \tilde{\sigma} = L_M(\varepsilon^M + \tilde{\varepsilon}) \tag{7-3}$$

Since the PZT fibers are embedded in the matrix, the average stress $\sigma^{(f)}$ and strain $\varepsilon^{(f)}$ of inclusion in real composite is father different from those of the surrounding matrix by the perturbed stress σ^{pt} and the perturbed strain ε^{pt} respectively. Eshelby's equivalence principle provides their average stress as

$$\sigma^{(f)} = \bar{\sigma} + \tilde{\sigma} + \sigma^{pt} \tag{7-4}$$

$$= L_f(\varepsilon^0 + \tilde{\varepsilon} + \varepsilon^{pt} - \varepsilon_{ds}) \tag{7-5}$$

$$= L_M(\varepsilon^0 + \tilde{\varepsilon} + \varepsilon^{pt} - \varepsilon_{ds} - \varepsilon^*) \tag{7-6}$$

where ε_{ds} represents phase transformation strain/ polarization strain due to domain switch in inclusions. ε^* represents the equivalent transformation strain, introduced to the region occupied by the inclusions, therefore their elastic moduli L_M can be

replaced by L_f to provide an identical $\sigma^{(f)}$.

The stress in the inclusions $\sigma^{(f)}$ and the matrix $\sigma^{(M)}$ must be in balance with the external $\bar{\sigma}$,

$$\bar{\sigma} = c_f \sigma^{(f)} + c_M \sigma^{(M)} \tag{7-7}$$

$$= c_f (\bar{\sigma} + \tilde{\sigma} + \sigma^{pt}) + c_M (\bar{\sigma} + \tilde{\sigma}) \tag{7-8}$$

$$= \bar{\sigma} + \tilde{\sigma} + c_f \sigma^{pt} \tag{7-9}$$

Therefore,

$$\tilde{\sigma} + c_f \sigma^{pt} = 0 \tag{7-10}$$

$$L_M \tilde{\varepsilon} + c_f L_M (\varepsilon^{pt} - \varepsilon_{ds} - \varepsilon^*) = 0 \tag{7-11}$$

$$\tilde{\varepsilon} = -c_f L_M (\varepsilon^{pt} - \varepsilon_{ds} - \varepsilon^*) \tag{7-12}$$

According to Eshelby's relation, the perturbed strain ε^{pt} and perturbed σ^{pt} are

$$\varepsilon^{pt} = S(\varepsilon_{ds} - \varepsilon^*) \tag{7-13}$$

$$\sigma^{pt} = L_M (\varepsilon^{pt} - \varepsilon_{ds} - \varepsilon^*) \tag{7-14}$$

where S is piezoelectric Eshelby tensor [58].

The total strain $\bar{\varepsilon}$ of the composite

$$\bar{\varepsilon} = c_f \varepsilon^{(f)} + c_M \varepsilon^{(M)} \tag{7-15}$$

To solve eigenstrain ε^*, return to eq.(7-4) & (7-5)

$$L_f (\varepsilon^0 + \tilde{\varepsilon} + \varepsilon^{pt} - \varepsilon_{ds}) = L_M (\varepsilon^0 + \tilde{\varepsilon} + \varepsilon^{pt} - \varepsilon_{ds} - \varepsilon^*) \tag{7-16}$$

Substitute eq. (7-12) into eq.(7-16), the equivalent transformation strain can be found,

$$\varepsilon^* = -[(L_f - L_M)(c_f I + c_M S) + L_M]^{-1} (L_f - L_M)[\varepsilon^0 + c_M (S - I)\varepsilon_{ds}] \tag{7-17}$$

where $\varepsilon_{ds} = c_1 \varepsilon_{ds}$

Once ε^* known, the stress of inclusion can be obtained from the eq. (7-6),

$$\sigma^{(f)} = L_M[\varepsilon^0 + c_M(S-I)(\varepsilon_{ds} + \varepsilon^*)] \tag{7-18}$$

The stress of matrix can be obtained from the eq. (7-3)

$$\sigma^{(M)} = L_M\{\varepsilon^0 - c_f[(S-I)\varepsilon_{ds} - (S+I)\varepsilon^*]\} \tag{7-19}$$

Recall the eq (7-1), which represents the stress-strain relation of PZT fiber inclusions. In order to be consistent with the indice in composite, rewrite it. So that the strain of inclusion can be provided by

$$\bar{\varepsilon}^{(f)} = M_f\sigma^{(f)} + c_1\varepsilon_{ds} \tag{7-20}$$

The strain of matrix can be given by

$$\varepsilon^{(M)} = L_M^{-1}\sigma^{(M)} \tag{7-21}$$

Therefore, the total strain of composite is

$$\bar{\varepsilon} = c_f\varepsilon^{(f)} + c_M\varepsilon^{(M)}$$

$$= c_f(M_f\sigma^{(f)} + c_1\varepsilon_{ds}) + c_M L_M^{-1}\sigma^{(M)} \tag{7-22}$$

7.3 Nonlinear Stress vs Strain and Stress vs Electric Displacement Relation under Compressive Loading

The two-level micromechanics model allows one to calculate the nonlinear stress-strain and stress-electric displacement response of a PZT-Epoxy composite. The properties of matrix such as elastic modulus and Poissons ratio are 5.8 x 10^9 Pa and 3.0, respectively [102]. The PZT5A1 composite are calculated using this model, then compared with the experimental data. The results are shown in Fig 7.2 and Fig 7.3.

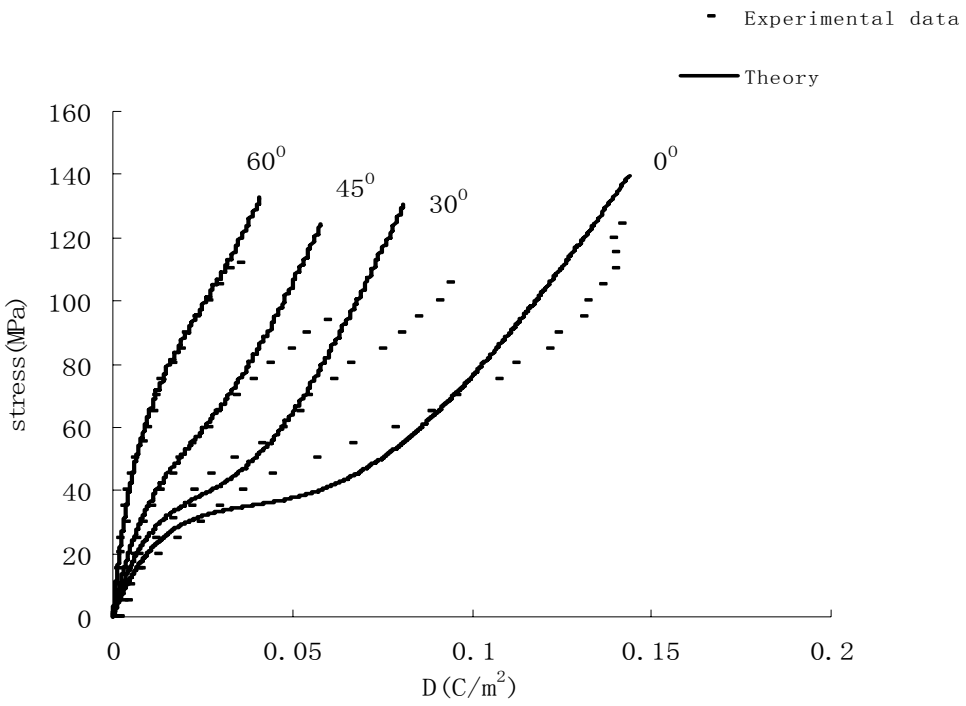

Fig 7.2 Comparison for stress-electrical displacement relation between theory and experimental data

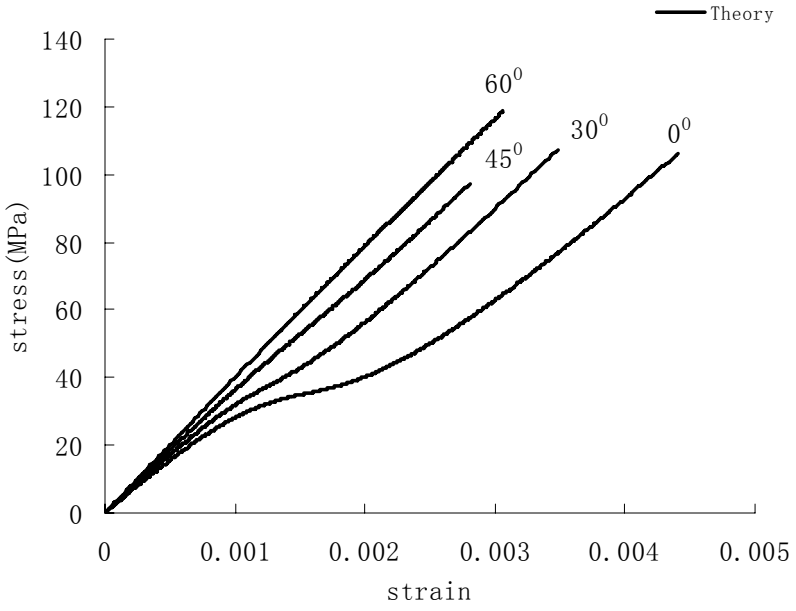

(a) Theory

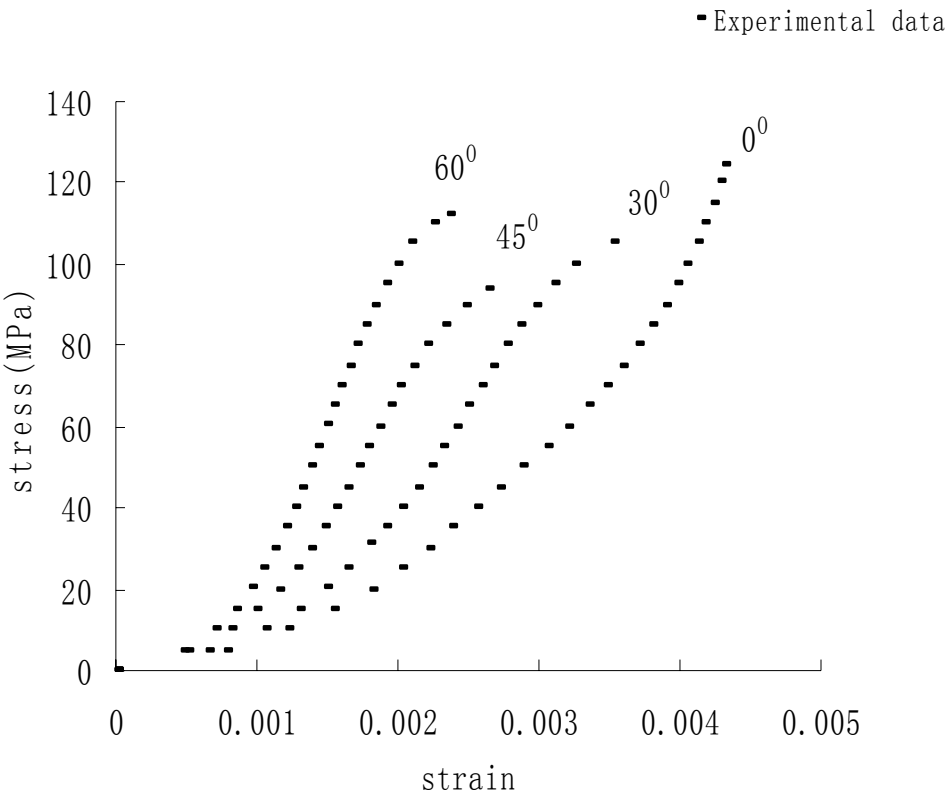

(b) Experimental data

Fig 7.3 Comparison for stress-strain relation between theory (a) and experimental data (b)

7.4 Discussion and Conclusions

The results from the theory are found to be in satisfactory agreement with the experimental data of stress vs strain and stress vs electrical displacement. It is clear that this two-level micromechanical model can capture the nonlinear electro-mechanical coupling behavior of PZT composite well under multiaxial compressive loading.

8. Conclusions and Future Works

8.1 Conclusions

In this dissertation, the experimental study and theoretical modeling for ferroelectrics and their composites were conducted in order to predict the effects of orientation on electromechanical behavior of ferroelectrics and their composites under mechanical and electric loading.

For ferroelectrics, a compressive load was applied on PZT specimens at different polarization angle and the response in terms of such angle dependence was captured. In the mean time, micromechanics based on an irreversible thermodynamics principle and physical morphology model was applied and compared with the experimental results. Therefore, the micromechanics model was proved to be still valid for multi-axial loading by the experimental investigation.

1-3 piezoelectric composites were used to study the electromechanical behavior of composites. The experimental investigation was conducted under multiaxial compressive loading. In parallel, a two-level micromechanics model was applied to compare with the experimental data. The theoretical results are found to be in a good agreement with the experimental data.

The experimental investigation for 1-3 piezoelectric composites under multiaxial electric loading were also carried out in this dissertation. The measured electric field vs electric displacement and electric field vs strain show nonlinear response and

strong angle dependence.

As a conclusion, for ferroelectrics and their composites, the electromechanical behavior all exhibits orientation dependence. The loading angle to the poling direction shows very strong effect on the electric response due to the anisotropic nature of ferroelectrics. When the applied compressive loading is vertical to the original poling direction, few domain switches can be expected. When the applied loading is parallel to the poling direction, which is also the case for practical application of ferroelectric materials and composites, the electric displacement or remnant polarization reaches maximum with nonlinear relation to the applied load. It is also clear that micromechanics models are suitable to capture the nonlinear electromechanical coupling behavior of ferroelectrics and their composites. Then the developed model can be used for prediction of electromechanical behavior of ferroelectrics and their composites.

8.2 Future Works

First of all, we can continue to finish the micromechanics modeling of ferroelectrics and their composites for their unloading part. Second, extend the two-level model to study the electromechanical response of piezoelectric composite under electric loading. Third, since the stress and strain relations we have obtained in the experimental testing are not very good, we can try to use the strain gauges instead of sensors to catch the displacement of specimen. After all, it is possible to see if the

experimental data could be improved.

References

1. J. Li and G.. J. Weng, A theory of domain switch for nonlinear behavior of ferroelectrics, Proc R Soc London, Ser, A 455, 3493 (1999)

2. J. Li and G. J. Weng, A micromechanics-based hysteresis model for ferroelectric ceramics, J, Intell, Mater Syst Struct, 12, 79 (2001)

3. Z. K. Lu, G. J. Weng, A two-level micromechanical theory for a shape-memory alloy reinforced composite, Int J Plasticity, 16, 1289 (2000)

4. J. E. Huber, N. A. Fleck, Multi-axial electrical switching of a ferroelectric: theory versus experiment, J Mech Phys Solids, 49, 785 (2001)

5. J. Shieh, J.E. Huber and N.A. Fleck, An evaluation of switching criteria for ferroelectrics under stress and electric field, Adv. Mater. (Weinheim, Ger.), 51, 6123 (2003)

6. J. F. NYE, Physical properties of crystals, Oxford University Press Inc., New York (1985)

7. Chad M. Landis, Non-linear constitutive modeling of ferroelectrics, Curr Opin Solid State Mater Sci, 8, 59 (2004)

8. Takuro Ikeda, Fundamentals of piezoelectricity, Oxford University Press (1996)

9. E. Fatuzzo and W. J. Merz, Ferroelectricity, North-Holland, Amsterdam (1967)

10. B. Jaffe, W. R. Cook and H. Jaffe, Piezoelectric Ceramics, Academic, London (1971)

11. M. E. Lines and A. M. Glass, Principles and application of ferroelectrics and related materials, Clarendon, Oxford (1977)

12. Franco Jona and G. shirane, Ferroelctric crystals, Dover publications, Inc, New York (1993)

13. T. Ikeda, Fundamentals of piezoelectrics, Oxford University Press, Oxford (1996)

14. B. A. Strukov and A. P. Levanyuk, Ferroelectric phenomena in crystals, Springer, Berlin (1998)

15. J. D. Eshelby, The determination of the elastic field of an ellipsoidal inclusion and related problems, Proc Roy Soc London, Ser A, 241, 376 (1957)

16. M. L. Dunn, M. Taya, Micromechanics predictions of the effective electroelastic moduli of piezoelectric composites, Int J Soilds Stuct, 30 (2), 161 (1993)

17. M. L. Dunn, Electroelastic green's functions for transversely isotropic piezoelectric media and their application to the solution of inclusion and inhomogeneity problems, Int J Eng Sci, 32, 119 (1994)

18. M. L. Dunn, H. A. Wienecke, Inclusions and inhomogeneities in transversely isotropic piezoelectric solids, Int J Solids Struct, 34), 3571 (1997)

19. S. C. Hwang, C. S. Lynch and R. M. Mcmeeking, Ferroelectric/Ferroelastic interactions and a polarization switching model, Acta Metall Mater, 43, 2073 (1995)

20. S. C. Hwang and R. M. McMeeking, The prediction of switching in polycrystalline ferroelectric ceramics, Ferroelectrics, 207, 465 (1998)

21. R. M. McMeeking and S. C. Hwang, On the potential energy of a piezoelectric inclusion and the criterion for ferroelectric switching, Ferroelectrics, 200, 151 (1997)

22. T. Michelitsch and W.S. Kreher, A simple model for the nonlinear material behavior of ferroelectrics, Acta Mater, 46, 5085 (1998)

23. X, Chen, D. N. Fang and K. C. Hwang, Micromechanics simulation of ferroelectric polarization switching, Acta Mater, 45, 3138 (1997)

24. J. Fan, W. A. Stoll and C. S. Lynch, Nonlinear constitutive behavior of soft and hard PZT: experiments and modeling, Acta Mater, 47, 4415 (1999)

25. Wolfgang Seemann, Arunachalakasi Arockiarajan, Bulent Delibas, Modeling and simulation of piezoceramic materials using micromechanical approach, European Congress on Methods in Applied Sciences and Engineering (2004)

26. Chin-The Sun and Ajit Achuthan, Domain-switching Criteria for ferroelectric materials subjected to electrical and mechanical loads, J Am Cream Soc, 87, 395 (2004)

27. H. Cao and A. G.. Evans, Nonlinear deformation of ferroelectric ceramics, J Am Ceram Soc, 76, 890 (1993)

28. W. Lu, D-N, Fang, C. Q. Li, K, C. Hwang, Nonlinear electric-mechanical behavior and micromechanics modeling of ferroelectric domain evolution, Acta Mater, 47, 2913 (1999)

29. C. S. Lynch, The effect of uniaxial stress on the electro-mechanical response of 8/65/35 PLZT, Acta mater, 44, 4137 (1996)

30. J. Li, Electromechanical coupling behavior of ferroelectric ceramics under multiaxial electric switching, J Appl Phys, 94, 5 (2003)

31. W, Chen and C. S. Lynch, A micro-electro-mechanical model for polarization switching of ferroelectric materials, Acta Mater, 46, 5303 (1998)

32. R. E. Newnham, D. P. Skinner and L. E. Cross, Connectivity and

piezoelectric-pyroelectric composites, Math, Res, Bull., 13, 525 (1978)

33. H. Banno. Recent developments of piezoelectric ceramic products and composites of synthetic rubber and piezoelectric ceramic particles, Ferroelectrics; 50, 329 (1983)

34. HLW Chan, J. Unsworth. Simple model for piezoelectric ceramic/polymer 1-3 composites used in ultrasonic transducer applications. IEEE Trans Ultrason Ferr; 36, 434 (1989)

35. W.A Simth, B.A. Auld, Modeling 1-3 composites piezoelectrics: thickness-mode oscillations. IEEE Trans Ultrason Ferr, 38, 40 (1991)

36. T. Olson, M. Avellaneda, Effective dielectric and elastic constants of piezoelectric polycrystals, J Appl Phys, 71, 4455 (1992)

37. P. Bisegana, R. Luciano, Variational bounds for the overall properties of piezoelectric composites, J Mech Phys Solids, 44, 583 (1996)

38. M. Hori, Nemat- Nasser S, Universal bounds for effective piezoelectric moduli, Mech Mater, 30, 1 (1998)

39. J. Y. Li, M. L. Dunn, Variational bounds for the effective moduli of heterogeneous piezoelectric solids, Philos Mag A, 81, 903 (2001)

40. P. Gaudenzi, On the electromechanical response of active composite materials with piezoelectric inclusions, Comput Struct, 65, 157 (1997)

41. C. Poizat, M. Sester, Effective properties of composites with embedded piezoelectric fibers, Comput Mater Sci, 16, 89 (1999)

42. B. Wang, Three-dimensional analysis of an ellipsoidal inclusion in a piezoelectric material, Int J Solids Struct, 29, 293 (1992)

43. Y. Benveniste, The determination of the elastic and electric fields in a piezoelectric inhomogeneity, J Appl Phys, 72, 1086 (1992)

44. T. Chen, An invariant treatment of interfacial discontinuities in piezoelectric media, Int J Eng Sci, 31, 1061 (1993)

45. M. L. Dunn, Taya M. An analysis of piezoelectric composite materials containing ellipsoidal inhomogeneities, Proc Roy Soc London, Ser A, 443, 265 (1993)

46. T. Chen, Micromechanical estimates of the overall thermoelectroelastic moduli of multiphase fibrous composites, Int J Solids Struc, 31, 3099 (1994)

47. J. H. Huang, W. S. Kuo Micromechanics determination of the effective properties of piezoelectric composites containing spatially oriented short fibers, Acta Mater, 44, 4889 (1996)

48. N. Fakri, L. Azrar, L. El Bakkali, Elctroelastic behavior modeling of piezoelectric composite materials containing spatially oriented reinforcements, Int J Solids Struct, 40, 361 (2003)

49. T. Mori, K. Tanaka, Average stress in matrix and average elastic energy of materials with misfitting inclusions, Acta Metall, 21, 571 (1973)

50. Y. Benveniste, A new approache to the application of mori-tanaka's theory in composite materials, Mech Mater, 6, 147 (1987)

51. R. Hill, A self-consistent machanics of composite materials, J Mech Phys Solids 13, 213, (1965)

52. B. Budiansky, On the elastic moduli of some heterogeneous materials, J Mech Phys Solids, 13, 223 (1965)

53. R. McLaughilin, A study of the differential scheme for composite materials, Int J Eng Sci, 5, 237 (1977)

54. A. N. Norris, A differential scheme for the effective moduli of composite, Mech Mater, 4, 1 (1985)

55. B. Wang, Effective behavior of piezoelectric composite, Appl Mech Rev, 47, 112 (1994)

56. M. L. Dunn, H. A. Wienecke, Green's functions for transversely isotropic piezoelectric solids, Int J Solids Struct, 33, 4571 (1996)

57. T. Chen Effective properties of platelet reinforced piezocomposites, Composites, Part B, 27, 467 (1996)

58. Y. Mikata, Determination of piezoelectric eshelby tensor in transversely isotropic piezoelectric solids, Int J Eng Sci, 38, 605 (2000)

59. Y. Mikata, Explicit determination of piezoelectric eshelby tensors for a spheroidal inclusion, Int J Solids Struct, 38, 7045 (2001)

60. Ronit Kar-Gupta, T. A. Venkatesh, Electromechanical response of 1-3 piezoelectric composites: An analytical model, Acta Mater, 55, 1093 (2007)

61. Ronit Kar-Gupta, T. A. Venkatesh, Electromechanical response of 1-3 piezoelectric composites: A numerical model to assess the effects of fiber distribution, Acta Mater, 55, 1275 (2007)

62. Dai-Ning Fang, Ai. Kah. Soh etc, Nonlinear behavior of 0-3 type ferroelectric composites with polymer matrices, Journal of Materials Science, 36, 5281 (2001)

63. Dai-Ning Fang, Ai. Kah. Soh etc, Nonlinear electric-mechanical behavior of

PZT-5 fiber reinforced composites with epoxy resin matrix, Journal of Materials Science Letters, 19, 1579 (2000)

64. G. M. Odegard, Constitutive Modeling of piezoelectric polymer composites, Acta Mater, 52, 5315 (2004)

65. H. Y. Zhang, L. X. Li, Y. P. Shen, Modeling of poling behavior of ferroelectric 3-3 composites, Int J Engr Sci, 43, 1138 (2005)

66. X, Zeng, R. K. N. D. Rajapkse, Eshelby tensor for piezoelectric inclusion and application to modeling of domain switching and evaluation, Acta Mater, 51, 4121 (2003)

67. Ahmad Safari, Rajesh K. Panda and Victor F. Janas Ferroelectric Ceramics: Processing, properties & applications, Rutgers University, Piscataway NJ (2006)

68. R. C. Buchanan, ed., Ceramic materials for electronics - processing, properties and applications, Marcel Dekker, New York (1986)

69. L. M. Levinson, ed., Electronic ceramics - properties, devices and applications, Marcel Dekker, New York (1987)

70. H. J. Hagemann, D. Hennings and R. Wernicke, Ceramic multilayer capacitors, Philips Tech. Rev., 41, 89 (1984)

71. J. H. Adair, D. A. Anderson, G. O. Dayton, and T. R. Shrout, A review of the processing of electronic ceramics with an emphasis on multilayer capacitor fabrication, J Matl. Ed., 9, 71 (1987)

72. J. F. Scott, L. Kammerdiner, M. Paris, S. Traynor, V. Ottenbacher, A. Shawabkeh, and W. F. Oliver, Switching kinetics of lead zirconate titanate submicron thin-film

memories, J Appl Phys, 64, 787 (1988)

73. J. F. Scott, C. A. Aranjo, H. B. Meadows, L. D. McMillan, and A. Shawabkeh, Radiation effects on ferroelectric thin-film memories: Retention failure mechanisms, J Appl Phys, 66, 1444 (1989)

74. D. Bondurant, and F. Gnadinger, Ferroelectric for nonvolatile RAMs, IEEE Spectrum, 26, 30 (1989)

75. J. F. Scott, and C. A. Aranjo, Ferroelectric Memories, Science, 246, 1400 (1989)

76. A. Baudrant, H. Vial and J. Daval, Liquid Phase Epitaxial Growth of LiNbO3 Thin Films, J Cryst Growth, 43, 197 (1978)

77. S. Miyazawa and N. Uchida, Refractive indices of E.G.M. grown Li(Nb,Ta)O_3 solid-solution optical waveguide , Opt and Quantum Electronics, 7, 451 (1975)

78. K. Sreenivas, M. Sayer, D. J. Baar, and M. Nishioka, Surface acoustic wave propagation on lead zirconate titanate thin films, Appl Phys Lett, 52, 709 (1988)

79. P. N. T. Wells, Biomedical ultrasonics, Academic Press, London (1977)

80. W. A. Smith, Composite piezoelectric materials for medical ultrasonic imaging trandusers-A review, Proc 6th Int Symp Appl Ferroelectrics, 249 (1986)

81. D. A. Christensen, Ultrasonic bioinstrumentation, John Wiley, New York (1988)

82. A. J. Moulson and J. M. Herbert, Electroceramics, materials, properties, and applications, Chapman and Hall, London (1990)

83. E. B. Tadmor, U. V. Waghmare, G.. S. Smith, E. Kaxiras, Polarization switching in $PbTiO_3$: an ab initio finite element simulation, Acta Mater, 50, 2989 (2002)

84. Sang-Joo Kim, Qing Jiang, A finite element model for rate-dependent behavior of

ferroelectric ceramics, Int J Solids Struct, 39, 1015 (2002)

85. S. Subrahmanyam and E. Goo, Nucleation of the ferroelectric phase in the $(Pb_xSr_{1-x})TiO_3$ system, Acta Mater, 46, 817 (1998)

86. Jie Wang, Yulan Li, Long-Qing Chen et, The effect of mechanical strains on the ferroelectric and dielectric properties of a model single crystal – Phase field simulation, Acta Mater, 53, 2495 (2005)

87. Jie Wang, San-Qiang Shi and Long-Qing Chen, Phase field simulations of ferroelectric/ferroelastic polarization switching, Acta Mater, 52, 749 (2004)

88. Eric Burcsu, G.. Ravichandran, Kaushik Bhattacharya, Electro-mechanical behavior of 90-degree domain motion in barium titanate single crystals, Smart Structures and Materials, Proc, SPIE , 4, 333 (2001)

89. www.americanpiezo.com

90. Daining Fang, Changqing Li, Nonlinear electric-mechanical behavior of a soft PZT-51 ferroelectric ceramic, Journal of materials science, 34, 4001 (1999)

91. Valentino R. Cooper, Local structure of PZT, AIP Conference Proceedings 626-Fundamental physics of ferroelectrics, 26 (2002)

92. J. Van Suchtelen, Product properties: A new application of composite materials, Philips Res Rep, 27, 28 (1972)

93. R. E. Newnham, Composite electroceramics, Ferroelectrics, 68, 1 (1986)

94. Ross and Sierakawski, Elastic Waves in Fiber-Reinforced Composites, Shock and Vibration Digest, 7, 96 (1975)

95. R. E. Newnham, L. J. Bowen, K. A. Klicker and L E. Cross, Composite

Piezoelectric Transducers, Materials Eng, 2, 93 (1980)

96. R. A. White, J. N. Webber and E. W. White, Replamineform: A new process for preparing porous ceramic, metal, and polymer prosthetic materials, Sicence, 176, 922 (1972)

97. Y. Su and G..J.Weng, A polycrystal model for the anisotropic behavior of a fully poled ferroelectric ceramic, J Appl Phys, 100, 114110 (2006)

98. J. Li, Orientation-dependent piezoelectric Eshelby S-tensor for a lamellar structure in a transversely isotropic medium, Acta Mech, 162, 69 (2003)

99. J. R. Rice, Continuum mechanics and thermodynamics of plasticity in relation to microscale deformation mechanisms. In: A.S. Argon, Editor, *Constitutive Equations in Plasticity*, MIT Press, Cambridge, MA, 23 (1975)

100. www.smart-material.com

101. P. Zhao, J. Li, Orientation dependence on electromechanical coupling behavior of ferroelectrics under compression, J Appl Phys, 103, 104104 (2008)

102. http://www.matweb.com